Lehigh University
Lehigh Preserve

Theses and Dissertations

1972

R.F. sputtering of nickel alloys

David Gregory Hill
Lehigh University

Follow this and additional works at: https://preserve.lehigh.edu/etd

Part of the Materials Science and Engineering Commons

Recommended Citation
Hill, David Gregory, "R.F. sputtering of nickel alloys" (1972). *Theses and Dissertations*. 4039.
https://preserve.lehigh.edu/etd/4039

This Thesis is brought to you for free and open access by Lehigh Preserve. It has been accepted for inclusion in Theses and Dissertations by an authorized administrator of Lehigh Preserve. For more information, please contact preserve@lehigh.edu.

R.F. SPUTTERING OF NICKEL ALLOYS

by

David Gregory Hill

ABSTRACT

The R.F. sputtering of nickel alloys was investigated to characterize the interrelationship of the deposition parameters and to determine the compositional and microstructural variation of the deposited thin films. Materials in the γ and $\gamma+\gamma'$ regions of both the Ni-Al and Ni-Ta alloy systems were sputtered on to glass substrates and carbon support films. The analysis entailed multiple beam interferometry, electron microprobe analysis and both normal and hot stage transmission electron microscopy.

The deposition of the films is related to the measured sputtering parameters of time, R.F. kilovoltage, D.C. bias kilovoltage and argon pressure. Specific attention is focused on the sputtering yields of the species and the sticking coefficients of the species as affected by the sputtering variables. Variation in composition from the target to the thin film is analyzed with respect to the sputtering parameters and the material properties of the species. Finally, the structure of thin sputtered films is related to the nucleation and growth processes, the surface mobility of each specie and the mismatch of the solute species with respect to nickel.

R.F. SPUTTERING OF NICKEL ALLOYS

by

David Gregory Hill

A Thesis

Presented to the Graduate Committee

of Lehigh University

in Candidacy for the Degree of

Master of Science

in

Metallurgy and Material Science

Lehigh University

1972

CERTIFICATE OF APPROVAL

This thesis is accepted and approved in partial fulfillment of the requirements for the degree of Master of Science.

September 11, 1972
(date)

Michael R. Notis
Professor in Charge

G. P. Conard II
Chairman of Department

ACKNOWLEDGEMENTS

The author is much indebted to Dr. Michael R. Notis for his invaluable direction and criticism of this thesis work.

Grateful acknowledgements are made to Dr. J. I. Goldstein for several discussions on the electron microprobe analysis and to Dr. G. Krauss for his assistance in interpretation of the transmission electron microscopy results. In addition, the author's appreciation is especially extended to D. Bush and R. Korastinsky for their technical assistance during this research.

The author is gratefully indebted to the Carpenter Technology Corporation and to the National Aeronautics and Space Administration for sponsorship of this investigation.

TABLE OF CONTENTS

Page

Certificate of Approval ii

Acknowledgements. iii

List of Tables. vi

List of Figures viii

List of Appendices. xii

Abstract. 1

Introduction

A. General. 2

B. The Alloy Systems Investigated 3

C. The Sputtering Process 4

D. Film Deposition During Sputtering. 9

E. Purpose. 14

Description of Experimental Apparatus and Procedure

A. Sputtering Process 15

B. Film Thickness Measurement 19

C. Electron Microprobe Analysis 20

D. Transmission Electron Microscopy 22

Results and Discussion

General. 24

Deposition Parameters. 25

Composition. 48

Target Surface Phenomena 64

Microstructure 69

Conclusions 86

List of References. 168

Vita. 174

LIST OF TABLES

		Page
Table I	Physical Properties of Al, Ni and Ta	88
Table II	Composition of Powder Mixtures for Plasma Sprayed Targets	88
Table III	Chemical and Sieve Analyses of Elemental Powders	89
Table IV	Composition of Machined Plate Targets	90
Table V	Runs with Time Varied for 93.1Ni - 6.9Al Alloy Target	91
Table VI	Runs with D.C. Bias Varied for 93.1Ni - 6.9Al Alloy Target	92
Table VII	Runs with Argon Pressure Varied for 93.1Ni - 6.9Al Alloy Target	93
Table VIII	Runs with Ni-Al Targets at Constant Sputtering Parameters for Deposition Rate Analysis	94
Table IX	Runs with Ni-Ta Targets at Constant Sputtering Parameters for Deposition Rate Analysis	95
Table X	Runs with Ni-Al Targets at Constant Sputtering Parameters for Microprobe Analysis	96
Table XI	Runs with Ni-Ta Targets at Constant Sputtering Parameters for Microprobe Analysis	97
Table XII	Runs with Various Targets for Transmission Electron Microscopy	98
Table XIII	Sputtering Yield for Ni, Al and Ta by Ar^+ Ions	99

Table XIV	Threshold Energy for Ni, Al and Ta	99
Table XV	Sputtering Yields and Target Surface Composition for Ni-Al Alloy Target for Various Target Voltage Conditions	100
Table XVI	Calculated Deposition Rate Ratio and Deposition Rates	100
Table XVII	Wet Chemical Analysis of Plasma-Sprayed Targets	101
Table XVIII	Electron Microprobe Analysis of Ni-Al Sputtered Films	102
Table XIX	Electron Microprobe Analysis of Ni-Ta Sputtered Films	103
Table XX	Calculated Target Composition for Ni-Ta Plasma Sprayed Targets	104

LIST OF FIGURES

		Page
Figure 1	The Ni-Al Phase Diagram	105
Figure 2	The Ni-Ta Phase Diagram	106
Figure 3	Substrate Configurations	107
Figure 4	R.F. Sputtering Apparatus	108
Figure 5	Variation of R.F. Kilovoltage with Deposition Time	109
Figure 6	Target Voltage as a Function of Time	110
Figure 7	Film Thickness Versus Deposition Time for Ni-Al Alloy Target	111
Figure 8	R.F. Kilovoltage Versus D.C. Bias Kilovoltage	112
Figure 9	Target Voltage with Respect to Ground Versus Time for Various Voltage Conditions	113
Figure 10	Sputtering Yield of Ni and Al Versus Ar^+ Energy	114
Figure 11	Film Thickness Versus Deposition Time for Various Voltage Conditions on Ni-Al Alloy Target	115
Figure 12	Film Thickness and Deposition Rate Versus R.F. Kilovoltage for Ni-Al Alloy Target	116
Figure 13	Film Thickness for 10 Minutes Versus Argon Pressure for Ni-Al Alloy Target	117
Figure 14	Mean Free Path of Argon Versus Argon Pressure	118
Figure 15	R.F. Forward Power Versus Argon Pressure for Ni-Al Alloy Target	119

Figure 16	Plot of Aluminum Content in Plasma Sprayed Target Versus Aluminum Content in Powder	120
Figure 17	Plot of Tantalum Content in Plasma Sprayed Target Versus Tantalum Content in Powder	121
Figure 18	Silicon K Alpha Intensity Versus Microprobe Kilovoltage for Thin Films and Bulk Sample	122
Figure 19	Comparison of Microprobe Results for 1.2 μ Ni-Al Films at 8 kv and 20 kv	123
Figure 20	Plot of Aluminum Content in Sputtered Film Versus Aluminum Content in Target	124
Figure 21	Plot of Tantalum Content in Sputtered Film Versus Tantalum Content in Target	125
Figure 22	Solid State Detector Scans for Pure Nickel Target and 1.2 μ Thin Film	126
Figure 23	Solid State Detector Scans for Ni-Al Alloy Target and 1.2 μ Thin Film	127
Figure 24	Solid State Detector Scans for Ni-Ta Alloy Target and 1.2 μ Thin Film	128
Figure 25	Surface Topography of Ni - 9.7Ta Plasma Sprayed Target	129
Figure 26	Surface Topography of Ni - 6.8Al Plasma Sprayed Target	130
Figure 27	Microstructure of Ni-Ta Alloy Target as Polished and Chemically Etched	131
Figure 28	Microstructure of Fine Precipitate Matrix of Ni-Ta Alloy Target as Polished and Chemically Etched	132

Figure 29	Low Magnification Micrograph of Surface Topography of Ni-Ta Alloy Target after Sputtering	133
Figure 30	High Magnification Micrographs of Surface Topography of Ni-Ta Alloy Target after Sputtering	134
Figure 31	Micrograph of As-Sputtered Structure of Pure Aluminum Thin Film	135
Figure 32	Micrograph of As-Sputtered Structure of Pure Nickel Thin Film	136
Figure 33	Micrographs of As-Sputtered Structure of Two Ni - 1.46Al Thin Films	137
Figure 34	Structure and Selected Area Diffraction Pattern of As-Sputtered Ni - 3.95Al Thin Film	138
Figure 35	Structure and Selected Area Diffraction Pattern of As-Sputtered Ni - 36.7Ta Thin Film	139
Figure 36	Selected Area Diffraction Patterns Showing Texture of Ni - 36.7Ta Thin Film on Tilting	140
Figure 37	Low Magnification Micrograph of Film Break Up on Heating	141
Figure 38	High Magnification Micrograph of Agglomerated Structure	142
Figure 39	Micrograph of Irregular Film Break Up Pattern	143
Figure 40	Selected Area Diffraction Pattern of Ni - 3.95Al Thin Film at 265°C	144

Figure 41	Selected Area Diffraction Pattern of Ni - 3.95Al Thin Film at 415°C	145
Figure 42	Bright Field and Dark Field Micrographs of Ni - 3.95Al Structure at 700°C	145
Figure 43	Selected Area Diffraction Pattern of Ni - 36.7Ta Thin Film at 410°C	146
Figure 44	Structure and Selected Area Diffraction Pattern of Ni - 36.7Ta Thin Film at 900°C	147

LIST OF APPENDICES

		Page
Appendix I	Description of the Three Stages for Sputtering	148
Appendix II	Data Sheet	150
Appendix III	Calculation of the Sticking Coefficient of Nickel on Glass	151
Appendix IV	Analysis of Sputtering Yield Versus Ion Energy	154
Appendix V	Analysis of Deposition Rate for Ni-Al Alloy Target	160
Appendix VI	Aluminum Sticking Coefficient Calculation for 93.1Ni - 6.9Al Alloy Target	164
Appendix VII	Target Composition Calculation for Ni-Ta Plasma Sprayed Targets	166

ABSTRACT

The R.F. sputtering of nickel alloys was investigated to characterize the interrelationship of the deposition parameters and to determine the compsitional and microstructural variation of the deposited thin films. Materials in the γ and $\gamma+\gamma'$ regions of both the Ni-Al and Ni-Ta alloy systems were sputtered on to glass substrates and carbon support films. The analysis entailed multiple beam interferometry, electron microprobe analysis and both normal and hot stage transmission electron microscopy.

The deposition of the films is related to the measured sputtering parameters of time, R.F. kilovoltage, D.C. bias kilovoltage and argon pressure. Specific attention is focused on the sputtering yields of the species and the sticking coefficients of the species as affected by the sputtering variables. Variation in composition from the target to the thin film is analyzed with respect to the sputtering parameters and the material properties of the species. Finally, the structure of thin sputtered films is related to the nucleation and growth processes, the surface mobility of each specie and the mismatch of the solute species with respect to nickel.

INTRODUCTION

A. General

Interest in the use of thin films lies primarily in the areas of microcircuitry for electronic devices and of protective coatings. The largest demand for thin films is in the electronic industry where thin film microcircuits offer small size, ease of fabrication and high reliability unobtainable with either mechanical or solder connections. Thin film protective coatings are now finding wide use in applications for wear resistance, corrosion resistance, heat resistance or a combination of these properties.

Thin films also represent a very suitable vehicle to study some of the fundamental properties and the structure of materials that are not possible to examine in the bulk. Thin film deposition studies have provided an invaluable tool in developing the general theories of nucleation and growth phenomena, while transmission electron microscopy and electron diffraction are now commonly used to study the fine structure of materials. Also, metastable phases have been deposited as thin films and the solid state reactions of these metastable phases have been investigated.

Currently there are two general categories of commercially attractive methods of thin film deposition; these are vacuum sputtering and vacuum evaporation. The

evaporation technique is generally applied where relatively pure metals with melting points below 1000°C are required. Sputtering is usually applied to high melting point materials such as refractory or semi-refractory metals. The sputtering process can also be used to deposit the span of materials from conductors such as Aℓ and Ta to insulators such as $A\ell_2O_3$ and Ta_2O_5 by varying the sputtering technique. Finally the sputtering process also represents a more convenient and more controllable method for the deposition of alloys or multiphase materials than does vacuum evaporation.

This research concerns the composition and microstructure of R.F. sputtered thin binary alloy films and the effects of the sputtering process variables upon these properties.

B. The Alloy Systems Investigated

The two alloy systems studied during this investigation were the Ni-Aℓ and Ni-Ta binary systems. These systems are being used or have high potential application for use as protective coatings for superalloy and refractory bulk materials and for the study of precipitation hardening effects of the γ'-phase in nickel based superalloys. The primary physical properties of the elemental metals (Aℓ, Ni,Ta) used in this research are given in Table I[1]. Of the four major alloying elements that partition to the γ' phase of nickel based alloys (i.e. Aℓ,Ti,Nb,and Ta[2]),

aluminum and tantalum form the end members with respect to the properties of nickel. Based on the lattice parameter effects in the nickel binary alloys, aluminum has a +6% difference in atomic diameter and tantalum has a +18% difference. Comparing the electron configuration of the γ' forming elements to that of nickel, aluminum has the largest electron vacancy number (7.66) and tantalum has the smallest (5.66). In addition to demonstrating extremes in atomic size and atomic bonding, the Ni-Aℓ and Ni-Ta systems exhibit considerably different variations in the extent of both the γ-solid solution region and the width of the (γ+γ') phase fields as shown in Figures 1 and 2 [3].

C. The Sputtering Process

Sputtered thin films have many characteristic properties which depend to a significant degree on the conditions of deposition. As noted by previous investigators the general parameters that have a major effect on the sputtered thin films are listed as follows:

(1) method of sputtering, i.e. type of input power, power levels, electrode configuration, substrate bias

(2) nature and purity of plasma, i.e. 99.99% Ar, 90% Ar-10%N_2, etc.

(3) composition, purity and morphology of target

(4) rate of sputtering and deposition

(5) temperature of substrate

(6) nature of substrate, i.e. crystalline or amorphous, surface condition

There are two general methods of sputtering: either direct current (D.C.) sputtering or radio frequency (R.F.) sputtering. The D.C. sputtering method is fairly simple in design but has certain limitations which complicate the deposition of thin films. The D.C. glow discharge diode sputtering technique can use only electrically conducting targets and is difficult to control due to the inter-relation of a large number of variables. The ion current density, and consequently the sputtering rate, depend on the system pressure, the electrode spacing, the residual gas composition and the cathode-anode voltage. In D.C. diode sputtering, the gas pressure required for stability of the glow discharge is relatively high (25 to $100 * 10^{-3}$ torr). The consequent ratio of gas molecules to sputtered atoms is high and results in frequent contamination of the film. There are several possible modifications which may be made to the basic D.C. glow discharge diode sputtering technique in order to improve the conditions of deposition. By applying a significantly large negative potential to the anode (i.e. the substrate), low energy ions from the plasma bombard the substrate with an effective cleaning action; this process is called D.C. bias diode sputtering [4]. Another variant to straight D.C. diode sputtering is the use of an asymmetric alternating current [5]. The asymmetric A.C. method is analogous to the D.C. bias diode process in that during alternate half cycles, the substrate

is cleaned. Lower deposition rates are achieved with both D.C. bias and asymmetric A.C. sputtering; however, the cleaner films produced somewhat compensate for this effect. Another method to attain clean films through the D.C. sputtering process is to achieve a low pressure plasma through the use of a thermionic emission source. The two variations on this principle are thermionically and/or magnetically assisted triode sputtering [6]. The D.C. triode method can maintain a plasma at a pressure as low as $1 * 10^{-3}$ torr by the injection of auxiliary electrons from the thermionic source. One salient advantage of the triode process is the fine control of the current density through the variation of the applied magnetic field.

The more versatile R.F. sputtering process as used in the present research can be used to sputter from insulators and semiconductors as well as metals with a high degree of control of the plasma and the deposition conditions. In an R.F. system, control of the sputtering conditions results from the direct excitation of the free electrons present in the system by the R.F. source and the consequent production of a plasma at low pressures (1 to $10 * 10^{-3}$ torr). High negative self-biasing of an insulator cathode occurs because of the difference in electron and ion mobilities in the R.F. field and the resultant negative charge build-up at the insulator surface; high sputtering rates are therefore easily obtained for insulators. Metals may be

sputtered through the use of capacitively coupled matching networks [7,8]. The general improved characteristics of an R.F. process over a D.C. diode process are a higher purity plasma, an increased mean free path of particles travelling through the plasma, a lower reactivity of freshly sputtered surfaces and a better quality film. The primary disadvantage of using R.F. power is the design of feedthroughs and electrical apparatus to minimize reflected power losses. In analogy to the modifications of the D.C. technique which have been developed in order to provide a more versatile process and higher purity films, similar modifications have been developed for the R.F. process. Methods such as getter sputtering [9] are used to provide high purity plasmas; substrate tuning [10] may be used to provide either positive or negative bias at the substrate (anode); sputter etching may be used to preclean either the cathode or anode prior to sputtering as well as being an important high resolution commercial etching process in and of itself[11]. Reactive sputtering methods, whereby compounds may be deposited from metal targets by the introduction of a reactive gas specie into the plasma, are available in both the R.F. and D.C. technique [12].

The particular gas chosen for the sputtering atmosphere is dependent on three major criteria [13]: (1) it should be inert to the material sputtered, (2) it should give a high sputtering yield, and (3) it should be

obtainable in high purity. The purity of the gas is paramount in that any reactive specie will increase the contamination of the thin film. Argon is the most generally used inert gas for non-reactive sputtering and is the gas used for the present research.

The target configuration for sputtering depends on the design of the sputtering system and on the material to be sputtered. A cylindrical cathode with magnetic field assistance was used by Gill and Kay [14] to sputter at a very low pressure (10^{-5} torr). Steidel, Jaffe and Kumagai[15] used alternating rods of tantalum and aluminum with a D.C. biased, A.C. sputtering system to control the composition of the thin film. The most common configuration is a set of parallel plates with a normal electric field between the cathode and anode.

There are essentially three methods of target construction for sputtering alloy thin films. One method involves deposition from a bi-metal target. A bi-metal target is constructed either by overlaying a screen or grid of the alloy specie over the face of the base cathode [16] or by inlaying strips or islands of the alloying element in the base metal cathode. The composition of the deposited film from a bi-metal cathode depends on the relative areas covered by each specie and the sputtering yields for each specie. A second method is to fabricate the cathode from powders. The two variants of this method are to plasma

spray the elemental material powders on a base plate in an inert atmosphere [16] or to sinter the elemental powders in the cathode configuration [16,17]. For both processes, the powders may be a single specie or a mixture of elements in the correct proportion. This method is particularly suited to high melting point materials or to multicomponent systems where the solubility characteristics do not permit solid solution alloying. The third and most obvious method for alloy sputtering is to deposit from an alloy cathode. When a multiphase alloy target is used, the morphology of the structure is an important consideration since the alloy components should sputter at a ratio proportional to their local atomic configuration. It is imperative to reach a steady state condition for an alloy target so that the surface sputters at a uniform rate independent of the phases present.

D. Film Deposition During Sputtering

While the primary quantities desired to be controlled during deposition are the sputtering rate and the deposition rate, they in turn depend on a number of significant variables. The sputtering rate, defined as the rate of removal of target atoms per unit area and unit time, is a function of the target composition, ion flux to the target, and the sputtering yield for each specie. Analytically the relation may be approximated by [18]:

$$\dot{N}_i = x_i * J * y_i \quad (1)$$

$\dot{N}_i$ = sputtering rate of specie i

x_i = atom fraction of specie i in target

J = ion flux

y_i = sputtering yield of specie i

The deposition rate is defined as the rate of film growth and involves not only the sputtering rate but also the sticking coefficient of each specie, the resputtering rate and the evaporation rate. As given by Winters et al. [19], the deposition rate may be approximated by:

$$\dot{D}_i = s_i \dot{N}_i - N_i' - \mu_i \quad (2)$$

$\dot{D}_i$ = deposition rate of specie i

s_i = sticking coefficient of specie i

$\dot{N}_i$ = sputtering rate of specie i

N_i' = resputtering rate of specie i

μ_i = evaporation rate of specie i

Almost all of the variables in the sputtering process influence the sputtering and deposition rates in a major way. The relationship of these variables to each other and to the sputtering and deposition rates will be demonstrated in the discussion section of this thesis.

One variable that can be measured and controlled fairly well is the substrate temperature. The nucleation and growth mechanisms of thin films have a definite

dependence on the substrate temperature. Neugebauer [20] has made a complete study of the condensation, nucleation and initial growth of thin films so that these aspects will not be discussed here. The substrate temperature also has a significant effect on the deposition rate and the composition and microstructure of the deposited film.

The sticking coefficient as given in equation (2) is directly dependent on the substrate temperature as shown by Chopra [21]. As the substrate temperature increases, the sticking coefficient generally decreases, the basic parameter being the relative ratio of the substrate temperature (T_s) to the specie's melting point (T_{mp}). For an alloy target under steady state conditions (i.e. the composition of sputtered particles is the same as the average composition of the target), the sticking coefficient of each specie determines the change in composition from the target to the film. For low substrate temperature, say on the order of $T_s/T_{mp} < 0.1$, the film will nominally have the bulk target composition under steady state conditions.

Mader [22] has shown that the relative substrate temperature and the atomic size ratio are the major factors that influence the microstructure of thin films. At low relative substrate temperatures, films with atomic size ratios less than 1.1 form crystalline films and conversely films with larger size ratios deposit as amorphous films. The critical size ratio, below which crystalline films

will be deposited, is shifted to higher values as the substrate temperature is increased. These observations will be further explained in connection with the results of this research.

Another salient point concerns the effect of substrate temperature on the incorporation of gasses during sputtering. The mechanism of gas incorporation is the sorption of molecules, atoms or ions which dissociate upon collision with the surface, or of energetic particles which penetrate the lattice. Spitzer [23] has shown that, during the reactive sputtering of niobium nitride, the combined effects of substrate temperature and argon/nitrogen (Ar/N_2) partial pressure ratio results in different microstructures and significant changes in the Curie temperature for the sputtered niobium nitride films. For a constant partial pressure ratio ($Ar/N_2 = 35$), an increase in substrate temperature from 300°C to 700°C produced a significantly different nitride (i.e. a different nitrogen content) and resulted in an increase in Curie temperature from 7.9°K to 14.7°K. The incorporation of a gas specie depends also on the deposition rate, gas pressure and substrate potential and often the substrate temperature effects are overshadowed by these other factors.

The final factor influencing the properties of sputtered thin films is the nature of the substrate. The effects of the substrate material can be separated into two

general areas: those affecting the sputtering process mechanisms and those affecting thin film formation. The substrate properties of concern with respect to the sputtering process are the electrical conductivity, thermal conductivity, surface texture and composition. The electrical properties of the substrate, whether conducting or insulating, influence the potential of the surface of the substrate and can alter the plasma region next to the substrate. The thermal conductivity determines the transient substrate temperature characteristics which, as previously noted, affect the sticking coefficient of each specie. The surface texture and composition of the substrate also influence the sticking coefficients by affecting the binding energy of atoms to the substrate and the mobility of the sputtered atoms on the substrate surface.

With respect to thin film formation, the surface texture and the crystallographic structures of the substrate are the major considerations. The nucleation rate of the film depends not only on the deposition rate but also on the surface configuration (i.e. smoothness) and the surface wettability. The crystallographic structure of the substrate is important as to whether the film will be amorphous, single crystal, polycrystalline with a random or textured orientation or a combination of these. One of the most critical effects is the variability of the surface of the substrate and it is therefore imperative

to have the surface thoroughly clean for consistent results.

E. Purpose

As has been shown in the prior discussion, each of the sputtering parameters influence either the mechanisms involved in the sputtering process or the material properties of the deposited thin film. The present research concentrates on the relationship between the sputtering process parameters and the material properties of composition and microstructure for the two binary alloy systems. The R.F. kilovoltage, the associated D.C. bias kilovoltage, the argon pressure and the substrate temperature are the sputtering variables measured and the chemical composition, phases present, crystallite size and crystal structure are studied for the films.

DESCRIPTION OF EXPERIMENTAL APPARATUS AND PROCEDURE

A. Sputtering Process

Two types of targets were used in this research. One set of targets was fabricated by plasma spraying a powder mixture of the desired composition on a 1/4" thick by 6" diameter commercially pure aluminum target. Seven plasma-sprayed targets were made with the powder compositions as given in Table II. The chemical and sieve analyses for the elemental powders are shown in Table III. The second set of targets was machined from plate stock and their composition is given in Table IV. The plate targets were 6" in diameter with the exception of the 65.2Ni - 34.8Ta target which was fabricated from a chill casting and machined to a 4-1/2" diameter disc. The plate target thickness varied with the total material present.

Three substrate configurations were employed in this investigation with a similar substrate holder for each. The substrate holder was a 1/4" by 6-1/2" diameter plate with a 3" by 3" by 0.040" recess and two clamps. The substrate varied depending on whether the experiment was for deposition rate determination, electron microprobe analysis or transmission electron microscopy; each arrangement is shown in Figure 3. The glass slides were cleaned with hot chromic acid, washed with de-ionized water, rinsed with

methanol and baked at 100°C - 150°C. Nickel grids (150 mesh) with either a carbon or silicon monoxide support film were used for the transmission electron microscopy work. The clamps on each substrate holder were to assure positive thermal contact between the substrate and the holder. The beveled microscope slides and the plain slides enabled film thicknesses to be measured for all configurations.

The sputtering apparatus was a typical diode sputtering setup as shown in Figure 4. The R.F. generator was a Lepel crystal controlled generator model number T-2-1-MC1-X-BW which has a single phase output at a frequency of 13.56 MHZ. The generator was matched to a 50 ohm load at a power level of 2000 watts. Power was controlled by the crystal driver control and monitored by a watt meter positioned between the generator and the matching network. The matching network was designed to match the sputtering module and target electrode to a 50 ohm impedance and thus obtain zero reflected power. Two meters, a D.C. bias and an R.F. kilovolt meter, were located on the matching network and measured the effective kilovoltage between the target and the substrate. Consecutive adjustments of the matching network controls and the crystal driver control enabled precise kilovolt levels and zero reflected power* to be maintained.

*The zero reflected power was measured by a 0-500 watt Bird meter and had an accuracy of +2/-0 watts.

The vacuum pumping system consisted of a Sargent Welch turbo-molecular model 3102-D pumping system with an optimum vacuum of $<10^{-9}$ torr in the blanked off condition. An auxiliary mechanical pump was used to double pump shaft feedthroughs into the sputtering chamber. Either ultra-high purity argon or prepurified nitrogen could be bled into the chamber through a needle valve. A titanium gas purification element, heated to 900°C, was incorporated in the argon line to insure the purity of the argon; it could be isolated when nitrogen was used. Between the chamber support column and the turbo-molecular pump throat, a sputter-shutter throttling valve was positioned to regulate the pumping speed (i.e. chamber pressure). Adjustment of the needle valve and the sputter-shutter valve enabled a constant argon flow and pressure to be maintained in the chamber. Four vacuum gauges were employed to measure the chamber pressure from atmospheric to less than 10^{-9} torr:

Veeco TG-7 Thermocouple gauge	atm. - 10^{-3} torr
Veeco RG-86 Ionization gauge	10^{-1} - 10^{-6} torr
Pirani GP-210C gauge	10^{-1} - 10^{-4} torr
Veeco RG-81 Ionization gauge	10^{-3} - 10^{-10} torr

The Pirani gauge and the RG-86 ionization gauge were simultaneously used to measure the argon pressure during sputtering and the measured pressure had an accuracy of $1 * 10^{-4}$ torr (0.1 micron) at $3 * 10^{-3}$ torr.

The sputtering chamber consisted of three sets of electrodes and a rotatable substrate holder table. Two of the substrate electrodes were adaptable to substrate tuning or sputter etching while the other was permanently grounded and had a resistance heater for elevated temperature work. For all targets and substrates, the separation was approximately 10 cm. Both the targets and the substrates had independent shields that permitted a selected set of electrodes to be used. The target electrodes were water-cooled and the selected substrate electrode could be water-cooled. The feedthroughs for the vacuum gauges, gas inlets and electrical lines were situated on the column supporting the chamber.

The sputtering operation was divided into the three stages of pre-sputtering, sputtering and post-sputtering. The general sequence was to place the desired target(s) and substrate(s) in the chamber, pump to less than 6×10^{-7} torr, backfill with argon to the sputtering pressure and sputter at the desired parameters for the desired time, pump to less than 6×10^{-7} torr and finally backfill with nitrogen to atmospheric pressure and remove the substrate(s). Sputtering on the substrate commenced only after the target was cleaned, the sputtering parameters were stable and the color of the plasma indicated a high purity argon content. A detailed description of the three stages is given in Appendix I. The sputtering parameters that were closely

controlled, and their accuracy are:

Pressure	- ±0.1μ at 3μ
D.C. bias kilovoltage	- ±0.01 kv at 2 kv
R.F. kilovoltage	- ±0.02 kv at 2 kv
Reflected Power	- ±2 watts at 0 watts
Time	- ±2 sec.

Parameters of secondary importance that were recorded were the forward power and the shunt and series settings of the matching network. A typical data sheet for a sputtering run is shown in Appendix II. A five hour sputtering run was made for each new target in order to insure cleanliness before a controlled run was attempted.

B. Film Thickness Measurement

Film thickness was measured using the Tolansky multiple beam interference technique [24]. A partially masked glass slide was used as the substrate for the sputtered thin films (see Figure 3). The sputtered films were then coated with a uniform high reflectivity film by evaporating high purity (99.99%) aluminum wire to a thickness of 1000Å. This assured the fabrication of a highly reflective surface with a step height equal to that of the original sputtered film thickness. For the measurement, a Zeiss model WL research microscope was modified by the addition of a Leitz multiple beam interference attachment and a polaroid camera. A monochromatic sodium lamp was used as the light source and either a 75% or a 94% reflectance reference mirror was

used. The interference patterns were recorded photographically or were measured directly with a micrometer eyepiece. A column adapter to extend the eyepiece was used to compensate for the Leitz objective in the Zeiss microscope.* Film thickness was calculated from the amount of fringe offset according to the relation [24]:

$$d(\text{Å}) = m * (\frac{\lambda}{2}) \tag{3}$$

d = film thickness in Å

m = relative fringe displacement

λ = wavelength of light source in Å

The accuracy of the technique was estimated to be ±50Å or better.

C. Electron Microprobe Analysis

A standard ARL (Applied Research Laboratory) electron probe micro-analyzer modified with a Princeton Gamma Tech Model LS23 solid state detector was used in the point, matrix and scanning modes of operation. Qualitative analysis for all elements was accomplished with the solid state detector and quantitative analysis was performed with the spectrometers. The operating kilovoltage was based on the critical excitation voltages for the desired characteristic radiations and on the depth of x-ray emission. The characteristic radiation analyzed and their respective excitation

*Leitz objectives are for infinity corrected eyepieces while the Zeiss eyepieces have a finite focal distance.

voltages are:

Ni	K alpha, $Ni_{K\alpha}$	8.33	kv
Ni	L alpha, $Ni_{L\alpha}$	0.854	kv
Aℓ	K alpha, $A_{K\alpha}$	1.56	kv
Ta	L alpha, $Ta_{L\alpha}$	9.88	kv
Si	K alpha, $Si_{K\alpha}$	1.84	kv

The depth of x-ray emission was calculated by the theoretical relation [25]:

$$\rho R = 0.064 \; (V_o^{1.68} - V_c^{1.68}) \qquad (4)$$

where: ρ = density of material, gms/cc.

R = depth of x-ray emission, microns

V_o = probe operating voltage, kv

V_c = critical excitation voltage for line analyzed, kv

With glass as the substrate, Si K alpha radiation was used as an indication of the penetration of the sputtered thin film. The microprobe was operated at a kilovoltage that gave a depth of x-ray emission less than the film thickness. The sample current was either 1.00 nanoamperes for qualitative analysis with the solid state detector or that which gave a count rate greater than 10,000 cts./sec. for quantitative analysis. Fixed maximum counts were used for the solid state detector scans and fixed time was employed for the quantitative work.

The solid state detector scans were recorded on a strip chart and the principal peaks were noted from the multi-channel analyzer. The quantitative data from the spectrometers was recorded by teletype and, for large quantities of data, on paper tape. A standard Z.A.F. (atomic number, absorption, fluorescence) correction computer program for conversion of intensity to weight percent, written by J.I. Goldstein and P.A. Comella [26], was used in this analysis. The absorption coefficient for nickel L alpha radiation in nickel was that given by the more recent results of Colby [27] rather than that given in [26]. The absorption coefficients calculated by the computer program for the binary alloy matrices were checked using the relations and tables in the NASA Technical Note D-2984 [28]. The standards for the analysis of the Ni-Aℓ system were: pure Ni (99.97 wt.%), pure Aℓ (99.995 wt.%) and the 93.1 Ni - 6.9 Aℓ target alloy; for the Ni-Ta system, the standards were: pure Ni (99.97 wt.%), pure Ta (99.9^{+} wt.%) and the 65.2Ni - 34.8Ta target alloy. These standards were examined after metallographic polishing with 0.25μ diamond paste and the sputtered films were analyzed in the as-sputtered condition.

D. Transmission Electron Microscopy

Transmission electron microscopy was performed on an R.C.A. EMU-3G electron microscope during the early part

of this work and by a Phillips 300 electron microscope for the high temperature hot stage work towards the end of the research. The limiting operating characteristics for each microscope are:

	RCA EMU-3G	Phillips 300
Max. magnification (Normal Holder)	45,000x	180,000x
Max. magnification (Hot Stage)	28,000x	180,000x
Max. temperature of hot stage	700°C	1000°C
Max. kilovoltage	100	100

Both microscopes were operated at 100 kv and the temperature of the hot stage was measured by a Pt-Pt,10%Rh thermocouple. The only other major difference betwee the two microscopes is that the selected area aperture for diffraction is a sleeve type for the R.C.A. model and a fixed circular type, either 20 μ, 30 μ or 50 μ diameter, for the Phillips model. Standard preparation of the grids and support films was performed and films were then sputtered onto the grids. Normal operating procedures wer followed and both structure and diffraction were monitored during the hot stage work.

RESULTS AND DISCUSSION

General

Several sets of controlled runs were made to determine the relationship between the sputtering parameters and the material deposited. Three sets of runs were made where a single target, the 93.1Ni - 6.9Aℓ alloy target, was used and the sputtering parameters were varied. Specifically, Table V shows the data for the runs made with time as the variable; Table VI gives the data for the runs with the D.C. bias kilovoltage as the variable; and Table VII lists the data for the runs where the argon pressure was the variable. A set of four runs was made for each target with the sputtering parameters held constant. Each set can be separated into two short runs, for which the data is given in Table VIII and Table IX, to show the deposition rate relation with respect to the target material and two long runs, for which the data is given in Table X and Table XI, for chemical analysis by the electron microprobe. The sequence of the four runs from each target was first a two-hour run, then a ten-minute run, followed by a one-hour run and finally a five-minute run. Additional runs as given in Table XII were made from the pure aluminum target, the pure nickel target, the 93.2Ni - 6.8Aℓ plasma-sprayed target, the 93.1 Ni - 6.9Aℓ alloy target and the 65.2Ni - 34.2Ta alloy

target for the transmission electron microscopy work.

Deposition Parameters

The first set of results to be analyzed is the set given in Table V with the only controlled variable being the time of deposition. The D.C. bias kilovoltage and the argon pressure were very tightly controlled with a maximum error of ± 0.01 kv and ± 0.05 * 10^{-3} torr respectively. With "perfect" matching for each run, the R.F. kilovoltage is not constant and the average values given in Table V vary from a low of 2.44 kv (run #77) to a high of 2.59 kv (run #80). Figure 5 is a set of plots of the R.F. kilovoltage with respect to time for each run. The R.F. kilovoltage with an error of ± 0.02 kv is fairly constant during any run. The slight decrease at the start of some runs is due to a pressure decrease from 2.95 * 10^{-3} torr to 2.90 * 10^{-3} torr and, as will be shown in later results, the R.F. kilovoltage is somewhat sensitive to the argon pressure. With tight control maintained on the D.C. bias kilovoltage and the argon pressure, the variation in the magnitudes of the average R.F. kilovolt values show no correlation to these two major deposition parameters and no relation to the other deposition parameters of time, forward power and reflected power. Thus the average R.F. kilovolt variation from run to run is due to variations in the external matching network as substantiated by the slightly different matching network settings for identical time, power, D.C.

bias kilovoltage and argon pressure parameters. A change in the R.F. kilovoltage from the low of 2.44 kv to the high of 2.59 kv represents a change of approximately 7%. By considering, as an example, a 0.10 kv difference from 2.50 R.F. kv to 2.60 R.F. kv with a constant D.C. bias kilovoltage of 2.00 kv, these two conditions can be expressed by assuming a sinusoidal target voltage as:

$$V_1 = 2.50 \sin \omega t - 2.00 \quad (5)$$

$$V_2 = 2.60 \sin \omega t - 2.00 \quad (6)$$

The major difference in the two relations as shown in Figure 6 are the magnitude of the R.F. voltage and the time in the positive voltage region. For equation (5), 0.2048 of the cycle is positive and for equation (6), 0.2206 of the cycle is positive; a difference of 1.58 percent of a cycle. Because of this small change and due to the facts that the target voltage is not sinusoidal and that the positive part is "clipped" [29], the change is negligible. Thus, it can be concluded that the noted variation in the magnitude of the average R.F. kilovoltage from run to run is insignificant and that the deposition conditions are the same for all eight runs. Taking a weighted average of the R.F. kilovoltages, the eight runs given in Table V represent the following deposition conditions:

2.01 D.C. bias kilovolts
2.50 R.F. kilovolts
2.9 * 10^{-3} torr argon pressure
255 watts forward power
0 watts reflected power
93.1Ni - 6.9Aℓ alloy target
Substrate water cooled & grounded

With constant deposition conditions established for all runs, Figure 7 shows the increase in film thickness as a function of time. The curve is non-linear up to approximately 1000Å or 15 minutes and shows an increase in the deposition rate from an initial value of 66Å/min. to 131Å/min. The film thickness is dependent on the sputtering and deposition rates which in turn depend upon the unmeasured parameters of target temperature, substrate surface temperature and potential of the substrate surface.

The sputtering rate is a function of target composition, ion current flux and sputtering yields for each specie as given by equation (1) in the introduction. The net sputtering rate from the alloy target may be expressed as:

$$\dot{N} = \dot{N}_{A\ell} + \dot{N}_{Ni} \quad (7)$$

$$\dot{N} = (x_{A\ell} * J * y_{A\ell}) + (x_{Ni} * J * y_{Ni}) \quad (8)$$

$$\dot{N} = J * (x_{A\ell} * y_{A\ell} + x_{Ni} * y_{Ni}) \quad (9)$$

For the conditions of this set of runs, the ion current flux, J, and the atomic fractions of nickel, x_{Ni}, and

aluminum, $x_{A\ell}$, are constant. The sputtering yields of nickel and aluminum must therefore be studied. Although the target is water cooled, it does heat up slightly to possible around 150°C. This increase in target temperature is significant with respect to the low melting point specie aluminum but is negligible with respect to nickel. Because the target is nickel based (86.11 atomic % Ni) a two fold increase in the sputtering yield of nickel would be required to account for the two fold increase in the deposition rate. This increase in the sputtering yield of nickel due to a temperature increase is not plausible and later microprobe results show that the sputtering yield of aluminum is not large. Thus, the target temperature can be eliminated as a cause of the initial non-linear behavior. A second point with respect to the sputtering yield and the associated sputtering rate is that a thin oxide film on the target surface would give rise to an initial low deposition rate. This factor may be eliminated because for all runs, the target was precleaned for five minutes before deposition and some of the runs were made approximately thirty minutes after the previous run without breaking the vacuum. For thirty minutes at 10^{-6} torr, if an oxide film did form, it would be very thin and would be sputtered off in the five-minute pre-sputter. It must be concluded that the sputtering yields are fairly constant. Therefore, the net sputtering rate for all runs is the same and does not give rise to

the non-linear thickness versus time curve.

The deposition rate is related to the primary quantities of the sputtering rates and the sticking coefficients of each specie and the secondary quantities of the resputtering and evaporation rates of each specie as given in equation (2) in the introduction. The net deposition rate from the 93.1Ni - 6.9$A\ell$ alloy target may be expressed as:

$$\dot{D} = \dot{D}_{A\ell} + \dot{D}_{Ni} \tag{10}$$

$$\dot{D} = (s_{A\ell}\dot{N}_{A\ell} - N'_{A\ell} - \mu_{A\ell}) + (s_{Ni}\dot{N}_{Ni} - \dot{N}'_{Ni} - \mu_{Ni}) \tag{11}$$

$$\dot{D} = (s_{A\ell}\dot{N}_{A\ell} + s_{Ni}\dot{N}_{Ni}) - (N'_{A\ell} + N'_{Ni} + \mu_{A\ell} + \mu_{Ni}) \tag{12}$$

The sputtering rates $\dot{N}_{A\ell}$ and $\dot{N}_{Ni}$ are constant so they may be eliminated from consideration. The other six parameters must be investigated to see which may cause the initial non-linear behavior. Analogous to the target, the substrate is water cooled but does heat up to possibly as high as 200°C. The substrates were glass slides and being good thermal insulators, the substrate surface may heat to higher temperatures. Assuming the maximum substrate temperature as 250°C (it could be as great as 500°C), this would give a zero evaporation rate for nickel, μ_{Ni}, and a small evaporation rate for aluminum, $\mu_{A\ell}$. The effect of these two parameters is negligible and would be opposite to the observed trend in that the deposition rate would decrease as the deposition time increased (i.e. as the substrate heated up).

More importantly, the substrate temperature has a significant effect on the sticking coefficients. The sticking coefficients of nickel and aluminum are also dependent on the nature of the substrate. Initially, the substrate is cold and amorphous glass and later the substrate is warm and is a nickel-based thin film. An increase in substrate surface temperature from 20°C to 250°C will affect the sticking coefficient of aluminum. The increase in substrate temperature will lower the sticking coefficient of aluminum and will result in a lower deposition rate. Thus for the reason that the film is nickel-based and a substrate temperature effect on the sticking coefficient would give a trend opposite to that observed, the increase in substrate temperature may be neglected. The change in substrate from amorphous glass to a metal film, however, will give a major effect on both sticking coefficients. Very little data is available on sticking coefficients because of the many possible combinations of substrate surfaces and vapors. It is generally accepted that for low relative substrate temperatures, a metal vapor deposited on a substrate of the same material will have a sticking coefficient of unity. Yang et al.[30] have found that for a substrate temperature of 20°C (T_s/T_{mp} = 0.237), the deposition of silver gives a sticking coefficient of 1.00 on silver and of 0.31 on glass. The sticking coefficient is also dependent on film thickness and should approach unity for self-deposition. For the linear portion

of the curve of Figure 7 where the deposition rate is constant at 131 Å/min. and the relative substrate temperature for nickel is low, $T_s/T_{mp} \approx 0.3$, the sticking coefficient of nickel may be taken as unity. The sticking coefficient of aluminum in this region is less than unity because the relative substrate temperature is high at approximately $T_s/T_{mp} \approx 0.56$. Taking the major change in deposition rate as due to a change in the sticking coefficient of nickel, this would make the initial sticking coefficient of nickel on glass on the order of 0.5 as shown in Appendix III. Qualitatively this value is quite reasonable and an increase in the nickel sticking coefficient from 0.5 to 1.00 as the substrate becomes a continuous thin film is consistent. Johnson [31] has shown a similar change in the sticking coefficient and deposition rate for cadmium sulfide using a vacuum microbalance technique. The sticking coefficient is also dependent on the net sputtering rate and the impurity gas concentration so these conclusions are valid only for 2.01 D.C. bias kilovolts and $2.9 * 10^{-3}$ torr argon pressure. A final point concerns the resputtering rates given in equation (12) which are dependent on the substrate surface potential. If the substrate surface and the plasma are at ground potential, then the resputtering rates will be zero and the non-linear behavior of Figure 7 is due solely to a change in the sticking coefficients. However, because the substrate is a dielectric and an R.F. field is applied, the

substrate may acquire a negative potential and attract low energy ions. Therefore until the film is continuous and the substrate potential is at ground, the resputtering rates will be non-zero. A positive plasma potential will similarly give a non-zero resputtering rate. An initial resputtering rate will give a low deposition rate and complement an initial low sticking coefficient. Although the surface potential was not measured, it will be low and the resputtering rate due to the attraction of low energy ions will be low and possibly negligible.

In summary, Figure 7 shows that for constant sputtering conditions, the deposition rate is not constant and increases from 66Å/min. to 131Å/min. This increase is not related to any sputtering parameters but to a significantly large increase in the sticking coefficient.

The second set of runs to be analyzed is that given in Table VI where the D.C. bias kilovoltage is varied from 0.45 kv to 2.50 kv. For these runs, the argon pressure was tightly controlled at $2.9 * 10^{-3}$ torr with a maximum error of $0.05 * 10^{-3}$ torr and the power level was set to give a desired D.C. bias kilovoltage with an accuracy of ±0.01 kv. The associated R.F. kilovoltage was very stable during each run, varying less than 0.03 kv from the average value. The power level is very dependent on the degree of matching and at the low power levels, the system was run slightly unmatched because the crystal driver control is too coarse

to set the proper power level. As an example, for run #82 the system could be matched at the fixed driver control setting to give zero reflected power ($\approx$ 200 watts forward power) but the D.C. bias kilovoltage would be higher than 1.50 kv. It is also important to note that the power readings are very misleading when the system is unmatched. For example, the forward power for run #85 is approximately twice that for run #83 and the reflected power for run #85 is half that for run #83 while the R.F. and D.C. bias kilovoltages are the same and the deposition rate, as will be shown later, is identical for each run. This last point is a clear indicator that the primary electrical parameters to be measured are the R.F. kilovoltage and the D.C. bias kilovoltage rather than the R.F. power input. The final deposition parameter, time, was held at ten minutes for the high deposition rates and was increased to longer times for the low D.C. bias kilovoltages, i.e. 1.00 kv, 0.50 kv and 0.45 kv, because of the difficulty of measuring the thickness of very thin films by the multiple beam interference technique.

As can be noted from Table VI, there is a corresponding increase in the R.F. kilovoltage as the D.C. bias kilovoltage increases. Figure 8 is a plot of the average R.F. kv as a function of the D.C. bias kv showing the relation is slightly non-linear. The dashed line in Figure 8 represents equivalent R.F. and D.C. bias kilovoltages.

The relationship between the applied R.F. kilovoltage and the D.C. bias kilovoltage depends on the capacitance of the target and external equipment and on the plasma characteristics. A simple electrical schematic of the sputtering system and the location at which the R.F. kilovoltage and the D.C. bias kilovoltage were measured is shown as follows:

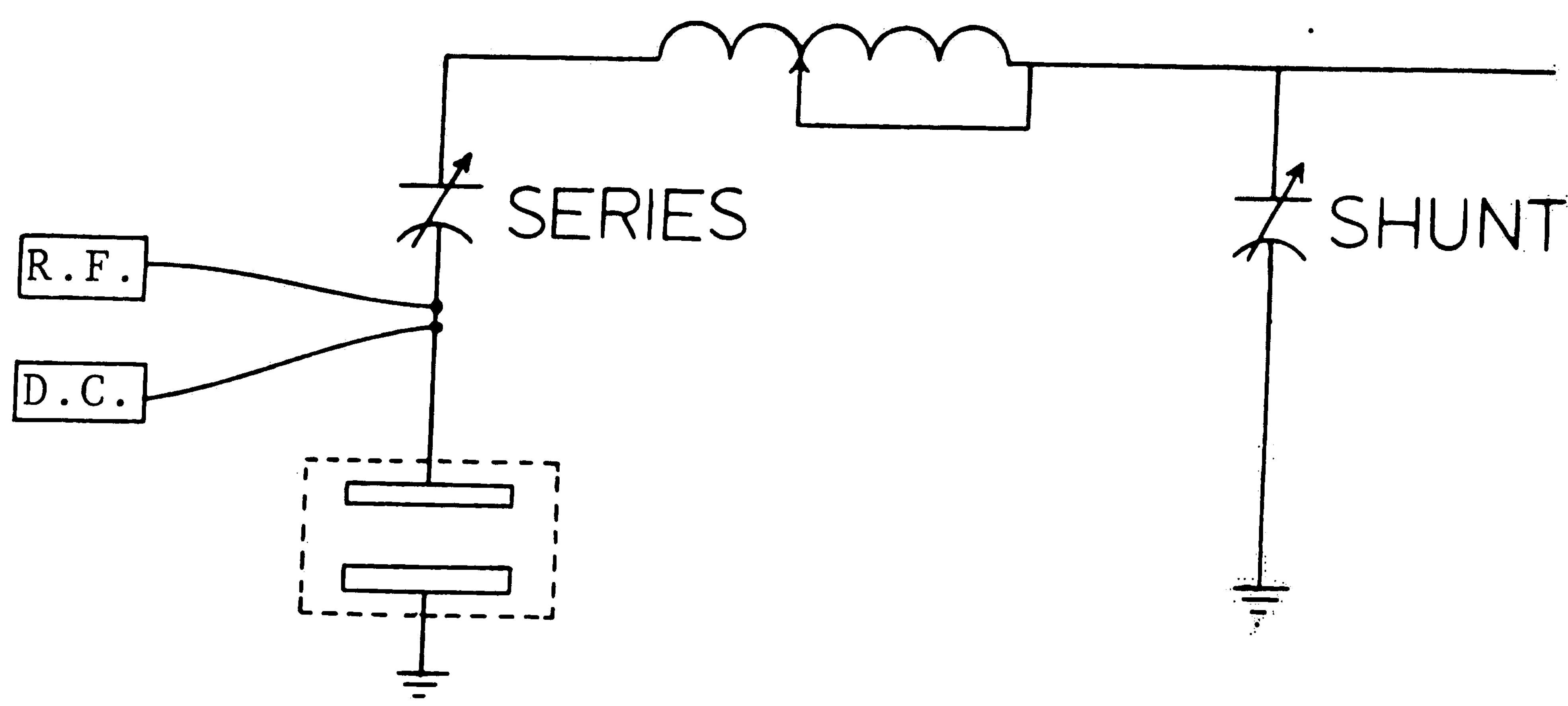

Not included in the schematic are the capacitances of the plasma, of the target, of the insulation between the target and the chamber and of the feeds from the matching network to the target. As written in equation (5) and (6), the voltage applied to the target with respect to ground is:

$$V = V_{RF} \sin \omega t - V_{DC} \tag{13}$$

Tsui [32] has shown that by assuming a linear electric field in the R.F. dark space, the D.C. bias value will reach 0.999928 of one half the R.F. peak-to-peak voltage, i.e. $V_{DC}/V_{RF} = 0.999928$. From Figure 8, the measured R.F.

kilovoltage, $V_{RF}|_m$, does not equal the D.C. bias kilovoltage as one would expect. The difference between the two results is that Tsui took the plasma at ground potential, i.e. $V_p = o$. Because the target is a metal with low capacitance, the measured R.F. kilovoltage does not have to be modified by a capacitance ratio as Butler and Kino [33] did for their work. The R.F. meter does read the actual target R.F. voltage and thus the plasma is not at ground potential but at a positive potential with respect to ground. Similar to the analysis by Brodie et al. [34], the target voltage with respect to ground is:

$$V = V_{RF}|_m \sin \omega t - (V_{DC} + V_p - \nu) \qquad (14)$$

where ν is the maximum positive potential of the target with respect to the plasma. By Tsui's results, $\frac{V_{RF}|_m}{V_{DC} + V_p} = 0.999928 \approx 1$ and ν is very close to zero. The potential gradient of the R.F. dark space is $(V_{DC} + V_p) \approx V_{RF}|_m$ and it is this voltage which accelerates the argon ions to the target. Stray capacitances between the meter position and the target surface are not included in this analysis; however, these are in parallel with the target and thus do not alter the target voltage. Thus the increase of the R.F. kilovoltage over the D.C. bias kilovoltage as shown in Figure 8 is due to an elevation of the plasma potential above ground and the magnitude of the R.F. kilovoltage is

equal to the <u>net</u> D.C. bias kilovoltage which accelerates the ions.

The sputtering rate and the deposition rate as a function of the <u>net</u> D.C. bias kilovoltage depend on the variation of the three primary parameters of ion current, sputtering yield and sticking coefficient. Figure 9 shows the target voltage variation based on equation (14). As Anderson et al. [35] have shown for a dielectric target, the relation between the applied voltage and the ion current, which is assumed independent of time, is given by:

$$\frac{dV}{dt} = I_{ion}/C \qquad (15)$$

where C is the capacitance of the dielectric target. For R.F. sputtering of metals, C is the capacitance of a fixed blocking capacitor. This gives the relation that $\frac{dV}{dt} \propto I_{ion}$ or that the ion current is directly proportional to the R.F. target voltage which is approximately equal to the net D.C. bias voltage, i.e. $I_{ion} \propto V_{RF}$. For the purpose of simplifying the present analysis, the sputtering yields of nickel and aluminum can be assumed to be equal to that for the pure species even though the target is a solid solution of aluminum in nickel. The data for the variation of the sputtering yield for Ni, $A\ell$, and Ta by Ar^+ ions with respect to the argon ion energy is given in Table XIII. The threshold energy of argon, defined as the minimum argon ion energy to sputter a specie, is given in Table XIV for Ni,$A\ell$

and Ta [42]. The sputtering yield data is scarce for the ion energy range of this study. Carter and Colligon [43] have made a complete review of the present sputtering theories and the expressions for the sputtering yield. Based on the published data of Table XIII, the sputtering yield data for nickel bombarded by nitrogen according to Bader et al. [44] and the sputtering yield being proportional to the natural logarithim of the ion energy, a simple analysis is given in Appendix IV to approximate the sputter yield of nickel and aluminum as a function of the argon ion energy. Figure 10 is a graph of the approximate variation of the sputtering yield with ion energy along with the published values of Table XIII plotted as points. The final primary parameter, the sticking coefficient, was found in the previous section to vary initially from 0.5 to 1.0 for the nickel specie. It can thus be concluded that the sticking coefficient for the nickel based alloy on glass will initially be approximately 0.5.

Figure 11 is a plot of the film thickness as a function of time for the different D.C. bias kilovoltage conditions. Initially, it can be noted that the deposition rate is identical for both the 10-minute and the 30-minute runs at 1.10 R.F./1.00 D.C. bias kilovoltages. At the low R.F. and D.C. bias kilovoltages, the deposition rate is low and consequently, the sticking coefficient, which depends in part on the film thickness rather than on the deposition

time, does not change very rapidly. As shown in Appendix V, the governing equations for this 93.1Ni - 6.9Aℓ alloy target for two target voltage conditions are:

$$i=1,2 \qquad \frac{x_{Ni|i}}{1-x_{Ni|i}} * \frac{y_{Ni|i}}{y_{A\ell|i}} = \frac{0.8611}{0.1389} \tag{16}$$

$$i=1,2 \qquad x_{A\ell|i} = 1 - x_{Ni|i} \tag{17}$$

$$\frac{D_1}{D_2} = \frac{s_{alloy|1}}{s_{alloy|2}} * \frac{V_{RF|1}}{V_{RF|2}} * \frac{x_{Ni|1}y_{Ni|1} + x_{A\ell|1}y_{A\ell|1}}{x_{Ni|2}y_{Ni|2} + x_{A\ell|2}y_{A\ell|2}} \tag{18}$$

Three major assumptions were made in this analysis:

(1) The resputtering and evaporation rates are negligible, i.e. $N'_{Ni} = N'_{A\ell} = \mu_{Ni} = \mu_{A\ell} = 0$.

(2) The sticking coefficient of nickel on glass is equal to the sticking coefficient of aluminum on glass which is thus equal to a sticking coefficient of the alloy on glass, i.e. $s_{Ni} = s_{A\ell} = s_{alloy}$.

(3) Steady state conditions exist at the target surface.

Taking the R.F. kilovoltage which is equal to the net D.C. bias kilovoltage, $V_{RF} \approx V_{DC} + V_p$, Table XV gives the sputtering yield from Figure 10 and the atomic fractions from equations (16) and (17) for each target voltage condition. If it is assumed that the sticking coefficient at the substrate is not affected by a voltage change at the target, then $s_{alloy|1}$ may be assumed equal to $s_{alloy|2}$. This is valid only for the initial deposition rate at $t = 0^+$ or

for steady state conditions at t >> 0. Equation (18) may then be solved with the data of Table XV. Because the initial deposition rate is known for the 2.52 R.F. kilovolt and the 1.10 R.F. kilovolt conditions (where short time data is available), equation (18) for $t = 0^+$ becomes:

$$\frac{\dot{D}_1|_{t=0^+}}{\dot{D}_2|_{t=0^+}} = \frac{V_{RF}|_1}{V_{RF}|_2} * \frac{x_{Ni}|_1 Y_{Ni}|_1 + x_{A\ell}|_1 Y_{A\ell}|_1}{x_{Ni}|_2 Y_{Ni}|_2 + x_{A\ell}|_2 Y_{A\ell}|_2} \tag{19}$$

This equation states that knowledge of the net D.C. bias voltage (the R.F. voltage) and the sputtering yields enables the calculation of the relative deposition rates. At the target voltage condition of 2.52 R.F. kv and 2.01 D.C. bias kv, the initial deposition rate was 66 Å/min. and at the target voltage condition of 1.10 R.F. kv and 1.00 D.C. bias kv, the initial deposition rate was 27.5 Å/min. By setting $\dot{D}_2|_{t=0^+}$ equal to either of these known rates, the deposition rate ratio can be calculated and a calculated $\dot{D}_1|_{t=0^+}$ can be found for each target voltage condition. Table XVI gives the results of equation (19) for both known initial deposition rates. Very good agreement is obtained for the two known conditions where the calculated values of 25.4 Å/min. and 71.3 Å/min. are very close to the experimental values of 27.5 Å/min. and 66 Å/min. Based on the calculated initial deposition rates, approximate film thickness versus time curves are drawn on Figure 11 for the conditions where only one data point is available.

For the 2.50, 2.01, 1.50 and 1.00 D.C. bias kilovoltage conditions, the film thickness for a deposition time of 10 minutes is experimentally known and by extrapolating the 0.50 and 0.45 D.C. bias kilovoltage data back to 10 minutes, the film thickness for these two conditions for a deposition time of 10 minutes can be found. Figure 12 is a plot of film thickness for a deposition time of 10 minutes as a function of the R.F. kilovoltage which is equal to the net D.C. bias kilovoltage. The calculated initial deposition rate from Table XVI is also plotted on Figure 12 and is analogous to a calculated film thickness for a deposition time of 10 minutes. Where the experimental data is available to compare to, i.e. 1.10 and 2.52 R.F. kilovolts, the initial deposition rate calculated from equation (19) and the data agree very well. As Figure 12 shows, the calculated initial deposition rate also agrees within experimental error with the data for the 0.56 R.F./0.50 D.C. bias and 0.45 R.F./0.45 D.C. bias conditions (extrapolated from 30 minutes and 20 minutes respectively). Figure 12 shows that at the higher R.F. kilovoltages, the experimental curve of film thickness deviates from the curve of the calculated film thickness at ten minutes based on the initial deposition rates. This deviation occurs because the sticking coefficient is increasing from its initial value of approximately 0.5 at a faster rate for the higher deposition rates. This is evident for the 2.52 R.F./2.01 D.C. bias

condition where the initial deposition rate of 66 Å/min. agrees very well with the calculated value but where the film thickness after ten minutes is significantly higher than would be expected (750 Å). The high value of film thickness for the 2.50 D.C. bias kilovoltage indicates that the sticking coefficient has changed rapidly in the ten minutes of deposition as shown in Figure 11 by the approximated thickness versus time curve. This behavior is to be expected because the film is 1280 Å thick and the sticking coefficient should be close to unity. The final point is that the slope of the initial deposition rate versus R.F. kilovoltage curve of Figure 12 is a constant value of 29.6 Å/min. per R.F. kilovolt. This is expected because the sputtering yield in this ion energy region is approximately $(a - \frac{b}{V})$ as shown in Appendix IV and the ion flux is proportional to V (equation 15). Thus with $\dot{D} = s*J*y$ where $J = k*V$ and $y = a - \frac{b}{V}$, the derivative of $\dot{D}$ with respect to V is:

$$\frac{d\dot{D}}{dV} = s*k*a = \text{constant} \tag{20}$$

By the analysis of the data for the 2.01 D.C. bias kilovoltage condition as a function of time, as previously discussed, the sticking coefficient for nickel increases from about 0.5 to 1.0. Therefore under steady atate condition, the deposition rate can be expected to be approximately twice the initial deposition rate as given in Table XVI and the rate of change of the deposition rate with R.F. kilovoltage

should be 59.2 $\frac{\text{Å/min.}}{\text{R.F.kv}}$ to be consistent with the change in the sticking coefficient.

In summary, several major points are noted from this analysis. First, the R.F. kilovoltage is greater than the D.C. bias kilovoltage at higher kilovoltages due to the increase in plasma potential above ground; thus the R.F. kilovoltage can be taken as the net D.C. bias kilovoltage. Second, the three governing equations (16), (17) and (18) express very well the relation between the initial deposition rates for different sputtering conditions at constant sputtering pressure. Third, the initial deposition rate is linearly related to the R.F. kilovoltage (net D.C. bias kilovoltage) with a slope of $\frac{29.6\text{Å/min.}}{\text{R.F. kv}}$ over the kilovoltage range investigated. Finally, the sticking coefficient and the resulting variation in the deposition rate change more rapidly at the higher sputtering rates.

The third set of runs to be studied is the set given in Table VII where the argon pressure varied from $2.9 * 10^{-3}$ torr to $34.0 * 10^{-3}$ torr. "Perfect" matching was achieved for each condition and the two deposition parameters of D.C. bias kilovoltage and time were tightly controlled at 2.01 ± 0.01 kv and 10 minutes ±2 seconds respectively. The average values of the R.F. kilovoltage show a slight increase with an increase in the pressure. As substantiated by the variation of the R.F. kilovoltages for the constant deposition conditions of the runs given in Table V, this

increase from 2.52 R.F. kv at $2.9 * 10^{-3}$ torr to 2.72 R.F. kv at $34.0 * 10^{-3}$ torr is not significant and is due to slight changes in the matching network as related to the power input. Although power is a deposition parameter of secondary importance and the exact magnitude of the forward power may be misleading, as previously noted, an increase in power (by the crystal driver control of the R.F. generator) is required at the higher pressures to maintain the 2.01 D.C. bias kilovoltage condition. This indicates that for <u>constant power</u> conditions, an increase in pressure results in a lower D.C. bias and R.F. kilovoltage. With <u>constant kilovoltage</u> conditions, the increase in power corresponds to an increase in current which to a first approximation means an increase in the ion flux.

The sputtering and deposition rates as a function of the argon pressure for constant target voltage conditions are complicated by plasma physics considerations. The ion flux depends not only on the applied field but also on the ionization process and the mean free path of the particles. At low pressures and at constant voltage conditions where the sputtering yield is not a function of pressure, the ion flux, J, increases as the pressure increases [47]. This results in a linear relation between the sputtering rate and the pressure (equation 9). At high pressures, the mean free path of the particles is small and sputtered atoms are able

to diffuse back to the target which results in a decrease in the sputtering yield. As shown by Laegreid and Whener [39] for 150 ev argon ions bombarding nickel, the sputtering yield decreases at pressures greater than approxmately 20 * 10^{-3} torr. Thus at high pressures, the ion flux is high and the sputtering yield is low. Figure 13 is a plot of the film thickness for the ten minute runs of Table VII as a function of the argon pressure. The analysis is complicated by the change in the sticking coefficient with respect to time as discussed in the first section. All of the ten minute runs except that at the pressure of 2.9 * 10^{-3} torr give a film thickness greater than 1000 Å and consequently the sticking coefficient for each has reach unity. At the high deposition rates, the sticking coefficient changes rapidly and the comparison of thickness data for constant short time is no longer very accurate. Specifically, quantitative evaluation of the process cannot be made for this case due to the unknown variation of the sticking coefficient with time as a function of the deposition rate, the unknown variation of the sputtering yield with pressure and the unknown variation of the ion flux with the pressure. It was shown that for the conditions of 2.01 D.C. bias kilovolts and 2.9 * 10^{-3} torr argon pressure, the deposition rate increases from initially 66 Å/min. to a steady state value of 131 Å/min. If the linear portion of Figure 13 is extrapolated back to 2.9 * 10^{-3}

torr, the film is between the limits of 660Å and 1310Å based on the deposition rates. Therefore, given an initial linear variation of the sticking coefficient with film thickness, which will be more salient at low deposition rates, Figure 13 shows an approximate linear variation between the film thickness, for a constant deposition time, and the argon pressure.

By analyzing the variation of the mean free path of gas particles and the R.F. sheath thickness with respect to pressure, some qualitative evaluation of the observed trend can be made. The standard relation for the mean free path of gas particles is [45]:

$$\lambda = \frac{kT}{p\pi\sigma^2\sqrt{2}} \tag{21}$$

where λ = the mean free path
p = the pressure
σ = the effective cross-section diameter
k = Boltzmann constant
T = the temperature.

The effective cross-section diameter of argon based on van der Wall's equation is 2.94Å [46]. With the pressure in 10^{-3} torr (microns) and the temperature as 298°K, the mean free path as a function of pressure is:

$$\lambda\ \left(\frac{\text{cm.}}{\text{molecule}}\right) = 11.362 * [p_{Ar}(10^{-3}\ \text{torr})]^{-1} \tag{22}$$

Figure 14 is a plot of equation (22) for the pressure range

studied. The variation of the R.F. plasma sheath thickness with pressure is a function not only of the density of ions but also of plasma-space charge relations. The density of ions is approximately equal to the density of gas particles which is given by equation (23):

$$\frac{n}{V} = \frac{p}{kT}$$

$$\rho \left(\frac{\text{molecules}}{\text{cm.}^3}\right) = 9.656 * 10^{15} \frac{p(10^{-3} \text{ torr})}{T(^\circ K)} \qquad (23)$$

The space charge conditions are given by the Langmuir-Child equation which relates the current to the voltage. The netdependence of the R.F. sheath thickness with pressure is approximately inverse, i.e. $x \propto \frac{1}{p_{Ar}}$, as noted by Levitskii [47]. However, Cannara and Crawford [48] have shown the complication is that for a constant target voltage, an increase in the pressure has a dual effect, i.e. to <u>decrease</u> the sheath thickness and to <u>increase</u> the ion current.

The sputtering rate is directly dependent on the ion current (equation (1)) and for R.F. sputtering without magnetic assistance, the ion current cannot be separately controlled. As shown in the previous section, the ion current for constant pressure conditions is directly related to the target voltage (equation (15)); however, the sputtering yield is also a function of voltage (Appendix IV). For constant target voltage, the ion current is not simply related to the pressure. Tsui [32] states that at the pressures of $2 * 10^{-3}$ torr to $20 * 10^{-3}$ torr, the majority of ions

originate at the ion sheath-plasma interface. This pressure range corresponds to a mean free path of 5.7 cm. to 0.57 cm. respectively. With the mean free path, λ, greater than or approximately equal to the sheath thickness, x, as determined visually (i.e. $\lambda > x$), it can be assumed that the ion current is proportional to the pressure (i.e. $I_{ion} \propto p_{Ar}$). By plotting the R.F. forward power, which is directly related to the ion current for constant target voltage and perfect matching, as a function of argon pressure, the relation is found to be linear up to approximately $20 * 10^{-3}$ torr as shown in Figure 15. At pressures greater than $20 * 10^{-3}$ torr, the mean free path becomes a factor of increasing importance because the sheath thickness will be on the order of or greater than the mean free path (i.e. $x > \lambda$). Thus the ion current will not be simply related to the ion density at the plasma-sheath interface (or to the argon pressure). Also the sputtering yield will decrease at these higher pressures due to the short mean free path and diffusion of sputtered atoms back to the target. Therefore, as the dashed line at the high pressures shows in Figure 13, the film thickness for ten minutes (which is related to the sputtering rate) should tend to increase at a slower rate.

In summary, although the film thickness data is complicated by a changing sticking coefficient, Figure 13 shows that the film thickness at ten minutes and hence the deposition rate increases as the pressure increases. As

qualitatively expected and as shown by the dashed lines in Figure 13, the film thickness for ten minutes and therefore the deposition rate is directly related to pressure below $20 * 10^{-3}$ torr and at higher pressures the rate of change of film thickness versus argon pressure tends to decrease.

Composition

The composition of the target materials for the runs given in Table X and XI was analyzed prior to determining the change in composition from the target to the sputtered thin films. Both the plate and plasma-sprayed targets were analyzed for composition and homogeniety and, in addition, the plate targets were analyzed for microstructural variations. The pure Ni, Ni-Aℓ alloy and Ni-Ta alloy target materials were metallographically polished and then etched with Marbles Etch*. Both the pure Ni and the Ni-Aℓ alloy possessed an equiaxed, fine grain, single phase structure. The Ni-Ta alloy had a fine precipitate structure with fine platelets or needles of a second phase. Chemical analysis of these three plate target materials was performed on the electron microprobe using the pure elements as the standards. The analysis showed that the pure Ni and the Ni-Aℓ alloy were homogeneous and of the composition given in Table IV, i.e. 100 wt.% Ni and 93.1 wt.% Ni - 6.9 wt.% Aℓ respectively. The analysis of the Ni-Ta alloy indicated 34.8 wt. % Ta

*Solution of 20 gms. of $CuSO_4$, 100 ml. H_2O, 100 ml. HCl, 200 ml. C_2H_5OH.

in the fine precipitate matrix while a composition of about 42 wt.% Ta was found for the second phase platelets indicating they were Ni_3Ta. The average composition of the Ni-Ta alloy is thus a little higher in tantalum than the value given in Table IV for the bulk alloy target.

For the plasma-sprayed targets, both qualitative and quantitative analyses were performed. Qualitative analysis for homogeniety was performed on small cut samples of the plasma-sprayed target material with the electron microprobe. The Ni-Aℓ samples showed a fairly uniform dispersion of aluminum particles with little agglomerated aluminum. This result is due to the finer size of the aluminum powder in comparison to that of the nickel powder as given by the sieve analyses listed in Table III. In contrast, the Ni-Ta samples showed significant inhomogeniety and agglomeration of tantalum. This was true especially for the higher tantalum content plasma-sprayed samples, even though both the nickel and tantalum powders have similar sieve analyses (Table III). Quantitative analysis for nickel was done by Coors/Spectro Chemical Laboratory using standard wet-chemical dimethlyglyoxime techniques. Two small samples of each of the plasma-sprayed specimens were analyzed; the stated accuracy for a duplicate analysis is ±0.15 wt.% Ni (absolute). Table XVII gives the results of the quantitative analysis and Figures 16 and 17 show the relation between powder composition and plasma-sprayed target

composition for the Ni-Aℓ and the Ni-Ta targets respectively.

From Figure 16, the agreement between the powder composition and target composition for the Ni-Aℓ plasma-sprayed targets is found to be very good. The Ni - 3.4Aℓ target possesses slightly higher aluminum in the plasma-sprayed target (3.88 wt.% Aℓ) than in the powder (3.4 wt.% Aℓ). This small deviation is probably due to inhomogeniety of the small plasma-sprayed specimen that was analyzed. It can be concluded that the average composition of the Ni-Aℓ plasma-sprayed target corresponds to the composition of the powder.

In complete contrast, the composition of the Ni-Ta plasma-sprayed samples show little agreement with the composition of the powder. As noted by the qualitative analysis with the electron microprobe, the Ni-Ta plasma-sprayed samples showed significant inhomgeniety and this is reflected in the lack of correspondence between the analysis of the plasma-sprayed samples and the composition of the powder. To better determine the relation between the Ni-Ta plasma-sprayed target composition and the powder composition, x-ray fluorescence analysis was performed on both the powders and the plasma-sprayed samples. The intensities of both the $Ta_{L_{\alpha 1}}$ and $Ta_{L_{\beta 1}}$ peaks were observed. The Ni-Ta powders showed the proper intensity relationships for tantalum contents of 2.4 wt.% Ta, 9.7 wt.% Ta and 17.1 wt.% Ta. However, while the plasma-sprayed Ni - 2.4Ta sample indicated

approximately the same tantalum intensity as the Ni - 2.4 wt.% Ta powder, both the Ni - 9.7Ta and the Ni - 17.1Ta plasma-sprayed samples gave approximately the same tantalum intensity which was slightly higher than that of the Ni - 9.7 wt.% Ta powder. Thus, in contrast to the wet chemistry analysis, the low tantalum content (2.4 wt.% Ta) plasma-sprayed target actually has an average composition equivalent to the 97.6 wt.% Ni - 2.4 wt.% Ta powder. The two higher tantalum content plasma-sprayed targets, where inhomogeniety is a major factor, have similar compositions. These compositions do not correspond directly to the composition of their respective powders, agreeing more closely with the wet chemistry analysis. There is fairly good agreement between the composition of the plasma-sprayed sample and the powder for five of the plasma-sprayed targets. Also, the desired composition is related to the percent surface area covered by each specie. For these two reasons, the composition of the plasma-sprayed target surface will be assumed equal to the composition of the powder. This assumption is in error for the two high tantalum plasma-sprayed targets and will be further discussed after the composition analysis of the sputtered thin films.

The chemical analysis of the sputtered films was made on the fairly thick films of the runs given in Tables X and XI. For these runs, the deposition conditions were approximately constant with the argon pressure controlled at

$2.9 * 10^{-3}$ torr and the D.C. bias kilovoltage at 2.01 kv. The R.F. kilovoltage showed only minor changes in magnitude from run to run with a low value of 2.30 R.F. kv (run #63) and a high value of 2.56 R.F. kv (run #29). With a deposition rate greater than 100 Å/min., the 60-minute runs gave a film thickness greater than 0.6 μ (6000 Å), and the 120-minute runs gave a films thickness greater than 1.2 μ (12,000 Å). The specific operation of the electron microprobe depended on the particular set of films analyzed, i.e. 0.6 μ Ni-Aℓ, 1.2 μ Ni-Aℓ, 0.6 μ Ni-Ta, or 1.2 μ Ni-Ta.

The operating kilovoltage which gave a depth of X-ray emission less than the film thickness was determined experimentally for the 0.6 μ and 1.2 μ films sputtered from the 98.8Ni - 1.2Aℓ plasma-sprayed target (runs #31 and #29). Figure 18 is a graph of the $Si_{K\alpha}$ intensity as a function of the microprobe kilovoltage for the two films on glass substrates and a bulk sample of "infinite" thickness (the Ni - 6.9Aℓ alloy standard). The bulk alloy indicates the $Si_{K\alpha}$ background intensity. Comparing the two films to this value, the $Si_{K\alpha}$ intensity from the 0.6 μ and 1.2 μ films is greater for kilovoltages greater than about 13.8 kv and about 20.8 kv respectively. From equation (4) and with the critical voltage set at that for Si_K ($V_c|_{Si_{K\alpha}} = 1.84$) and the density set at that for pure nickel ($\rho_{Ni} = 8.90$), the calculated kilovoltages for a depth of X-ray emission of 0.6 μ and 1.2 μ are 14.2 kv and 21.3 kv respectively. These

compare favorably with the experimental values.

For the lower energy radiation of $A\ell_{K\alpha}$ ($V_c|_{A\ell_{K\alpha}}$ = 1.56) and $Ni_{L\alpha}$ ($V_c|_{Ni_{L\alpha}}$ = 0.854), the kilovoltages for a depth of x-ray emission of 0.6 μ and 1.2 μ are slightly lower than that for $Si_{K\alpha}$. These are 14.1 kv and 21.2 kv for $A\ell_{K\alpha}$ and 14.0 kv and 21.2 kv for $Ni_{L\alpha}$. The higher energy radiation of $Ni_{K\alpha}$ ($V_c|_{Ni_{K\alpha}}$ = 8.33) and $Ta_{L\alpha}$ ($V_c|_{Ta_{L\alpha}}$ = 9.88) would require much higher operating microprobe voltages to achieve a depth of x-ray emission of 0.6 μ and 1.2 μ. The 0.6 μ films can thus be analyzed at a kilovoltage of 13 kv or lower and the 1.2 μ films at a kilovoltage of 20 kv or lower without penetration of the beam through the film into the glass substrate.

The actual operating kilovoltages finally used for analysis were chosen such that they were less than the kilovoltage that would cause complete penetration of the thin film and at least twice as large as the critical excitation kilovoltage, V_c, of the desired characteristic radiation, i.e. $V_o/V_c > 2$. This was so that intensities significantly larger than background would be produced and so that analysis could be carried out in reasonable time.

The characteristic radiations used for the Ni-Aℓ alloy thin films were $Ni_{K\alpha}$, $Ni_{L\alpha}$ and $A\ell_{K\alpha}$ with critical excitation voltages of 8.33 kv, 0.854 kv and 1.56 kv respectively. These films were analyzed under the following conditions:

0.6 μ thick film by $Ni_{L\alpha}$ and $A\ell_{K\alpha}$ at 8 kv

1.2 μ thick film by $Ni_{L\alpha}$ and $A\ell_{K\alpha}$ at 8 kv

1.2 μ thick film by $Ni_{L\alpha}$ and $A\ell_{K\alpha}$ at 20 kv

A kilovoltage of 8 kv was chosen because it is just below the Ni K excitation voltage. Thus $Ni_{K\alpha}$ and $Ni_{K\beta}$ will not be excited and will not fluoresce $Ni_{L\alpha}$ and $A\ell_{K\alpha}$. The results of the analyses at 8 kv and 20 kv on the two-hour 1.2 μ thick films for all the Ni-Aℓ targets are shown in Figure 19. With the two differences being the depth of penetration and the nickel characteristic radiation used, both operating conditions gave the same composition for each film.

The characteristic radiations used for the Ni-Ta alloy films were $Ni_{K\alpha}$ with $V_c|_{Ni_{K\alpha}}$ = 8.33kv and $Ta_{L\alpha}$ with $V_c|_{Ta_{L\alpha}}$= 9.88 kv. Because the $Ta_{L\alpha}$ critical voltage is quite high, only one analysis was made under the following condition:

1.2 μ thick film by $Ni_{K\alpha}$ and $Ta_{L\alpha}$ at 20 kv

The possibility of analysis of tantalum at low kilovoltages using $Ta_{M\alpha_1}$ was eliminated because the computer program, used to convert intensity to weight percent, could not analyze M lines. Thus the 0.6 μ and the 1.2 μ thick Ni-Aℓ thin films (Table X) were analyzed under two different probe operating conditions and the 1.2 μ thick Ni-Ta thin films (Table XI) were analyzed at only one operating condition.

Considering first the Ni-Aℓ system, Table XVIII gives the weight percent aluminum in the sputtered thin

films obtained by microprobe analysis using the 93.1Ni - 6.9Aℓ alloy as the standard. The analysis using the pure element standards gave similar results and the combined analyses for wt.% Ni and wt.% Aℓ gave a total composition close to 100 wt.%. The data of Table XVIII, from which Figure 19 was drawn, show the composition is uniform in the thin films. Preliminary ion microprobe results [49] similarly show a uniform composition in the film. Figure 20 is a plot of the average aluminum content of the sputtered films as a function of the aluminum content of the target. The dashed line in Figure 20 represents equivalent aluminum contents in the target and sputtered film; all of the analyses gave a lower aluminum content in the sputtered film than in the target.

The lower aluminum content in the thin films is thought to be caused by two factors. First, the sputtering yield of aluminum is lower than that of nickel. Secondly, the sticking coefficient of aluminum is less than that of nickel which is approximately unity.

The highest aluminum content in a sputtered thin film results from the 93.1Ni - 6.9Aℓ alloy target. As discussed previously, for this alloy target, the sputtering rate of each specie is proportional to the bulk target composition due to a change in the surface composition. The change from 6.9 wt.% Aℓ in the target to 3.9547 wt.% Aℓ in the sputtered film thus gives an aluminum sticking

coefficient of approximately 0.55 as shown in Appendix VI. With a substrate temperature of about 250°C and a relative substrate temperature with respect to aluminum of $T_s/T_{mp} \approx$ 0.56, an aluminum sticking coefficient of 0.55 is quite reasonable. Thus for the above common condition of deposition for the Ni-Aℓ targets, the sticking coefficient of aluminum can be assumed to be in the range of 0.55.

The Ni-Aℓ plasma-sprayed targets are bi-metal targets of pure nickel and pure aluminum and thus each element sputters as the pure specie according to the surface area covered by each specie. This is in contrast to the alloy target where the surface composition is not the bulk target composition but adjusts according to the sputtering yields of each specie, as shown in Table XV. For the plasma-sprayed targets, the sputtering rate of each specie is governed by the area covered by each specie and by the sputtering yield of each specie. Thus the change in composition from the plasma-sprayed target to the sputtered film depends not only on the sticking coefficient, but also on the sputtering yields. This is substantiated by the 3.9 wt.% Aℓ in the thin film sputtered from the 93.1Ni - 6.9Aℓ alloy target as compared to the 1.5 wt.% Aℓ in the thin film sputtered from the comparable 93.2Ni - 6.8Aℓ plasma-sprayed target. The four circles of Figure 20 correspond to the plasma-sprayed targets and show a fairly linear relationship significantly depressed from the dashed line.

For steady state conditions and negligible evaporation and resputtering rates, the deposition rate of each specie may be expressed using equation (1) and (2) as:

$$\frac{\dot{D}_{A\ell}}{\dot{D}_{Ni}} = \frac{s_{A\ell}}{s_{Ni}} * \frac{y_{A\ell}}{y_{Ni}} * \frac{x_{A\ell}}{x_{Ni}} \quad (30)$$

The sticking coefficients should be dependent only on the substrate conditions which are common for all the runs. From the analysis of the thin films sputtered from the Ni-$A\ell$ alloy target, $s_{A\ell}$ and s_{Ni} can be assumed to be 0.55 and 1.00 respectively. As discussed previously, the composition of the plasma-sprayed target is assumed equal to the composition of the powder. Using equation (30), the sputtering yields given in Figure 10 result in a calculated aluminum content higher than experimentally measured. Also noted previously, a target temperature of 150°C will have an effect on the sputtering yield of aluminum. This factor was considered negligible on the variation of film thickness with time and was not required for the analysis of the aluminum sticking coefficient from the alloy target (Appendix VI). The target temperature factor is, however, particularly important for the analysis of the plasma-sprayed target where the configuration of aluminum in the target is small particles of pure aluminum. As discussed by Carter and Colligon [43], an increase in target temperature will lower the sputtering yield of a specie. A target

temperature of 150 C will have a negligible effect on the sputtering yield of nickel (T_{mp} = 1453 °C) but may significantly decrease the sputtering yield of aluminum (T_{mp} = 660 °C). For example, by considering the 95.4Ni - 4.6Aℓ plasma-sprayed target and again using equation (30), a sputtering yield of aluminum of approximately 1.0 is necessary to give a film composition of 1.134 wt.% Aℓ (Table XIV). An aluminum sputtering yield of 1.0 is much lower than the value given in Figure 10 but is plausible since the target temperature is not known exactly and may be greater than 150 °C. Thus the difference in the sputtering yields of nickel, 2.4, and aluminum, 1.0, and the difference in sticking coefficients of nickel, 1.0, and aluminum, o.55, result in a large drop in the aluminum content from the plasma-sprayed target to the sputtered thin film.

The complete microprobe analysis of the sputtered Ni-Ta thin films is given in Table XIX with respect to both the pure element standards and the 65.2Ni - 34.8Ta alloy standard. The agreement between both analyses is very good. The preliminary ion microprobe results [49] also show a uniform composition in the Ni-Ta films as in the Ni-Aℓ films. The consistent decrease in the total weight percent with the increase in the tantalum content of the thin film occurs because the computer program did not correct for a third element, argon; this factor will be verified and discussed later. Figure 21 is a plot of the

average tantalum content of the sputtered film as a function of the tantalum content of the target. For all the Ni-Ta plasma-sprayed targets, the tantalum content of the sputtered films is lower than that of the target while for the Ni-Ta alloy target, the tantalum content of the sputtered film is approximately the same as in the target.

As discussed previously, the Ni-Ta alloy target was analyzed to be 34.8 wt.% Ta in the fine precipitate matrix and about 42 wt.% Ta in the second phase platelets. The 36.7 wt.% Ta in the thin film sputtered from the Ni-Ta alloy target is in agreement with the target composition. Being an alloy target, the target surface composition adjusts to give the composition of sputtered particles equal to the bulk target composition. Thus the approximately equal compositions of the sputtered thin film and the target give an identical sticking coefficient for each specie. Nickel and tantalum have high melting points (Table I) and therefore a substrate temperature of 250°C is expected to have a negligible effect on the sticking coefficients. The sticking coefficient of both nickel and tantalum can thus be taken as unity.

If sticking coefficients of unity are assumed for both species, the change in composition from the plasma-sprayed targets to the sputtered thin films is due solely to the different sputtering yields of nickel and tantalum. The high melting points of nickel and tantalum also dictate

that a target temperature of 150°C will have no effect on the two sputtering yields. Because the target composition for the two high tantalum content plasma-sprayed targets is uncertain, only the data point on Figure 21 for the 9712Ni - 2.4Ta plasma-sprayed target is accurate. Analogous to equation (30) for the Ni-Aℓ targets, the deposition rate of each specie for the Ni-Ta targets can be expressed as:

$$\frac{\dot{D}_{Ta}}{\dot{D}_{Ni}} = \frac{s_{Ta}}{s_{Ni}} * \frac{y_{Ta}}{y_{Ni}} * \frac{x_{Ta}}{x_{Ni}} \qquad (31)$$

The sticking coefficients of nickel and tantalum are unity; the sputtering yields of nickel and tantalum are found from the data of Table XIII, and the sputtered film composition was determined experimentally (Table XIX). Since the total composition must be 100 wt.%, i.e.

$$x_{Ta} + x_{Ni} = 1, \qquad (32)$$

equation (31) can be solved for the "expected" target composition. Table XX gives the "expected" target composition, as calculated in Appendix VII using equations (31) and (32), along with the film and powder compositions.

The low tantalum plasma-sprayed target (2.4 wt.% Ta) shows good agreement between the "expected" composition and the powder composition. This behavior agrees with the X-ray fluorescence analysis and the previous conclusion that the target surface composition corresponds to the powder composition for this target. For the two high tantalum plasma-

sprayed targets, the "expected" target composition does not correspond very well with the powder composition. Qualitatively, the sputtered film composition and the resultant "expected" target composition agree with the X-ray fluorescence analysis and somewhat with the wet chemistry analysis in that both targets have similar compositions. The net conclusion is that the plasma-spraying operation for these two high tantalum content targets gave erratic composition results. Also, the inhomogeniety of tantalum in the target surface increases the inaccuracy of the target surface composition determination. Although the exact magnitude of the target surface composition is uncertain, it is clear from all of the analyses that the tantalum content of the target is greater than that of the sputtered film. Thus the difference in sputtering yields of nickel, 2.4, and tantalum, 0.98, result in the decrease in the tantalum content from the plasma-sprayed target to the sputtered thin film.

The possibility of a third element or of trace elements was investigated using the solid state detector of the electron microprobe. Three sets of samples consisting of the target material and the two-hour sputtered thin film from that target were analyzed. From the quantitative microprobe results, the basis for selection and the three sets are as follows:

Basis for Selection	Target	Thin Film
No Aℓ or Ta in film	Pure Ni	Run #33
Maximum Aℓ in film	93.1Ni-6.9A alloy	Run #68
Maximum Ta in film	65.2Ni-34.8Ta alloy	Run #73

The microprobe was operated in the scanning mode (8 μ by 10 μ area scanned) at 20 kv and 1 nanoampere.

The solid state detector scans, generated for a maximum of 50,000 counts, are shown for each set in Figures 22, 23 and 24. The quantitative analysis for each sample is given alongside the scan. The notation on each scan is the channel number of the multi-channel analyzer, the characteristic radiation corresponding to the channel and the intensity in counts. The oxygen peak noted in each scan is the background oxygen level and is not indicative of oxygen or oxides in the samples. Neglecting argon as an impurity, none of the scans showed any detectable impurity content with detection being on the order of 0.1 wt.% of an element. Comparing the solid state detector scan of the thin film to that of the target material, the pure Ni and the Ni-Aℓ sets are similar with a slight decrease in the intensity of aluminum for the Ni-Aℓ set. In contrast, for the Ni-Ta set of Figure 24, the thin film shows an appreciable amount of argon in addition to the change in intensity of the characteristic radiations of Ni and Ta. This argon content partially accounts for the total weight percent for the Ni-Ta films not equaling 100 wt.%. As will be shown by the

transmission electron microscopy work, the Ni-Ta thin films from this alloy target are partially amorphous in structure. This somewhat open structure is liable to entrap argon from the plasma. As will be discussed, tantalum tends to form an amorphous structure. Thus the gradual decrease in total weight percent (Table XIX) with increase in tantalum in the thin film is due to a change in density and an increase in argon content. The pure Ni and the Ni-Aℓ thin films are crystalline in structure from the transmission electron microscopy work. The solid state detection scans of these films (Figures 22 and 23) show no detectable argon content.

Fagen [50] has shown that for argon release from an amorphous alloy film, a temperature on the order of 400°C is required. The temperature of the substrate was estimated to be as high as 250°C. Thus, argon entrapment is quite feasible and is enhanced by the partially amorphous structure of the Ni-Ta films. A secondary factor that will contribute to the total weight percent not being 100 wt.% and which was not corrected for in the computer program is that the films are probably not 100% dense. Thus the argon content and/or less than 100% dense material account for the deviation from a total analyzed composition of 100 wt.%.

In summary, several major points are noted from the chemical analysis of the targets and the sputtered thin films. First, the change in composition from the target to the sputtered thin film is dependent on the sputtering

yields and the sticking coefficient of each specie. Specifically, as shown in the following table, for an alloy target, the sticking coefficients determine the change in composition and for a plasma-sprayed target, both the sticking coefficients and the sputtering yields determine the change in composition:

Target Material	Change in Composition From Target to Film	Explanation for Change or No Change
Ni-Aℓ alloy	No Change	$s_{Ni} \approx s_{Ta} \approx 1.0$
Ni-Aℓ alloy	Decrease in Ta	$1.0 \approx s_{Ni} > s_{A\ell} \approx 0.55$
Ni-Ta plasma-sprayed	Decrease in Ta	$2.4 \approx y_{Ni} > y_{Ta} \approx 0.98$
Ni-Aℓ plasma-sprayed	Decrease in Aℓ	$2.4 \approx y_{Ni} > y_{A\ell} \approx 1.0$ $1.0 \approx s_{Ni} > s_{A\ell} \approx 0.55$

Second, the temperature effects at the target or at the substrate do not influence the sputtering of the nickel or tantalum specie while both influence the sputtering of the aluminum specie. Third, the Ni-Ta films, which are partially amorphous, entrap argon while the Ni-Aℓ films, which are crystalline, do not show any detectable argon content.

Target Surface Phenomena

This section concerns the effect of ion bombardment on the target surface. As previously noted in the introduction, if the target is two phase, each phase will sputter according to its local composition. In this research, three basic target structures were used: two phase plasma-sprayed

targets (Table III), single phase plate targets (pure Ni, pure Aℓ and 93.1Ni - 6.9Aℓ alloy) and a two phase plate target structure (65.2Ni - 34.8Ta alloy). Each of these target structures gave a different ion bombardment effect.

Two sets of figures for the plasma-sprayed targets will be shown as typical of the surface structures before and after sputtering. Because a large dpeth of field is required to resolve these surfaces, an ETEC scanning electron microscope was employed. Figure 25(a) is the unsputtered surface of the Ni - 9.7Ta plasma-sprayed target and Figure 25(b) is the surface after about 8 hours of sputtering at a deposition rate of about 100 Å/min. Figure 26(a) is the unsputtered surface of the Ni - 6.8 Aℓ plasma-sprayed target and Figure 26(b) is the surface after about 15 hours of sputtering at a deposition rate of about 100 Å/min. The unsputtered surfaces of Figure 25(a) and 26(a) show the characteristic surface topography due to plasma spraying. Both surface are similar and indicate that composition does not significatly affect the topography. These two micrographs are typical of the unsputtered surface topography of all the plasma-sprayed targets. The sputtered surfaces of Figure 25(b) and 26(b) show two significant points. First, both surfaces possess a very pointed topography consisting of conical projections and seoond, there is a definite size difference of the conical projections of the two surfaces. The ion bombardment effect forming the

conical projection is due to the variation in sputtering yield with the angle of ion incidence as noted by Stewart and Thompson [51]. On increasing the ion incidence angle from 0° with respect to the surface normal, the sputtering yield increases, reaches a maximum and then decreases to zero at 90° (parallel to target surface). Although the angle of ion incidence is normal to the target surace, the irregular plasma-sprayed surface enhances the sputtering of surfaces at an angle to the ion flux. The conical projections are thus developed by the higher sputtering rates at these angled surfaces. The taller projections of Figure 26 (b) as compared to those of Figure 25 (b) results from the longer sputtering time of about 15 hours from the Ni-Aℓ target, compared to a sputtering time of about 8 hours from the Ni-Ta target. Thus the conical projections remain and increase in size as the sputtering time increases.

The single phase plate targets show very little effect due to ion bombardment in comparison to the two phase Ni-Ta alloy plate target. Prior to sputtering, the single phase targets were not given a metallographic polish due to their large size while the smaller two phase Ni-Ta alloy target was polished with 1 micron diamond paste with random areas having an excellent finish. The single phase targets showed only the outline of grain boundaries after sputtering for more than 8 hours from each target. Other ion etching effects were not noticed on the single phase targets.

due to the poor surface finish. In contrast, the two phase, chill-cast, Ni-Ta alloy target possessed several interesting ion bombardment phenomena.

As previously noted in the discussion concerning electron microprobe analysis, the microstructure of the Ni-Ta alloy target consists of a fine precipitate structure and second phase platelets or needles. This structure is shown polished and chemically etched (Marbles Etch) in Figures 27(a) and 27(b). Specifically, Figure 27(a) shows two converging platelets and the surrounding fine precipitate structure and Figure 27(b) shows the fine precipitate structure with very fine platelets and a path of lamellar structure. In addition, Figure 28 shows a high magnification micrograph of the fine precipitate matrix obtained by scanning electron microscopy. This reticulated and platelet structure agrees with the Ni-Ta phase diagram of Figure 2 with respect to the nominal composition (Table IV) and the sharp change in the solid solubility of tantalum in nickel.

After more than 8 hours of sputtering from the Ni-Ta alloy target, several ion etching effects are evident as shown in Figures 29 and 30. First, there is preferential sputtering from the matrix and the platelets; second, hillocks are formed randomly; and third, the fine precipitate structure is developed by sputtering. Replicating and shadowing techniques were performed on the target surface. Subsequent transmission electron microscopy revealed that

the platelets are raised and that some of the hillocks appear to be elevated and some depressed. The hillock formation is a phenomena due solely to ion bombardment as discussed by Bayly [52]. The development of the sputter-etched precipitate and platelet structures is due to the variation in the net sputtering rate with local atomic composition. The precipitate structure is not a chemically homogeneous structure on the fine precipitate size scale and thus the precipitates and the area in between them sputter at different rates. The platelets are high in tantalum ($\approx$ 42 wt.%) compared to the precipitate matrix ($\approx$ 34.8 wt.%) and are expected to sputter at a significantly different rate than the matrix. As previously discussed, the sputtering yield of tantalum is lower than that of nickel. Thus the high tantalum content platelets sputter at a slower rate than the matrix and form the elevated structure. This topography change results in a change in surface composition such that the composition of sputtered particles is equal to the average bulk composition.

In summary, this investigation of the surface topography before and after sputtering reveals the dependence of the sputtering rate on the angle of ion incidence and on the local atomic composition.

Microstructure

The data for the runs made for transmission electron microscopy are listed in Table XII. For each run, two nickel grids with carbon support films were used and, in addition, run #91 and #92 included two nickel grids with silicon monoxide support films. The deposition rate for all the runs was on the order of 100Å/min ±20Å/min. depending on the sputtering kilovoltages and argon pressure. Prior to deposition, care was taken to assure that the plasma was high purity argon with the characteristic light blue color. Each of the micrographs of this section will be accompanied by the run number, the target, the nominal film composition, the film thickness and the magnification. The results of the as-sputtered thin films are presented and discussed first; the hot stage transmission electron microscopy results are shown and discussed separately.

The pure aluminum and pure nickel thin films were deposited under similar conditions with the deposition time varied. The film thickness for the pure aluminum set were about 250Å, 500Å, and 750Å respectively and for the pure nickel set, they were 300Å, 600Å and 900Å respectively. The 250Å pure aluminum film possessed a discontinuous structure consisting of small "islands" of material on the carbon film. The 500Å pure aluminum film had a similar structure with a high density of "islands" and possibly with some structure between the "islands". Figure 31 is a bright

field micrograph of the 750Å thick pure aluminum film. This film is very irregular with large thick areas separated by thin areas. From dark field analysis, there are large single crystals on the order of 5000Å maximum which overlap other crystals. The "island" structure of the thin films and the very irregular structure of the 750Å thick film illustrate the high mobility of aluminum atoms on the substrate. The large crystallite size indicates that the impurity content of the argon plasma is very low. This is true because aluminum has a high affinity for oxygen or nitrogen and if oxides or nitrides did form, the structure would be very fine grained.

The pure nickel films possessed a significantly different structure than that of the pure aluminum films. Figure 32 is a bright field micrograph of the 300Å thick pure nickel film. The film had a continuous fine structure with a crystallite size on the order of 200Å to 300Å. Very few twins or stacking faults were noted. The selected area diffraction patterns from this film showed the diffraction rings to be continuous and this is indicative of the fine crystallite size. The pattern indexed as a standard face center cubic (F.C.C.) pattern with a lattice parameter of 3.5225Å. This lattice parameter value is exceptionally close to the published x-ray data for pure nickel of 3.5238Å [53].

All of the pure nickel films were continuous and the

average crystallite size increased as the film thickness increased. The 300Å thick film possessed an average crystallite size of 200Å to 300Å with the largest crystallites about 700Å; the 600Å thick film had an average crystallite size of about 500Å with the largest being approximately 1300Å; and the 900Å film had a crystallite size of approximately 700Å with several very large crystallites. The density of twins and/or stacking faults appeared to increase with the thicker films. The selected area diffraction pattern for each thickness showed sharp rings with an increase in the "spottiness" corresponding approximately to the increase in the average crystallite size.

The thin Ni-Aℓ alloy films deposited from the 93.2Ni - 6.8Aℓ plasma-sprayed target possessed a structure similar to that of the pure nickel but with several important differences. The deposition conditions were similar to those for the pure aluminum and pure nickel runs and the resultant thicknesses of the film were again about 300Å, 600Å, 900Å and 1200Å respectively. The structures of the 300Å and the 600Å films are shown in Figure 33(a) and 33(b) respectively. The 900Å and 1200Å films showed a structure similar to the two thinner films but the transmission was seriously hampered because of the low intensity due to the high film thickness. Comparison of Figure 33(a) with 32 shows the crystallite size to be finer for the Ni-Aℓ alloy than for the pure nickel. The average crystallite size for

the 300Å alloy thin film was estimated to be between 50Å and 100Å. Although slight changes in grain size can be noted as a function of deposition time or film thickness (Figure 33), all of the alloy films had a crystallite size less than 100Å. The selected area diffraction patterns were consistent with the observed fine structure in having very continuous, slightly broadened rings. The patterns from each of the films indexed to a standard F.C.C. structure but with lattice parameters that varied significantly from that for pure nickel, i.e. a lattice parameter of 3.41Å was found for the 300Å film and a value of 3.64Å was found for the 600Å films. The thinnest (300Å) film also gave some very weak extra rings not corresponding to an F.C.C. structure which were not present for the thicker films.

There were also significant differences between the structure of the alloy films deposited from the plasma-sprayed targets and those from the alloy targets (Table XII). The film thicknesses obtained from the alloy targets were approximately 600Å for the Ni-Aℓ alloy film and approximately 500Å for the Ni-Ta alloy films.

The structure and selected area diffraction pattern for the Ni-Aℓ film sputtered from the 93.1Ni - 6.9Aℓ alloy target are shown in the micrographs of Figures 34(a) and 34(b). The structure (Figure 34(a)) consisted of very fine crystallites less than 100Å in size with good

diffraction contrast as was the case for the Ni-Aℓ alloy films obtained from the plasma-sprayed target. However, the diffraction pattern of Figure 36(b) showed very continuous and somewhat broadened rings which indexed to a set of very strong and a set of weak F.C.C. patterns. It was noted that the weak extra rings observed for the 300Å alloy film from the Ni-Aℓ plasma-sprayed target correspond somewhat to the weak F.C.C. pattern of Figure 34(b).

The structure and selected area diffraction pattern for the Ni-Ta alloy film obtained from the alloy target are given in Figures 35(a) and 35(b). In contrast to the Ni-Aℓ alloy films, this structure exhibited very little diffraction contrast and the diffraction pattern gave only two diffuse rings. Tilting of the specimen showed that the Ni-Ta alloy film possessed a definite texture as shown in the selected area diffraction patterns of Figure 36. The four fold symmetry of the inner most ring, as shown in Figure 36(a), occurred at a specimen tilt of either about +19° or about -36°. The two-fold symmetry of the inner most ring (Figure 36(b)) was obtained at a specimen tilt of about -6.5°. Tilting of the sample also produced some short arcs of diffraction rings which did not correspond to the complete rings of Figure 35(b).

The crystallite size in a thin film depends atomistically on the density and mobility of atoms on the substrate. This may be translated into the rate of arrival

of atoms to the substrate, the sticking coefficient and the resputtering and evaporation rates for the film. If the resputtering and evaporation rates are assumed negligible, the rate of arrival depends on the sputtering parameters while the sticking coefficient depends on the relative substrate temperature, T_s/T_{mp}, and the substrate material. For all of the runs described above, the sputtering parameters were maintained fairly constant and the substrate was a carbon support film. Thus the major difference for each material is the substrate temperature, T_s, with respect to the melting point of the material, T_{mp}. A substrate temperature of about 100°C maximum can be assumed because all of the film deposition runs for electron microscope examination were made at extremely short times. The ratio $[T_s/T_{mp}]_{A\ell}$ is much larger than the ratio $[T_s/T_{mp}]_{Ni}$. Thus the crystallite size for nickel is much less than that for aluminum as is observed for the pure element films. The melting point of the alloy in the Ni-Aℓ films is only slightly lower than that of pure nickel and it is expected from the temperature factor that the alloy films should have a crystallite size approximately equal to that for pure nickel. This is opposite to what is observed and therefore other factors must be considered when analyzing crystallite size in alloy films. The aluminum specie in the Ni-Aℓ alloy films is essentially an impurity with respect to the nickel lattice. The accommodation of the

larger aluminum atoms results in a "defect" structure and a finer crystallite size for the Ni-Aℓ alloy in comparison to pure nickel.

The crystallite size as a function of the film thickness depends on the previously mentioned factors of the net deposition rate and the substrate temperature. However, these factors will change as the sputtering process continues. First, the mobility of the atoms will change as the substrate becomes the initial thin film deposit and second, the substrate temperature will change. Both of these factors will tend to increase crystallite size as follows. As the substrate becomes the thin film deposit, the crystallite nucleation rate will decrease and crystallites will tend to grow rather than to start new ones [20]. Due to the high energy of the arriving atoms, heat will build up in the thin film and the corresponding increase in temperature enhances the formation of larger crystallites. As was observed in the micrographs for both the pure nickel and the Ni-Aℓ films and by the increase in the spottiness of the diffraction rings, the crystallite size did increase as the film thickness increased.

The defect structure of the films depends primarily on the mobility of the atoms. Thus, for the pure aluminum films with the relatively high atom mobility, there were few defects, i.e. the major feature in these films are interference fringes due to thickness contours. For the

nickel base films with relatively low atom mobility, there are several defects, twins and/or stacking fault, and a high surface area to volume ratio because of the small crystallite size. For pure nickel, the stacking fault energy is high [2] and twins and stacking faults are not expected and were very rarely observed. The deposition of vapor on a cold substrate, however, will enhance the formation of these defects and is the explanation for the observed defects. The addition of a solute to the material will also aid in the formation of defects. This is an effect similar to that which produced the finer crystallite size of the alloy films. In solid solution with nickel, both aluminum and tantalum lower the stacking fault energy of nickel [2] and increase the probability of twins and stacking faults. As noted previously, the atomic diameter of aluminum is 6% larger and tantalum is 18% larger than nickel. Thus, both the Ni-Aℓ and Ni-Ta alloy films should yield a higher defect density in the structure.

The observed structure of the alloy films agrees with the criteria set forth by Mader [22] (as noted in the introduction) in that the Ni-Aℓ alloy films were crystalline and the Ni-Ta alloy films were "semi-amorphous". Although the Ni-Aℓ alloy films were crystalline, the very fine structure and resultant high grain boundary to volume ratio indicate that the defects are predominantly incorporated into the grain boundaries. A discussion of geometric defects for

the Ni-Ta alloy films is not appropriate because of the "semi-amorphous" structures. The structure showed little diffraction contrast but is called "semi-amorphous" because the selected area diffraction patterns indicated a texture which could arise only from crystalline material.

The last point relevant to the as-sputtered structures concerns the phases that are present. The diffraction patterns for the pure Ni and the Ni-Aℓ alloy films have been analyzed but no clear interpretation is presently available for indexing of the diffuse rings observed in the Ni-Ta alloy film.

The pure Ni films gave excellent lattice parameter values which corresponded to the published x-ray data. Although the substrate used for the electron microprobe analysis of the Ni-Aℓ alloy films was not the same as that for the transmission electron microscopy, the composition of the thin films are assumed to be that determined by the electron microprobe. Thus, the composition of the films from the 93.2Ni - 6.8Aℓ plasma-sprayed target is 1.46 wt.% Aℓ and the composition of the films from the Ni-Aℓ alloy target is 3.95 wt.% Aℓ. With the exception of the very thin 300Å film, the diffraction pattern for the Ni-1.46 wt.% Aℓ films indexed to a single F.C.C. phase with a lattice parameter significantly different than that of pure nickel. This confirms that the film is a single phase, solid solution of aluminum in nickel. As shown in Figure

34(b), the Ni-3.95 wt.% Aℓ films from the Ni-Aℓ alloy target contained two F.C.C. phases. The diffraction patterns for these phases indexed to γ and γ' with the γ' lines corresponding to the weak rings. The weak rings for the 300Å Ni-1.46 wt.% Aℓ film can thus be assumed to be due to γ'. Under equilibrium conditions, neither of these alloys should possess the γ' phase but these films were formed under severely non-equilibrium conditions. The two phase, γ and γ' structure of the non-equilibrium as-sputtered films may be explained as follows. The aluminum specie has high mobility on the substrate surface and the crystallites are very fine. With these two facts, the aluminum specie may tend to segregate at the crystallite grain boundaries which would require only short distances of travel. The grain boundaries would thus be high in aluminum content and may therefore order to form $Ni_3A\ell$. This reaction is reasonable because the sputtered film is a high energy, non-equilibrium structure where equilibrium thermodynamics of bulk phases does not apply. The volume fraction of the $Ni_3A\ell$ would be small and would correspond to the diffraction rings being weak. For Ni-1.46 wt.% Aℓ alloy, the γ' rings are noticed only for the very short deposition time where the heating effects are minimal. The Ni-3.95 wt.% Aℓ alloy gave the γ' rings for the thicker 600A film due to the higher aluminum content. As will be shown, the set of weak diffraction rings disappear on heating. These weak γ' rings were also

studied to see if they were due to double diffraction rather than γ'. The double diffraction principle has been well discussed by Pashley and Stowell [54] and the observed rings do not correspond to double diffraction. This point is significant because although none of the Ni-Aℓ alloy films showed any preferred orientation by transmission electron microscopy, preliminary results by the more accurate technique of x-ray diffraction on the Ni-3.95 wt.% Aℓ films of Table V indicate a definite (111) texture.

The hot stage transmission electron microscopy was performed on both the R.C.A. EMU-3G model and the Phillips 300 model. The R.C.A. EMU-3G (with a lower maximum hot stage temperature) was used for the initial analysis of the thin films from the 93.2Ni - 6.8Aℓ plasma-sprayed target. As noted previously, only the 300Å film exhibited extra diffraction rings corresponding to a two-phase structure. Each of the films (i.e. 300Å, 600Å, 900Å and 1200Å) was heated to approximately 600°C and the change in structure was observed. The 300Å and 600Å films agglomerated on heating while the thicker 900Å and 1200Å films recrystallized without breakup of the film. Figure 37 shows the transformed structure of the 600A thick Ni-1.46 wt.% Aℓ film after heating to 575°C. This low magnification, bright field micrograph shows two different structures: a very fine structure with crystallites of the same size as the as-sputtered structure and relatively large globular

particles of an average size of 1.2 μ with associated areas denuded of material. The high magnification micrograph of Figure 38 illustrates that the globular particles possessed significant internal structure. A most dramatic consequence of the film breakup and agglomeration is shown by the unusual pattern in Figure 39.

The agglomeration phenomena of the thinner films is caused by a relaxation of the film into a lower energy configuration. Presland et al. [55,56] have observed and analyzed this phenomena for thin silver films. In the present work, the 300Å film structure was observed to break up at a slightly lower temperature than that for the 600Å film. Depending on the film thickness, there is a critical temperature, as was experimentally found. On break up, the fine structure either was consumed into the larger particles or recovered with a slight growth in crystallite size. The globular particles did not increase in size significantly on holding at about 600°C and thus single crystal diffraction techniques could not be employed. The thicker 900Å and 1200Å films did not agglomerate presumably because either not enough thermal energy was available or more probably, the continuous film is the stable configuration.

The films from the alloy targets, runs #91 and #92, were studied on the hot stage of the Phillips 300 microscope. Particular attention was paid to the selected area diffraction patterns on monitoring the change in structure

while heating the film. The break-up of the film was noticed only randomly for the Ni-3.95 wt.% Aℓ films and the Ni-36.7 wt.% Ta films even though the temperature was raised to 900°C for a short time. Nevertheless, the film surface did become irregular which indicates some relaxation and movement of material. Both the films deposited on carbon and those on silicon monoxide exhibited similar changes in structure on heating.

In the as-sputtered condition, the Ni-3.95 wt.% Aℓ films possessed a two phase, $\gamma + \gamma'$ structure. Figures 40 and 41 are the selected area diffraction patterns at temperatures of 265°C and 415°C respectively. The comparison of these two patterns with the room temperature pattern shown in Figure 34(b) revealed several interesting points. In Figure 40, the two weak inner most rings are the (100) and (110) reflections of the ordered γ'-$Ni_3A\ell$ phase. The high intensity "double-ring" indexed to two very closely spaced rings corresponding to the (111) reflections of γ and γ'. In contrast, the diffraction pattern at 415°C (Figure 41) showed no γ' rings and indexed to a standard single phase F.C.C. structure. Bright field analysis showed only an increase in diffraction contrast with little change in the fine structure. Upon heating to approximately 700°C, the fine structure recrystallized into polygonal grains as shown in Figure 42(a) and 42(b) and the selected area diffraction pattern showed sharp spotty rings. The

bright field micrograph (Figure 42(a)) shows a very irregular surface while the dark field micrograph (Figure 42(b)) clearly illustrates the polygonal crystallites. This polygonal structure is similar to the structure of the 900Å and 1200Å Ni-1.46 wt.% Aℓ films that were heated to 600°C. At approximately 900°C, the Ni-3.95 wt.% Aℓ films exhibited a very irregular structure with many thickness contour fringes. The diffraction pattern at 900°C gave a very spotty F.C.C. pattern with some extra weak, continuous rings. Although the pattern was not indexed, the extra weak rings appear to be due to double diffraction and not to a second phase. The double diffraction phenomena [54] may arise because of the very irregular surface and the fine crystallite size.

The appearance of the γ' $Ni_3A\ell$ rings in the diffraction patterns up to about 400°C is consistent with the explanation that the grain boundaries are enriched in aluminum and order to form $Ni_3A\ell$. The disappearance of the rings in the diffraction pattern at 415°C indicates that the γ' phase has been eliminated. This would correspond to the hypothesis that if the structure at the grain boundaries was aluminum rich and ordered to form $Ni_3A\ell$, then by heating the film, the defects (grain boundaries) should relax and permit aluminum to distribute homogeneously. This disappearance of $Ni_3A\ell$ at about 400°C is in contrast to the disordering temperature of 1250°C for $Ni_3A\ell$ in the bulk

alloys [57].

Heating of the "semi-amorphous" Ni-36.7 wt.% Ta film resulted in only minor changes in the film structure but major changes were noted in the diffraction effects. On increasing the temperature to about 400°C, the structure showed an increase in diffraction contrast but the diffraction patterns did not change. At approximately 400°C, the diffraction pattern changed and showed many continuous rings as shown in Figure 43. The structure corresponding to this pattern exhibited a very fine crystallite size (<< 100Å). Continued heating to 900°C resulted in enhanced diffraction contrast, a slight increase in crystallite size and sharper diffraction rings. The final structure and associated selected area diffraction pattern at 900°C are shown in the micrographs of Figures 44(a) and 44(b) respectively. Tilting of the specimen showed that the texture, observed in the as-sputtered structure, was present at all temperatures.

The composition of the Ni-36.7 wt.% Ta film is such that the structure is two phase under equilibrium conditions (Figure 2). The diffraction patterns were therefore not indexed due to the many rings and the uncertain structure of the Ni_3Ta phase. Thus the exact phases present in the heat treated films are not known. Also, no definitive x-ray data for intermediate phases in the Ni-Ta system is available. These facts, and the unusual combination of both a texture effect and the presence of diffuse rings in the as-

sputtered films have prevented good phase analysis for these films. However, the texture that is present in the heat-treated films is confined to only a few rings and thus there are at least two phases present; an oriented phase and a randomly oriented phase. The very slight change in crystallite size shows that the structure is quite stable and does not tend to break up upon heating.

Mader [22] has presented the rough criteria that an amorphous alloy film should become crystalline on heating to between 0.3 $*T_{mp}$ and 0.35 $* T_{mp}$ where T_{mp} is the average melting points of the component species. The average melting point for this Ni-36.7 wt.% Ta alloy, based on the atomic fractions of nickel and tantalum, is approximately 1970°K and according to Mader, the film should become crystalline between 320° and 420°C. Thus the observed change in diffraction pattern at about 400°C agrees fairly well with Mader's criteria.

In summary, the transmission electron microscopy has revealed several significant points. First, in the as-deposited condition, the Ni-Ta thin film possessed a "semi-amorphous" structure while the Ni-Aℓ thin films had a very fine but crystalline structure. Second, the average crystallite size for the as-sputtered films increased as the film thickness increased. Third, the Ni-1.46 wt.% Aℓ films were primarily single phase while the Ni-3.95 wt.% Aℓ were two phase in the as-deposited condition. The hot stage

work showed three major effects. First, very thin continuous films tended to agglomerate on heating. Second, the γ'-Ni_3Al phase that was observed in some of the Ni-Al alloy films disappeared on heating. Finally, the "semi-amorphous" Ni-Ta alloy film transformed into a two phase fine crystalline structure at approximately 400°C.

CONCLUSIONS

This investigation of the R.F. sputtering of nickel alloys has produced the following results:

(1) The deposition rate of a nickel alloy on glass changes significantly for a constant sputtering rate for an initial short period of time due to a change in the sticking coefficients.

(2) The major control of the deposition rate for R.F. sputtering is obtained by the regulation of the applied voltages and the argon pressure. For constant pressure conditions, the sputtering rate is linearly related to the voltage for ion accelerating potentials between 0.5 kev and 5 kev. For constant volt- conditions, the sputtering rate is linearly related to the argon pressure up to approximately $20 * 10^{-3}$ torr.

(3) The control of film composition is dependent on the target construction and composition and on the sputtering yields and sticking coefficients. All of the films gave equal or greater nickel contents than that in the targets due to the higher sputtering yield

of nickel to those of the solute specie aluminum or tantalum.

(4) The net sputtering rate is particularly a function of the angle of ion incidence and of the local atomic configuration.

(5) The as-deposited structure of the R.F. sputtered films is related to the mobility of the sputtered species on the substrate and to the degree of mismatch of the specie atoms for an alloy film. As-depositied, the Ni-Al films possessed a fine crystalline structure and the high tantalum (36.7 wt.% Ta) sputtered film had a somewhat amorphous structure.

(6) The sputtered films may maintain a high energy non-equilibrium structure where bulk thermodynamic considerations are strongly influenced by surface affects.

(7) The absorption of argon is particularly noticed for the sputtered films that tend to form a non-crystalline structure.

TABLE I

Physical Properties of $A\ell$, Ni and Ta

	$A\ell$	Ni	Ta
Atomic number	13	28	73
Atomic weight	26.9815	58.71	180.948
Melting Point	660°C	1453°C	2996°C
Crystal Structure	F.C.C.	F.C.C.	B.C.C.

TABLE II

Composition of Powder Mixtures for
Plasma-Sprayed Targets

Ni - $A\ell$ System

98.8 wt % Ni - 1.2 wt % $A\ell$

96.6 wt % Ni - 3.4 wt % $A\ell$

95.4 wt % Ni - 4.6 wt % $A\ell$

93.2 wt % Ni - 6.8 wt % $A\ell$

Ni - Ta System

97.6 wt % Ni - 2.4 wt % Ta

90.3 wt % Ni - 9.7 wt % Ta

82.9 wt % Ni - 17.1 wt % Ta

TABLE III

Chemical and Sieve Analysis of Elemental Powders

Ni powder (wt.%)		Ta powder (wt.%)		Aℓ powder (wt.%)	
Ni	99.83	Ta	99.59	Aℓ	99.50
Co	0.07	Cb	0.20	Fe	0.17
Fe	0.030	C	0.11		
S	0.020	O	0.07		
C	0.007	Si	0.02		
Cu	0.005	Fe	0.01		
		Ti	0.01		
(Tyler)		(Tyler)		(Tyler)	
+200	10% max.	+200	10% max.	+270	5% max.
-325	15% max.	-325	25% max.	-270	balance

TABLE IV

Composition of Machined Plate Targets

Pure Ni (wt.%)		Pure Aℓ (wt.%)		93.1Ni-6.9Aℓ (wt.%)		65.2Ni-34.8Ta (wt.%)	
Ni	99.95	Aℓ	99.995	Ni	92.99	Ni	64.85
Fe	0.01/0.04	Si	0.001	Aℓ	6.9	Ta	34.8
Co	0.01/0.03	Fe	0.001	Ti	0.088	Ti	0.28
C	trace	Cu	0.001	Mg	0.013	Aℓ	0.042
Si	trace			C	0.008	C	0.012
S	trace					O	0.0105
						N	0.0020
						Mg	0.0003

TABLE V

Runs with Time Varied
for 93.1Ni-6.9Aℓ Alloy Target

Run (#)	Time (MIN.)	F.P. (WATTS)	R.P. (WATTS)	R.F. (kv)	D.C. (kv)	P_{Ar} (μ)
71	5	265	0	2.57	2.01	2.9
69	10	265	0	2.52	2.01	2.9
77	15	255	0	2.44	2.01	2.9
78	20	255	0	2.51	2.01	2.9
79	25	250	0	2.56	2.01	2.9
80	30	255	0	2.59	2.01	2.9
70	60	260	0	2.49	2.01	2.9
68	120	255	0	2.47	2.01	2.9

TABLE VI

Runs with D.C. Bias Varied
for 93.1Ni-6.9Aℓ Alloy Target

Run (#)	Time (MIN.)	F.P. (WATTS)	R.P. (WATTS)	R.F. (kv)	D.C. (kv)	P_{Ar} (μ)
81	10	400	0	3.41	2.50	2.9
69	10	265	0	2.52	2.01	2.9
82	10	170	19	1.79	1.50	2.9
83	10	92	19	1.09	1.00	2.9
85	30	186	10	1.10	1.00	2.9
86	30	41	8	0.56	0.50	2.9
84	20	59	30	0.45	0.45	2.9

TABLE VII

Runs with Argon Pressure Varied for 93.1Ni-6.9Aℓ Alloy Target

Run (#)	Time (MIN.)	F.P. (WATTS)	R.P. (WATTS)	R.F. (kv)	D.C. (kv)	P_{Ar} (μ)
69	10	265(255)	0	2.52	2.01	2.9
87	10	275	0	2.58	2.01	5.1
88	10	325	0	2.61	2.01	10.0
89	10	450	0	2.65	2.01	20.2
90	10	515	0	2.72	2.01	34.0

TABLE VIII

Runs with Ni-Aℓ Targets
at Constant Sputtering Parameters
for Deposition Rate Analysis

Target (wt.%)	Run (#)	Time (min.)	F.P. (watts)	R.F. (watts)	R.F. (kv)	D.C. (kv)	P_{AR} (μ)
Pure Ni	36	5	280	0	2.36	2.01	2.7
Pure Ni	34	10	275	0	2.36	2.01	2.8
98.8Ni-1.2Aℓ plasma sprayed	32	5	265	0	2.70	2.01	2.7
98.8Ni-1.2Aℓ plasma sprayed	30	10	250	0	2.53	2.03	2.7
96.6Ni-3.4Aℓ plasma sprayed	42	5	280	0	2.49	2.01	2.7
96.6Ni-3.4Aℓ plasma sprayed	40	10	280	0	2.46	2.01	2.9
95.4Ni-4.6Aℓ plasma sprayed	46	5	255	0	2.30	2.01	2.8
95.4Ni-4.6Aℓ plasma sprayed	44	10	265	0	2.35	2.01	2.8
93.2Ni-6.8Aℓ plasma sprayed	52	5	255	0	2.43	2.01	2.8
93.2Ni-6.8Aℓ plasma sprayed	50	10	250	0	2.51	2.01	2.9
93.1Ni-6.9Aℓ alloy	71	5	265	0	2.57	2.01	2.9
93.1Ni-6.9Aℓ alloy	69	10	265	0	2.52	2.01	2.9

TABLE IX

Runs with Ni-Ta Targets
at Constant Sputtering Parameters
for Deposition Rate Analysis

Target (wt.%)	Run (#)	Time (min.)	F.P. (watts)	R.P. (watts)	R.F. (kv)	D.C. (kv)	P_{Ar} (μ)
Pure Ni	36	5	280	0	2.36	2.01	2.7
Pure Ni	34	10	275	0	2.36	2.01	2.8
97.6Ni-2.4Ta plasma sprayed	56	5	260	0	2.35	2.01	2.9
97.6Ni-2.4Ta plasma sprayed	54	10	255	0	2.38	2.01	2.9
90.3Ni-9.7Ta plasma sprayed	62	5	245	0	2.44	2.01	2.9
90.3Ni-9.7Ta plasma sprayed	60	10	240	0	2.43	2.01	2.9
82.9Ni-17.1Ta plasma sprayed	66	5	255	0	2.31	2.01	2.9
82.9Ni-17.1Ta plasma sprayed	64	10	260	0	2.30	2.01	2.9
65.2Ni-34.8Ta alloy	76	5	265	0	2.36	2.01	2.9
65.2Ni-34.8Ta alloy	74	10	260	0	2.35	2.01	2.9

TABLE X

Runs with Ni-Aℓ Targets at Constant Sputtering Parameters for Microprobe Analysis

Target (wt.%)	Run (#)	Time (min.)	R.F. (kv)	D.C. (kv)	P_{Ar} (μ)
Pure Ni	35	60	2.33	2.01	2.8
Pure Ni	33	120	2.35	2.01	2.8
98.8Ni-1.2Aℓ plasma sprayed	31	60	2.55	2.01	2.7
98.8Ni-1.2Aℓ plasma sprayed	29	120	2.56	2.01	3.0
96.6Ni-3.4Aℓ plasma sprayed	41	60	2.43	2.01	3.0
96.6Ni-3.4Aℓ plasma sprayed	39	120	2.54	2.01	2.8
95.4Ni-4.6Aℓ plasma sprayed	45	60	2.32	2.01	2.7
95.4Ni-4.6Aℓ plasma sprayed	43	120	2.34	2.01	2.8
93.2Ni-6.8Aℓ plasma sprayed	51	60	2.46	2.01	2.8
93.2Ni-6.8Aℓ plasma sprayed	49	120	2.41	2.01	2.9
93.1Ni-6.9Aℓ alloy	70	60	2.49	2.01	2.9
93.1Ni-6.9Aℓ alloy	68	120	2.47	2.01	2.9

TABLE XI

Runs with Ni-Ta Targets
at Constant Sputtering Parameters
for Microprobe Analysis

Target (wt.%)	Run (#)	Time (min.)	R.F. (kv)	D.C. (kv)	p_{Ar} (μ)
Pure Ni	35	60	2.33	2.01	2.8
Pure Ni	33	120	2.35	2.01	2.8
97.6Ni-2.4Ta plasma sprayed	55	60	2.34	2.01	2.8
97.6Ni-2.4Ta plasma sprayed	53	120	2.37	2.01	2.8
90.3Ni-9.7Ta plasma sprayed	61	60	2.43	2.01	2.8
90.3Ni-9.7Ta plasma sprayed	59	120	2.41	2.01	2.8
82.9Ni-17.1Ta plasma sprayed	65	60	2.31	2.01	2.8
82.9Ni-17.1Ta plasma sprayed	63	120	2.30	2.01	2.8
65.2Ni-34.8Ta alloy	75	60	2.36	2.01	2.8
65.2Ni-34.8Ta alloy	73	120	2.35	2.01	2.8

TABLE XII

Runs with Various Targets for Transmission Electron Microscopy

Target (wt.%)	Run (#)	Time (Min.)	F.P. (Watts)	R.P. (Watts)	R.F. (kv)	D.C. (kv)	P_{Ar} (μ)
Pure Aℓ	15	3	245	1	2.03	1.79	2.9
Pure Aℓ	16	6	245	1	1.99	1.73	3.0
Pure Aℓ	17	9	240	0	1.99	1.71	3.0
Pure Ni	18	3	235	9	2.13	1.83	3.1
Pure Ni	21	6	250	4	2.23	1.84	3.1
Pure Ni	23	9	245	2	2.18	1.81	2.9
93.2Ni-6.8Aℓ plasma sprayed	22	3	245	2	2.16	1.81	3.0
93.2Ni-6.8Aℓ plasma sprayed	24	6	245	2	2.19	1.79	3.0
93.2Ni-6.8Aℓ plasma sprayed	25	9	240	3	2.16	1.79	2.9
93.2Ni-6.8Aℓ plasma sprayed	26	12	240	7	2.27	1.88	2.8
93.1Ni-6.9Aℓ alloy	91	5	275	0	2.61	2.01	2.9
65.2Ni-34.8Ta alloy	92	5	280	0	2.41	2.01	2.9

TABLE XIII

Sputtering Yield for Ni, Aℓ and Ta by Ar^+ ions

Ar^+ energy	Ni (atoms/ion)	Aℓ (atoms/ion)	Ta (atoms/ion)
200 ev	0.7[39]	0.35[39]	0.3[39]
500 ev	1.45[36], 1.33[37]	1.05[36]	0.57[36]
600 ev	1.52[39]	1.24[39]	0.6[39]
1000 ev	2.21[37], 2.1[41], 2.0[38]	—	—
5000 ev	—	2.0[40]	1.05[40]

TABLE XIV

Threshold Energy for Ni, Aℓ and Ta

	Ar^+ (ev)
Ni	21
Aℓ	13
Ta	26

TABLE XV

Sputtering Yields and Target Surface Composition for Ni-Aℓ Alloy Target for Various Target Voltage Conditions

(kv)	Y_{Ni} ($\frac{atoms}{ion}$)	$Y_{A\ell}$ ($\frac{atoms}{ion}$)	X_{Ni} (atomic)	$X_{A\ell}$ (atomic)	$X_{Ni}Y_{Ni}+X_{A\ell}Y_{A\ell}$ ($\frac{atoms}{ion}$)
3.41	2.48	1.95	0.8298	0.1702	2.3898
2.52	2.42	1.90	0.8296	0.1704	2.3314
1.79	2.34	1.82	0.8282	0.1718	2.2507
1.10	2.15	1.63	0.8246	0.1754	2.0588
0.56	1.56	1.17	0.8230	0.1770	1.4910

TABLE XVI

Calculated Deposition Rate Ratio and Deposition Rates

	$\dot{D}_{1.10RF}\|_{t=0^+} = 27.5$		$\dot{D}_{2.52RF}\|_{t=0^+} = 66.0$		
V_{RF} (kv)	$\frac{\dot{D}_1\|_{t=0^+}}{\dot{D}_{1.10}\|_{t=0^+}}$ (——)	$\dot{D}_1\|_{t=0^+}$ (Å/Min.)	$\frac{\dot{D}_1\|_{t=0^+}}{\dot{D}_{2.52}\|_{t=0^+}}$ (——)	$\dot{D}_1\|_{t=0^+}$ (Å/Min.)	$\overline{\dot{D}_1}\|_{t=0^+}$ (Å/Min.)
3.41	3.598	99.0	1.387	91.5	95.2
2.52	2.594	71.3	1.000	66.0	68.6
1.79	1.779	48.9	0.686	45.3	47.1
1.10	1.000	27.5	0.385	25.4	26.5
0.56	0.369	10.1	0.142	9.4	9.8

TABLE XVII

Wet Chemical Analysis of Plasma-Sprayed Targets

Powder (wt.%)	Plasma-Sprayed Film (wt.% Ni - balance Aℓ or Ta)
98.8Ni - 1.2Aℓ	98.75Ni - 1.25Aℓ 98.93Ni - 1.07Aℓ
96.6Ni - 3.4Aℓ	95.74Ni - 4.26Aℓ 96.12Ni - 3.88Aℓ
95.4Ni - 4.6Aℓ	95.35Ni - 4.65Aℓ 95.14Ni - 4.86Aℓ
93.2Ni - 6.8Aℓ	93.19Ni - 6.81Aℓ 93.33Ni - 6.67Aℓ
97.6Ni - 2.4Ta	94.16Ni - 5.84Ta 94.19Ni - 5.81Ta
90.3Ni - 9.7Ta	86.96Ni - 13.04Ta 87.25Ni - 12.75Ta
82.9Ni - 17.1Ta	89.06Ni - 10.94Ta 88.84Ni - 11.16Ta

TABLE XVIII

Electron Microprobe Analysis of
Ni - $A\ell$ Sputtered Films

Deposition Time Probe kv - Sample Current X-ray Lines	1-Hour 8kv-0.10μA. $Ni_{L\alpha}$, $A\ell_{K\alpha}$	2-Hour 8kv-0.10μA. $Ni_{L\alpha}$, $A\ell_{K\alpha}$	2-Hour 20kv-0.05μA. $Ni_{K\alpha}$, $A\ell_{K\alpha}$	
Target Material	(wt.% $A\ell$)	(wt.% $A\ell$)	(wt.% $A\ell$)	(wt.% $A\ell$)
Pure Ni	0.004	0.000	0.038	0.014
98.8Ni - 1.2$A\ell$ Plasma Sprayed	0.532	0.517	0.506	0.518
96.6Ni - 3.4$A\ell$ Plasma Sprayed	0.833	0.884	0.860	0.859
95.4Ni - 4.6$A\ell$ Plasma Sprayed	1.121	1.169	1.112	1.134
93.2Ni - 6.8$A\ell$ Plasma Sprayed	1.676	1.368	1.322	1.455
93.1Ni - 6.9$A\ell$ Alloy	3.737	4.083	4.021	3.947

TABLE XIX

Electron Microprobe Analysis
of Ni-Ta Sputtered Films

Deposition Time	2-Hour
Probe kv - Sample Current	20 kv - 0.05μA.
X-ray Lines	$Ni_{K\alpha}$, $Ta_{L\alpha}$

Target Material	Standards: Pure Ni, Pure Ta			65.2Ni - 34.8Ta Alloy		
	wt.% Ni	wt.% Ta	sum	wt.% Ni	wt.% Ta	sum
Pure Ni	101.838	0.067	101.905	101.215	0.065	101.280
97.6Ni - 2.4Ta Plasma Sprayed	98.161	1.164	99.325	98.045	1.149	99.194
90.3Ni - 9.7Ta Plasma Sprayed	92.330	6.504	98.834	92.072	6.364	98.436
82.9Ni - 17.1Ta Plasma Sprayed	90.580	6.830	97.411	91.115	6.906	98.022
65.2Ni - 34.8Ta Alloy	53.939	37.015	90.954	54.769	36.394	91.163

TABLE XX

Calculated Target Composition for Ni-Ta Plasma-Sprayed Targets

Film Composition (wt.% Ta)	"Expected" Target Composition (wt.% Ta)	Powder Composition (wt.% Ta)
1.16	2.8	2.4
6.43	14.5	9.7
6.87	15.3	17.1

FIGURE 1

THE NI-AL PHASE DIAGRAM

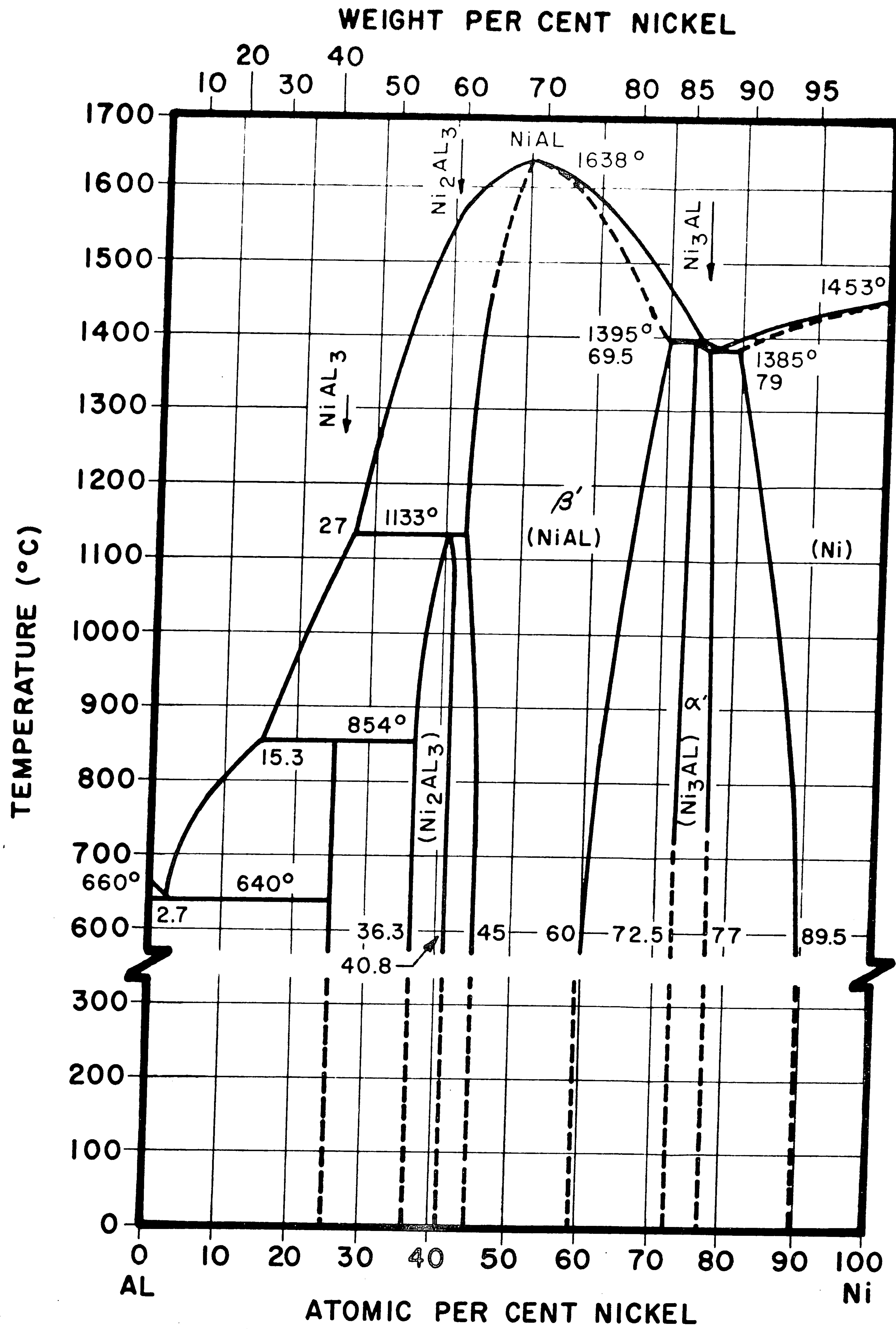

FIGURE 2

THE NI-TA PHASE DIAGRAM

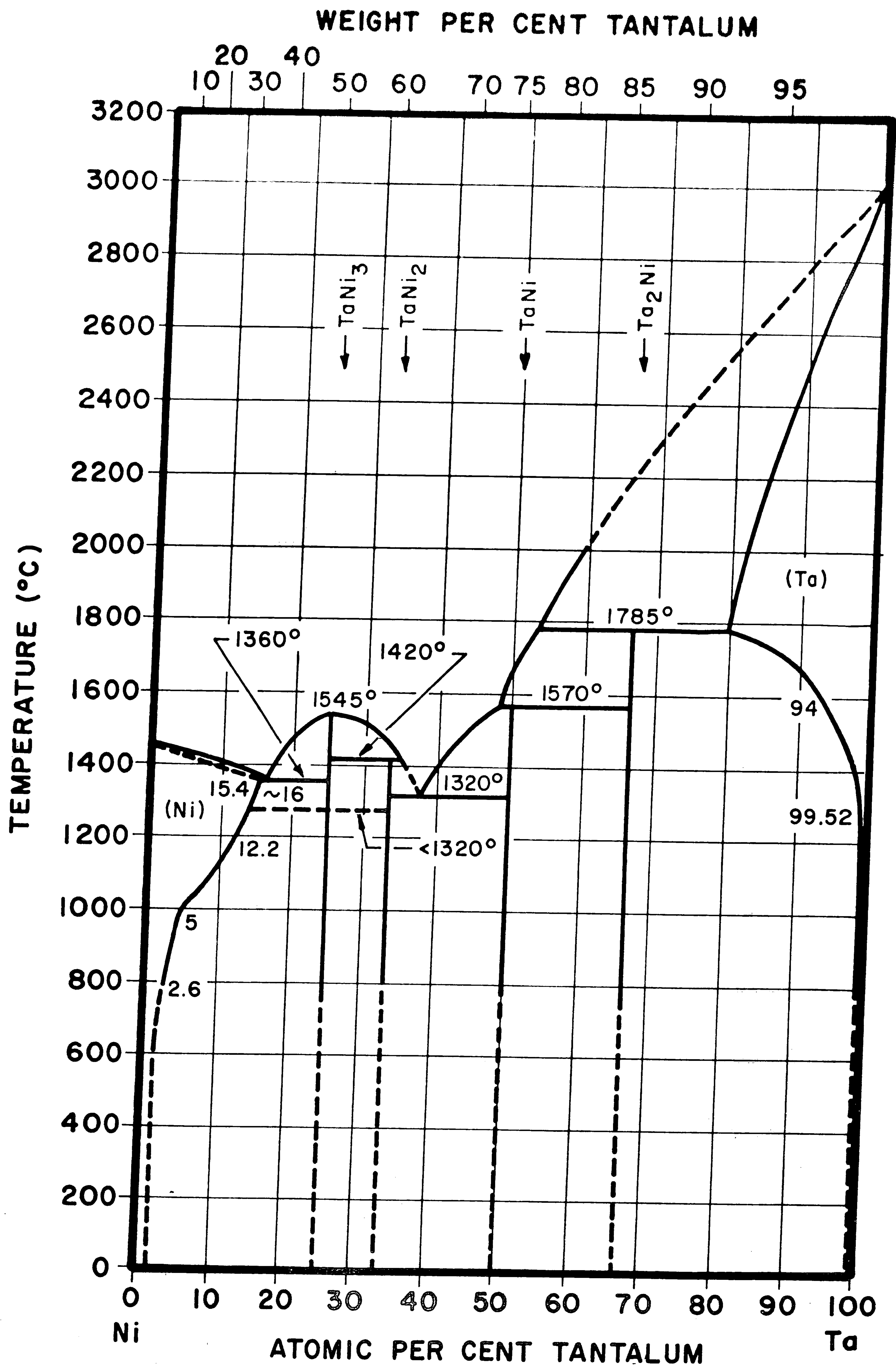

FIGURE 3

SUBSTRATE CONFIGURATIONS

Deposition Rate Determination

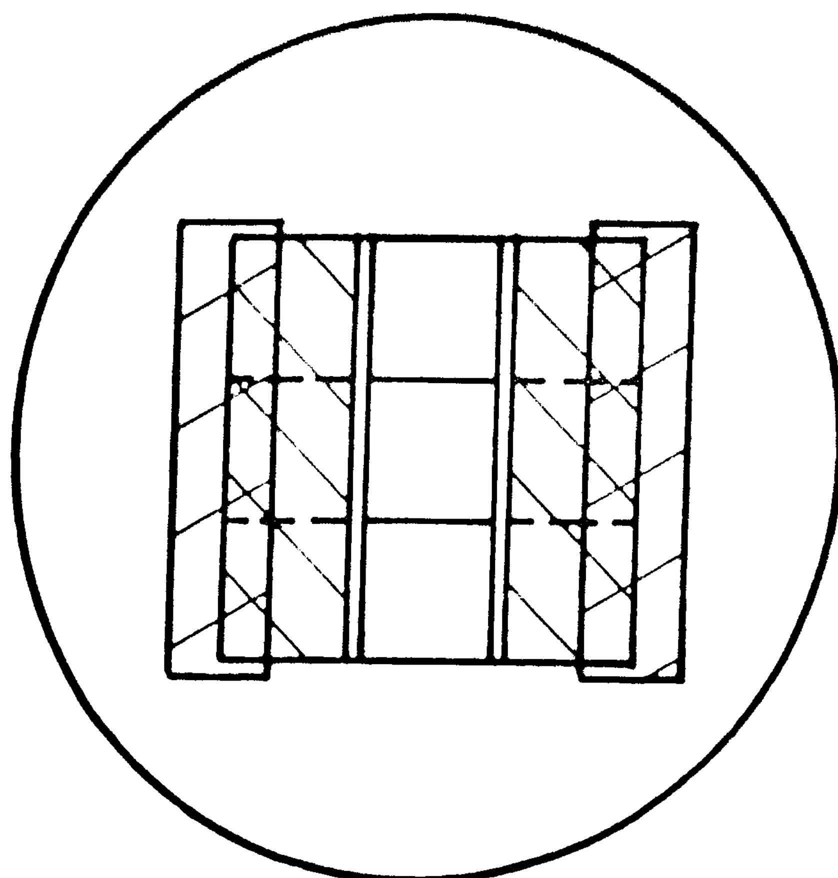

3: 1" x 3" slides
2: beveled 1" x 3" slides

Electron Microprobe Analysis

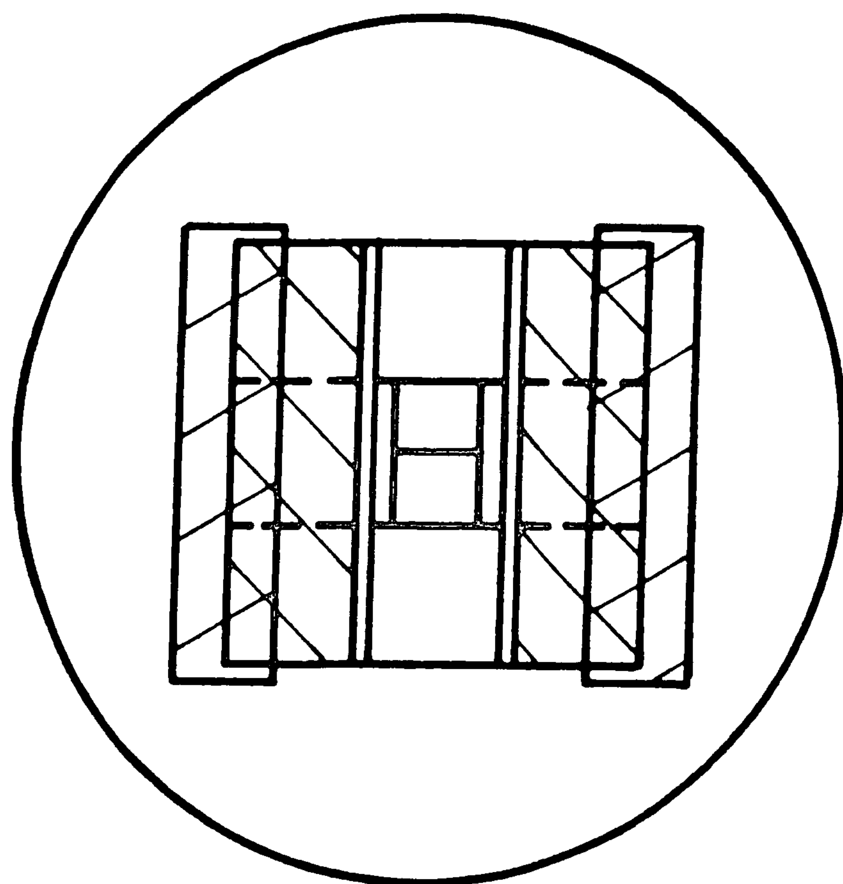

2: ¼" x ½" slides
2: 1" x 1¼" slides
2: 1" x 3" slides
2: beveled 1" x 3" slides

Transmission Electron Microscopy

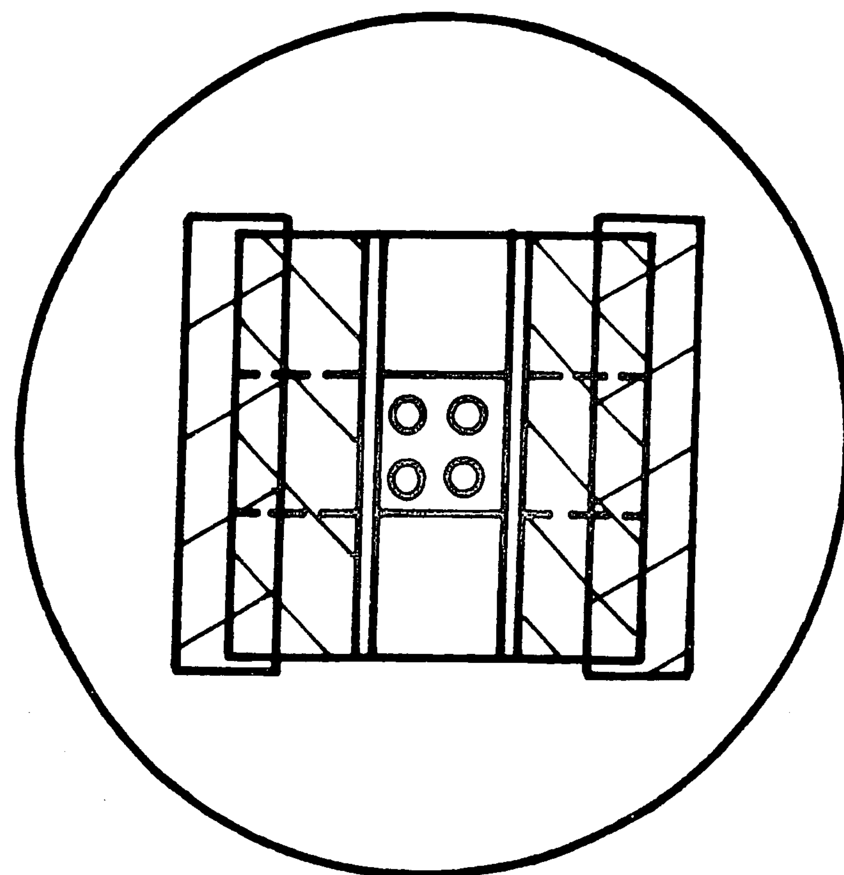

4: T.E.M. grids
1: 1" x 3" Al sheet with
   4 recessed holes
2: 1" x 3" slides
2: beveled 1" x 3" slides

FIGURE 4

R.F. SPUTTERING APPARATUS

FIGURE 5

VARIATION OF R.F. KILOVOLTAGE
WITH DEPOSITION TIME

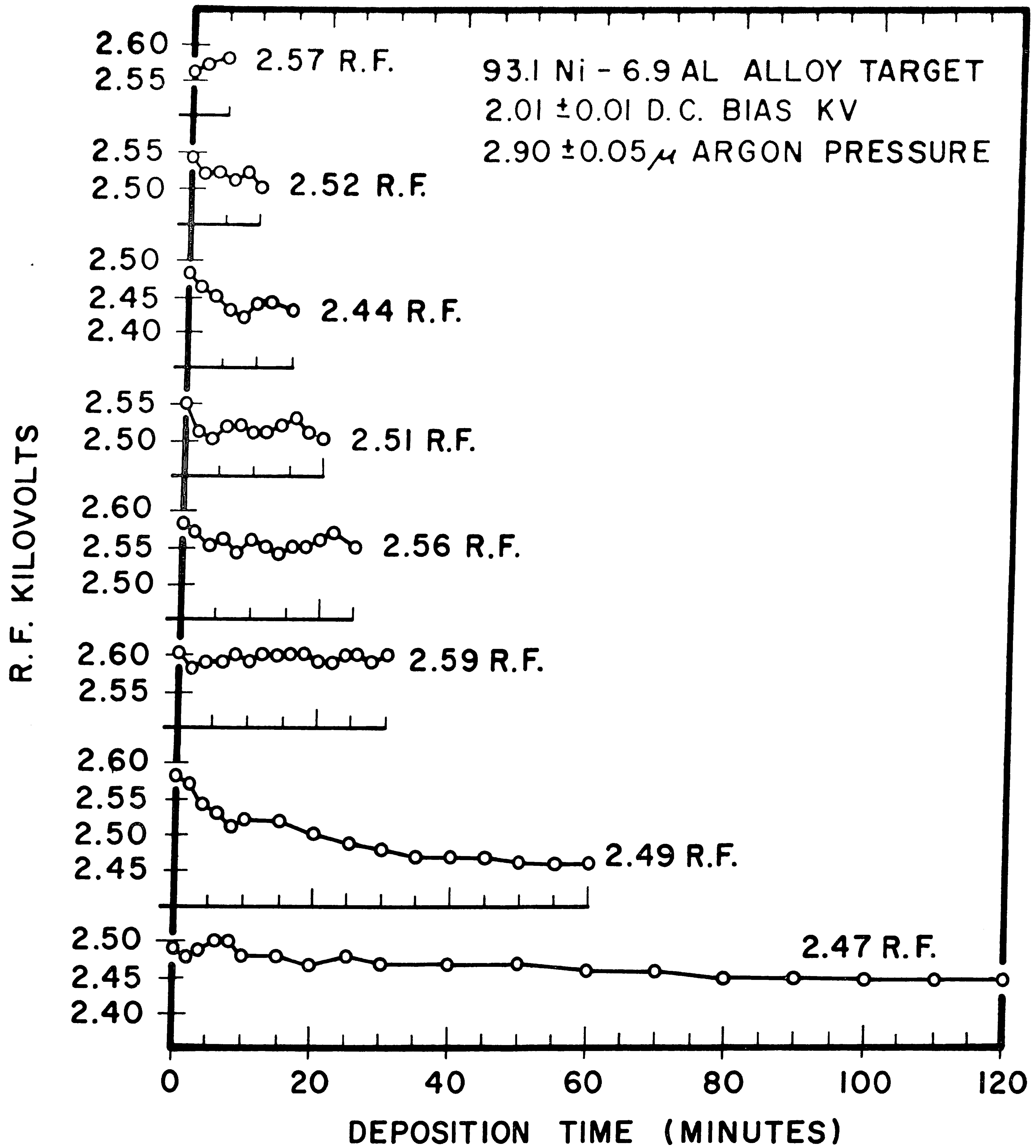

FIGURE 6

TARGET VOLTAGE AS A FUNCTION OF TIME

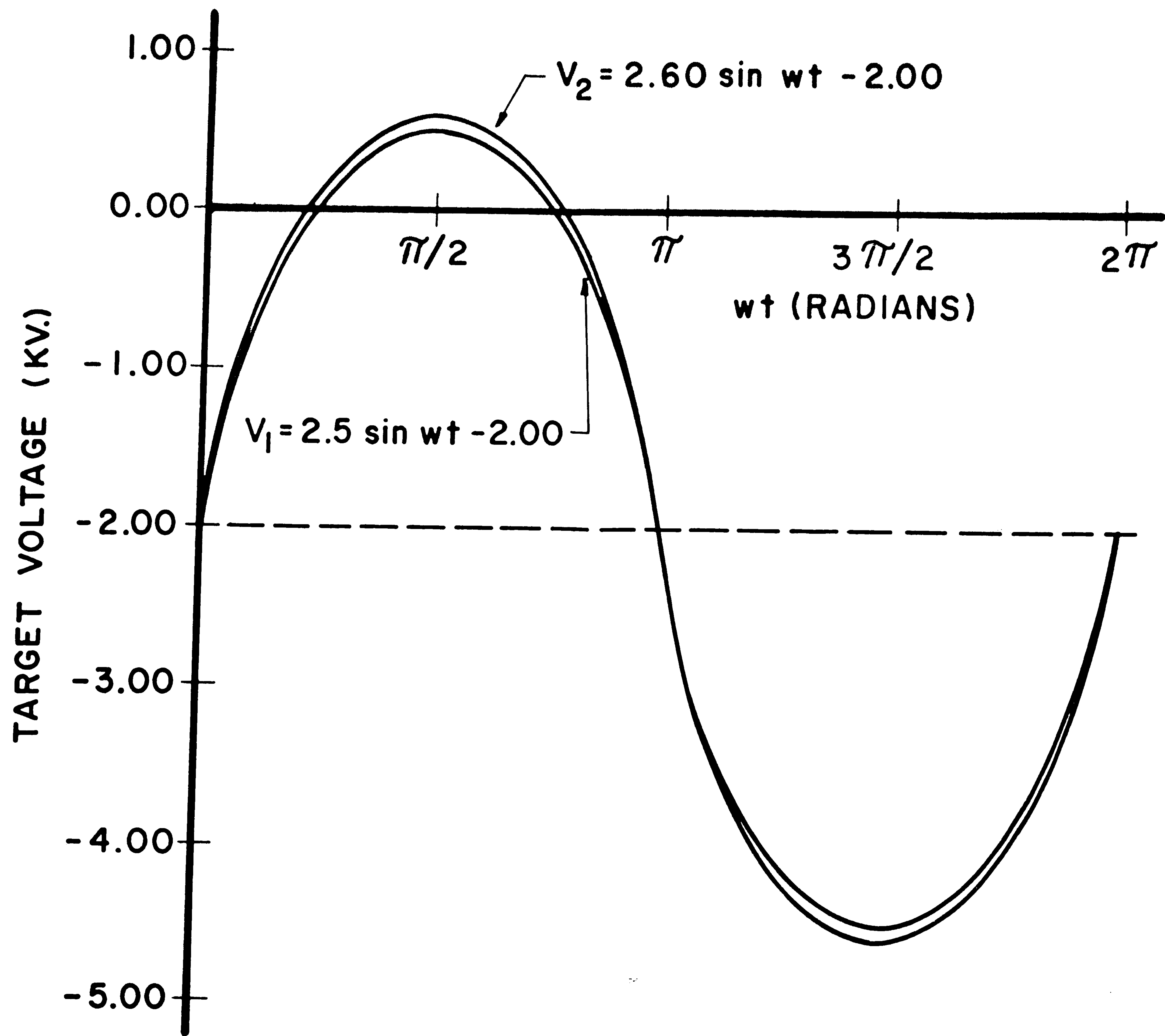

FIGURE 7

FILM THICKNESS VERSUS DEPOSITION
TIME FOR NI-AL ALLOY TARGET

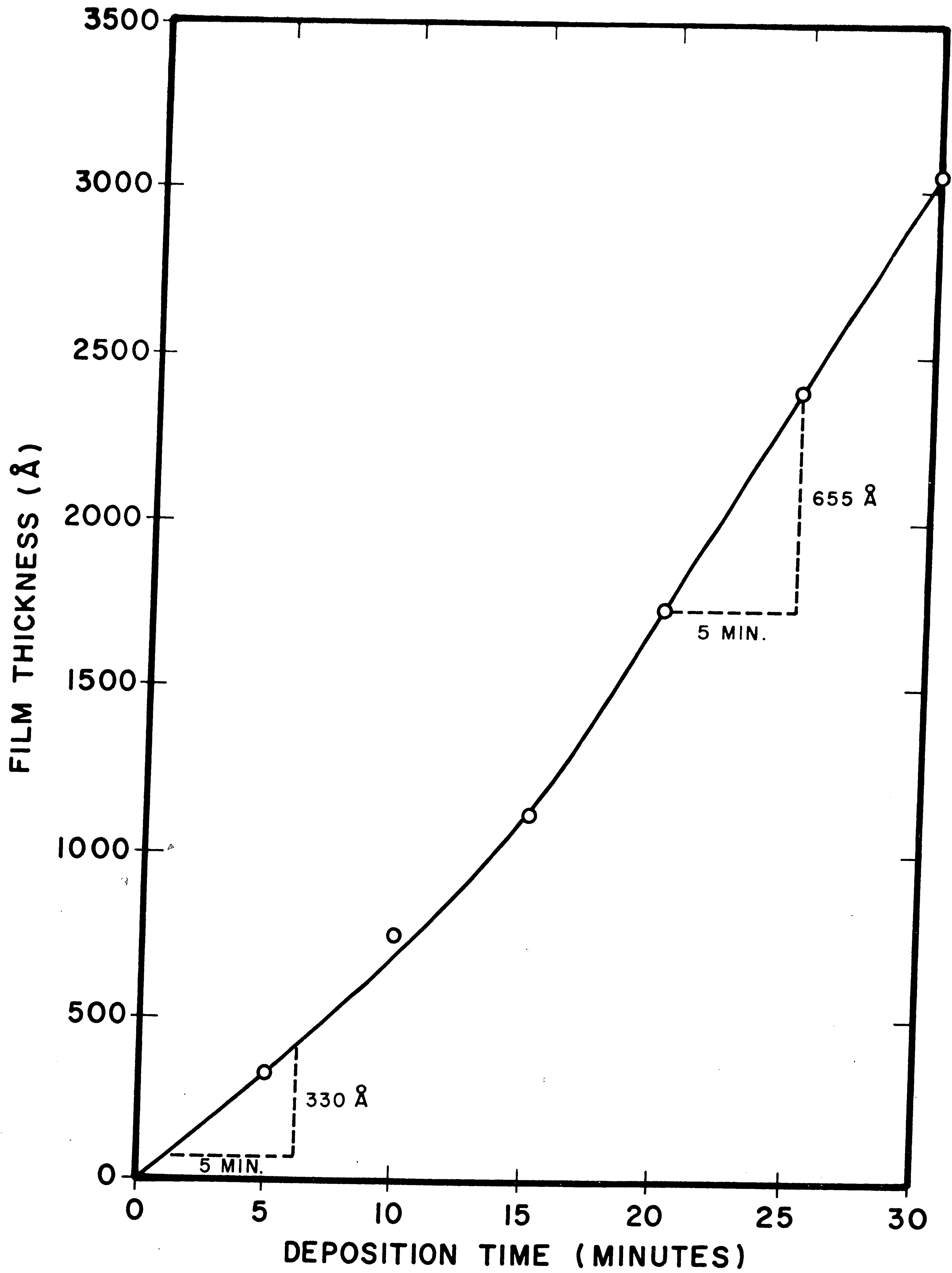

FIGURE 8

R.F. KILOVOLTAGE VERSUS
D.C. BIAS KILOVOLTAGE

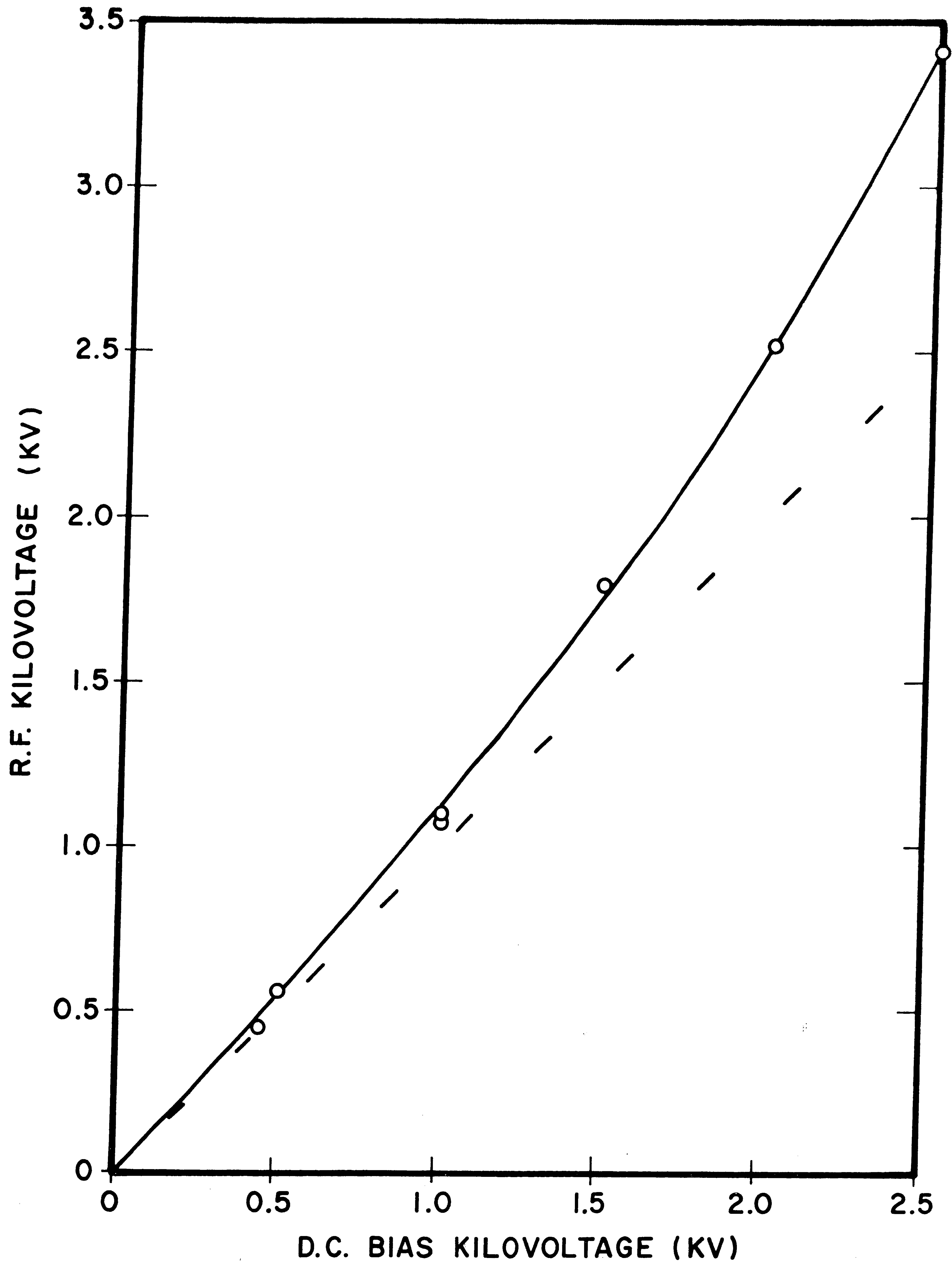

FIGURE 9

TARGET VOLTAGE WITH RESPECT TO GROUND
VERSUS TIME FOR VARIOUS VOLTAGE CONDITIONS

$$V = V_{RF} \sin wt - V_{DC} - V_P$$

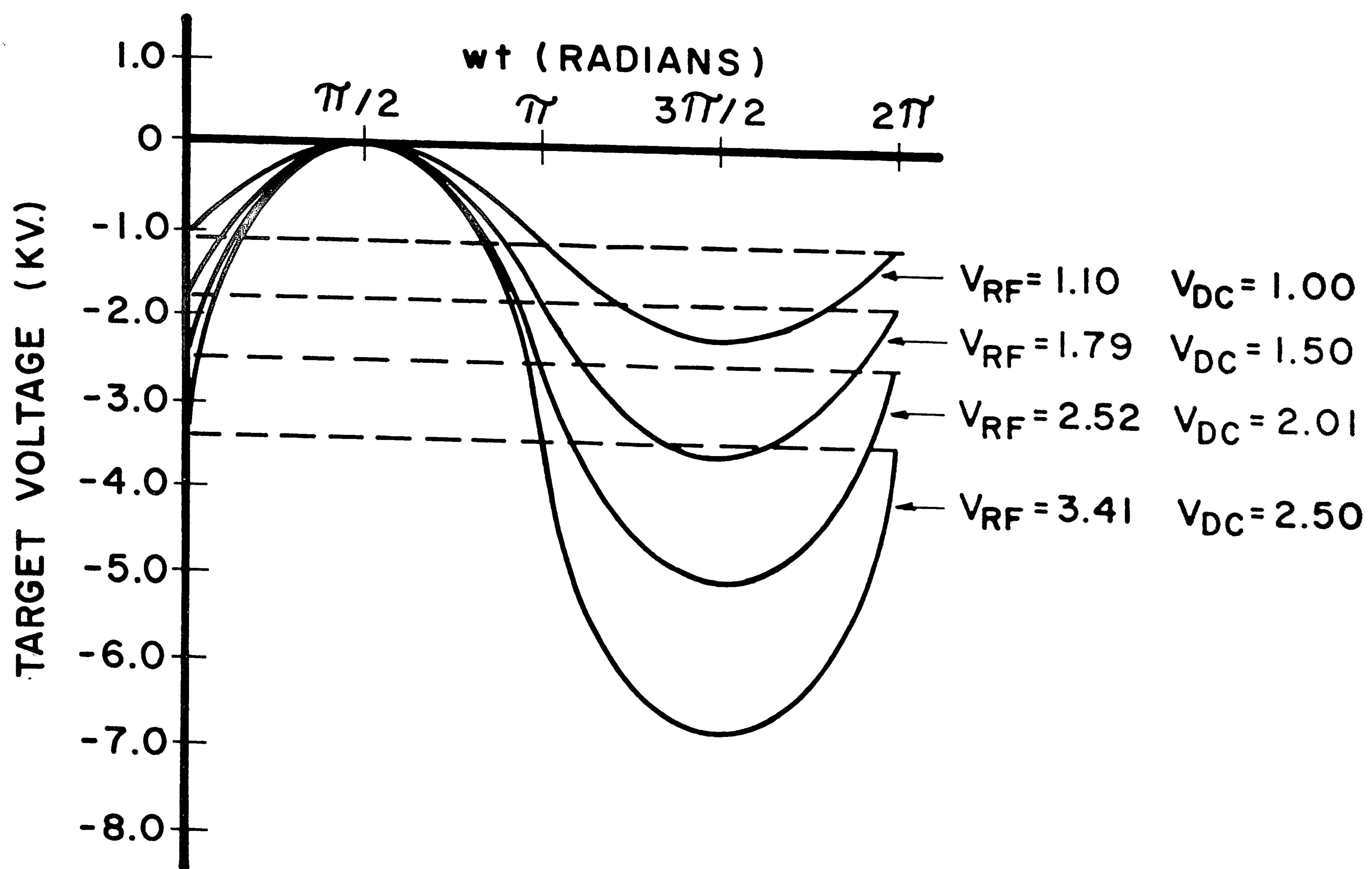

FIGURE 10

SPUTTERING YIELD OF NI AND AL VERSUS Ar^+ ENERGY

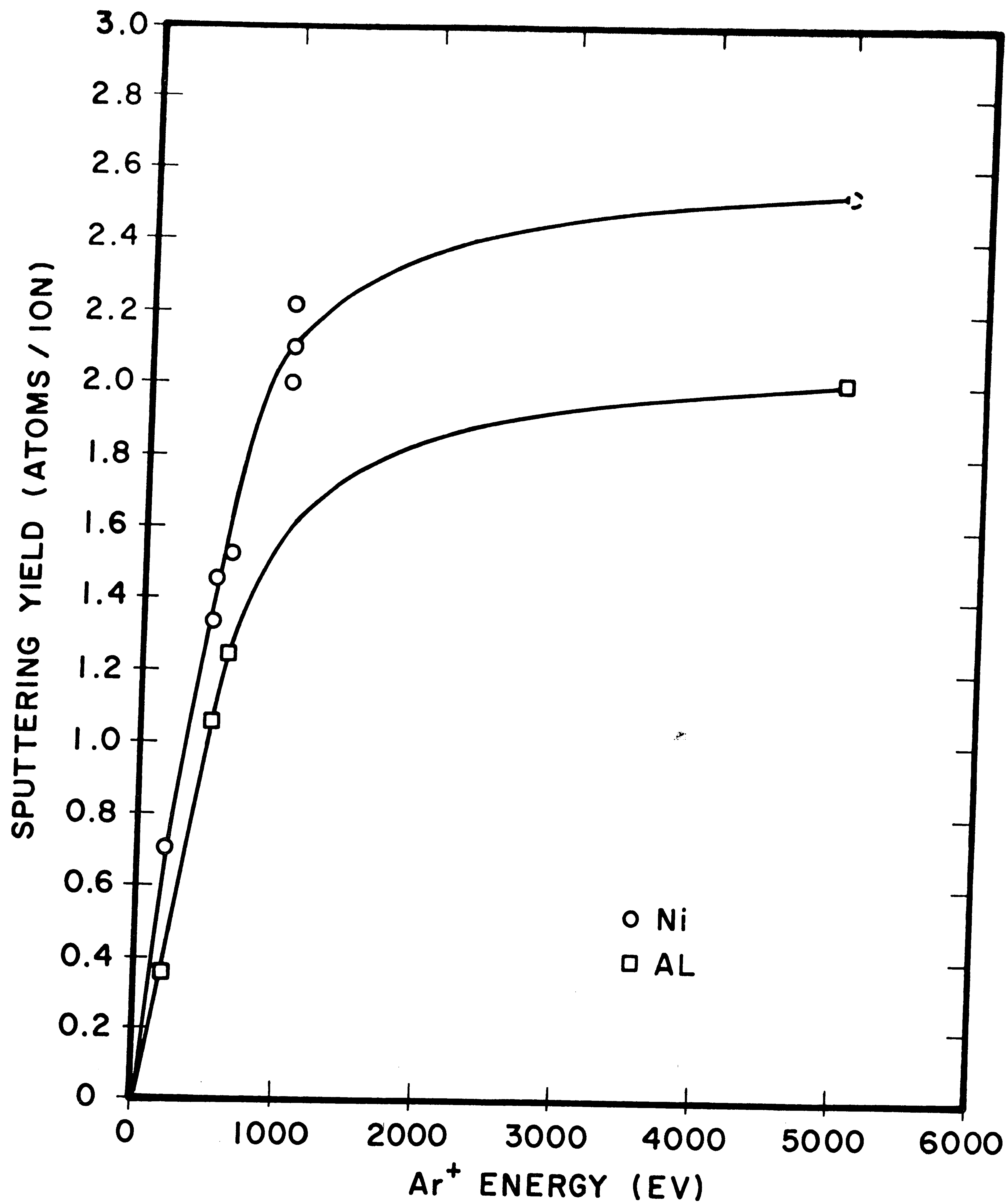

FIGURE 11

FILM THICKNESS VERSUS DEPOSITION TIME FOR VARIOUS VOLTAGE CONDITIONS ON NI-AL ALLOY TARGET

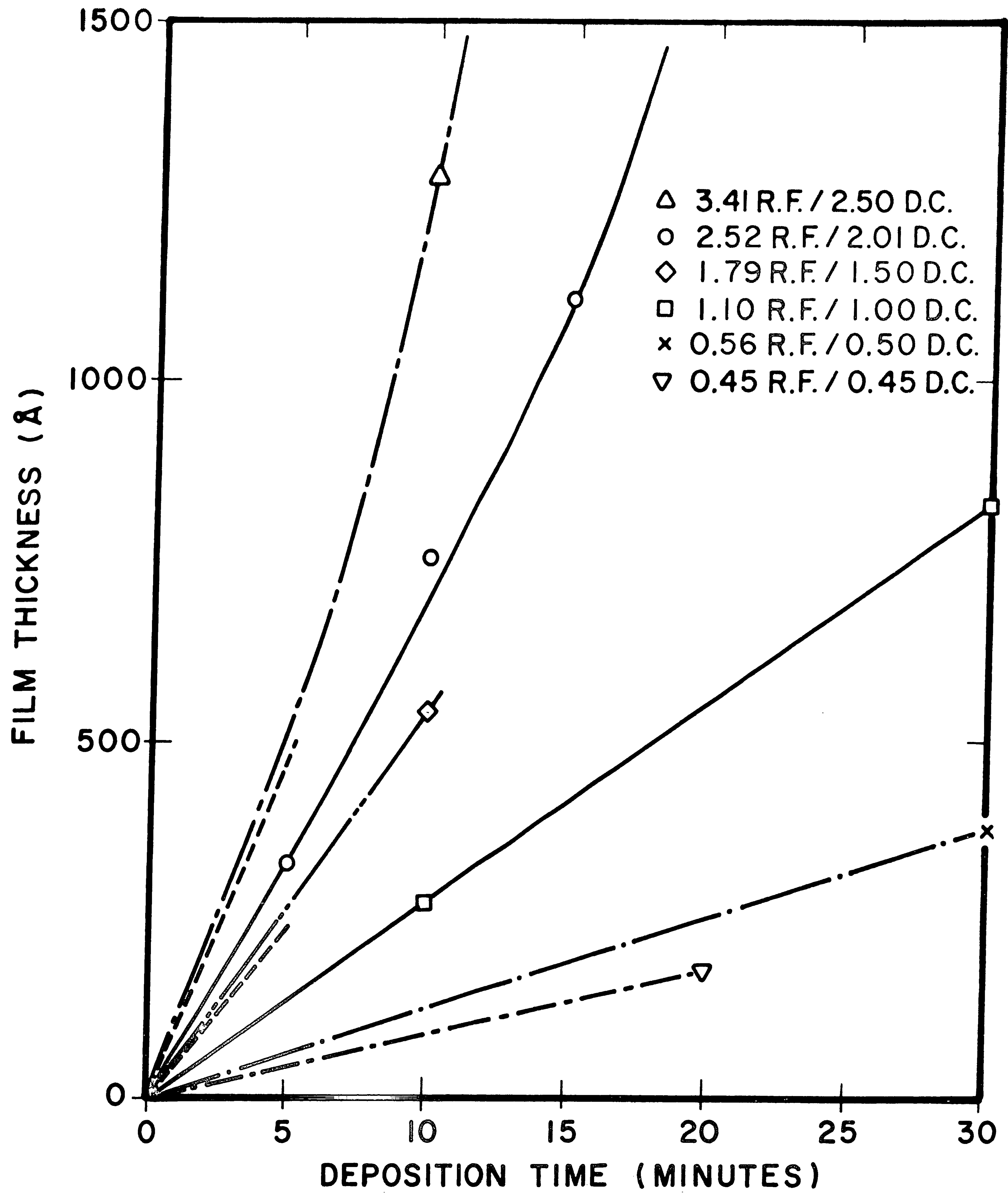

FIGURE 12

FILM THICKNESS AND DEPOSITION RATE VERSUS
R.F. KILOVOLTAGE FOR NI-AL ALLOY TARGET

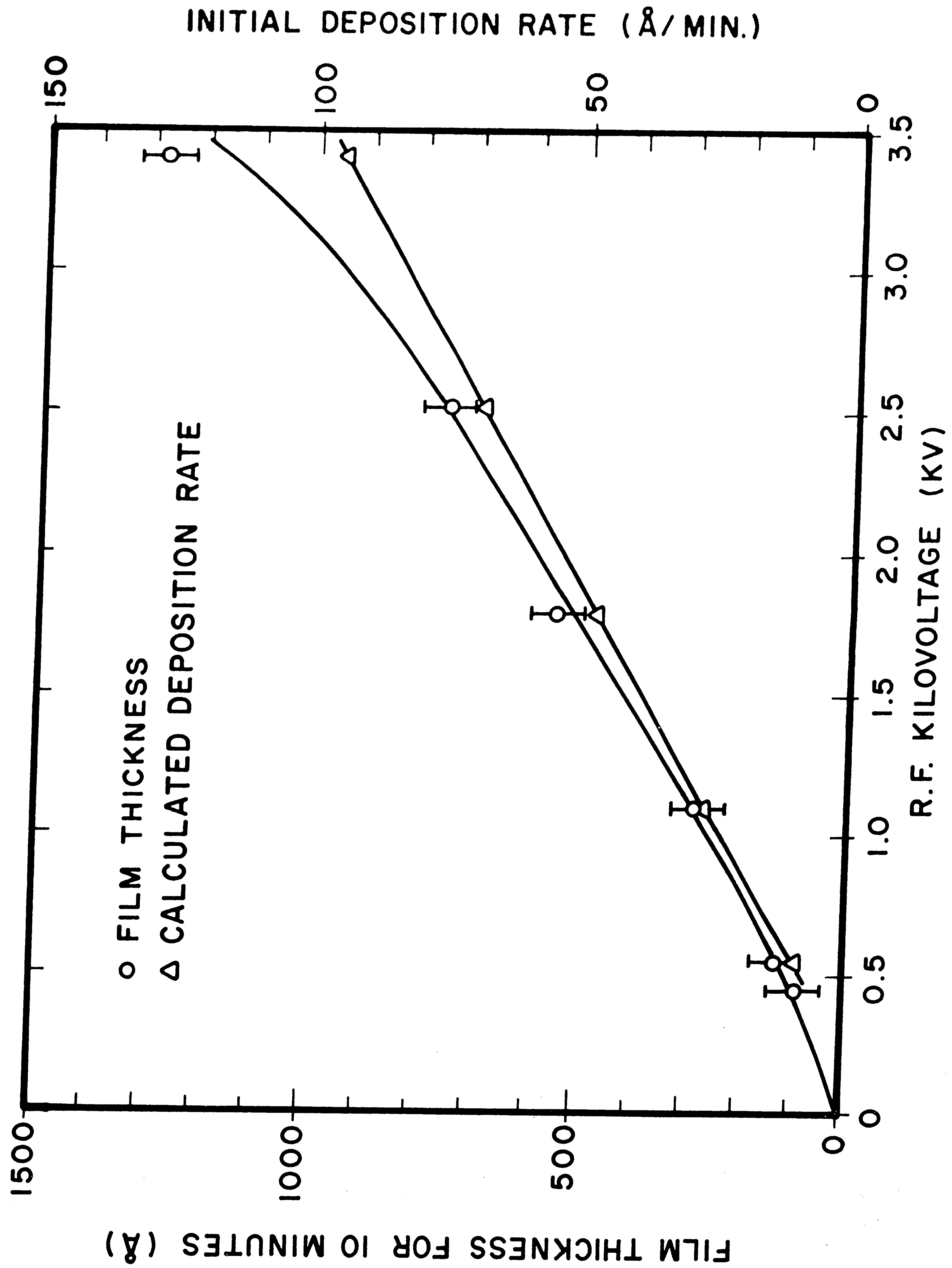

FIGURE 13

FILM THICKNESS FOR 10 MINUTES VERSUS
ARGON PRESSURE FOR NI-AL ALLOY TARGET

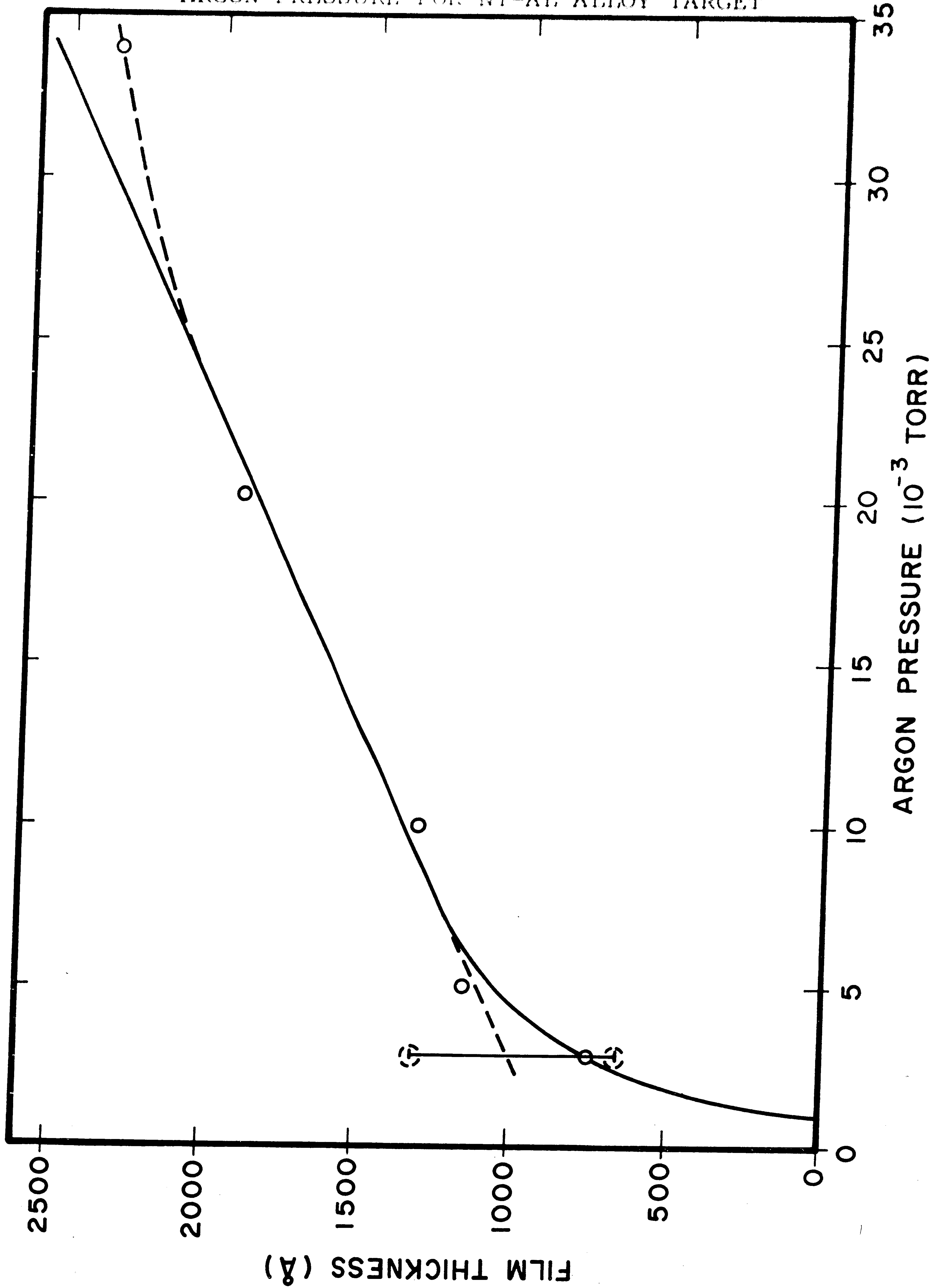

FIGURE 14

MEAN FREE PATH OF ARGON
VERSUS ARGON PRESSURE

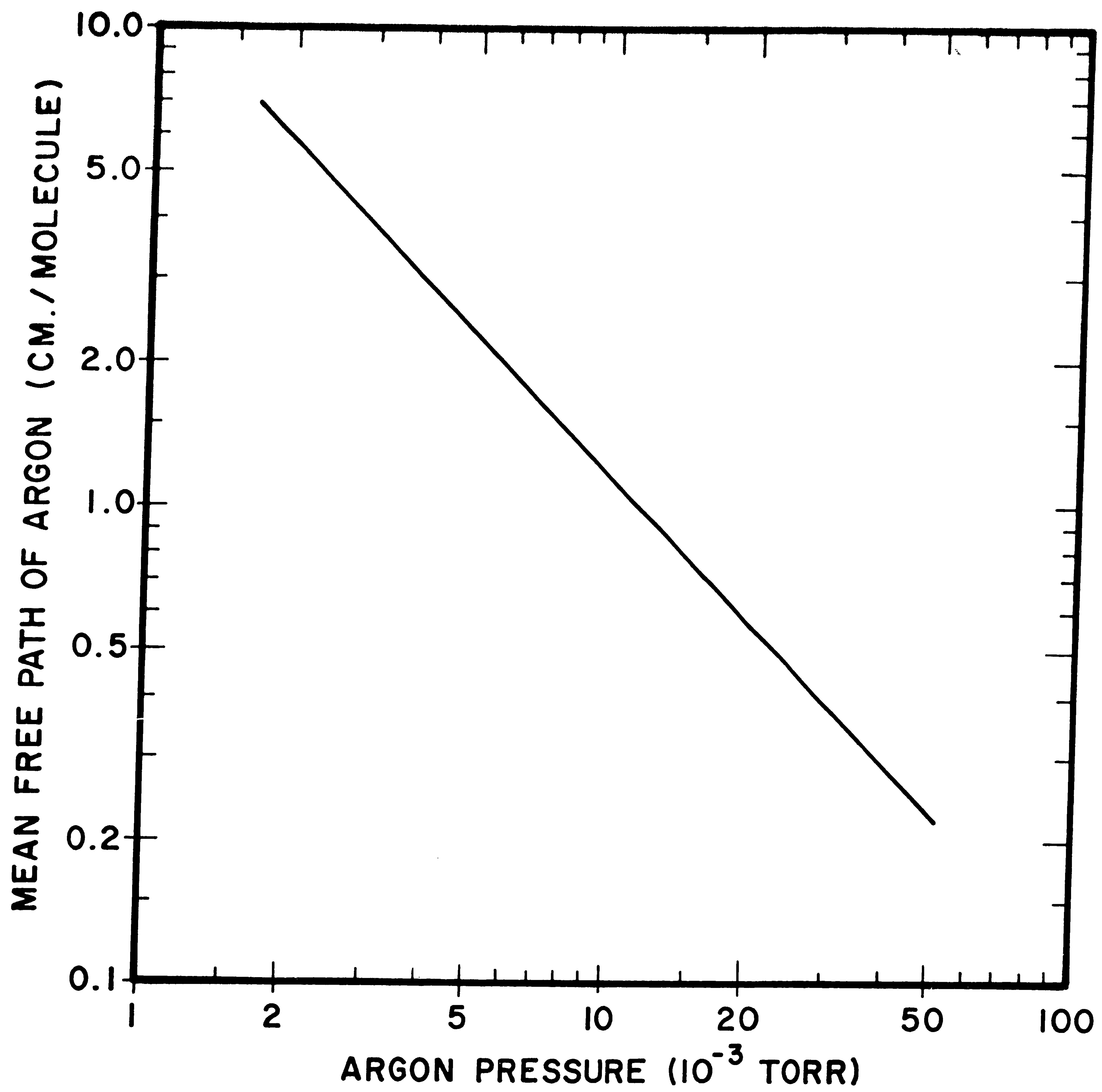

FIGURE 15

R.F. FORWARD POWER VERSUS ARGON PRESSURE FOR NI-AL ALLOY TARGET

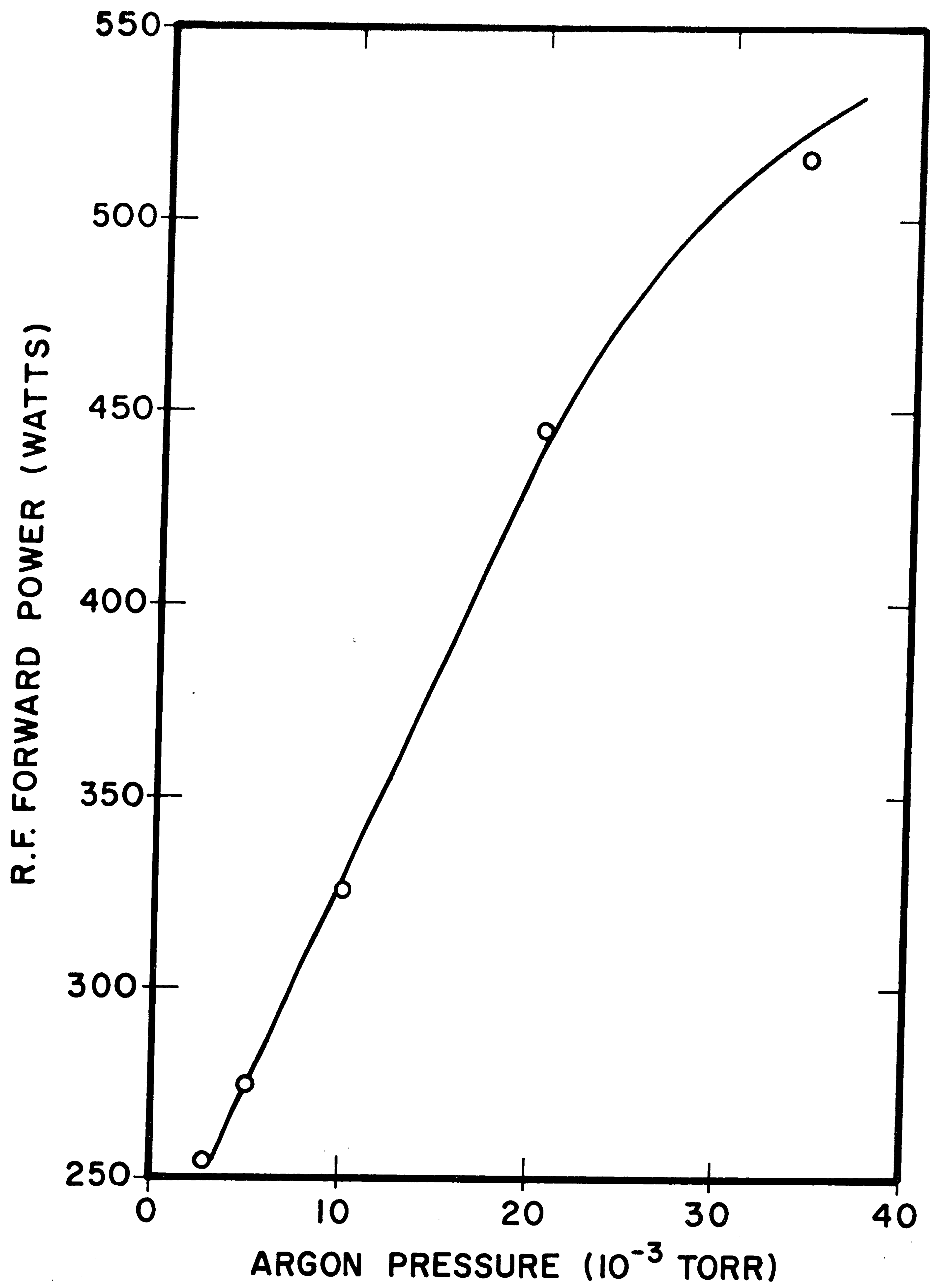

FIGURE 16

PLOT OF ALUMINUM CONTENT IN PLASMA SPRAYED TARGET VERSUS ALUMINUM CONTENT IN POWDER

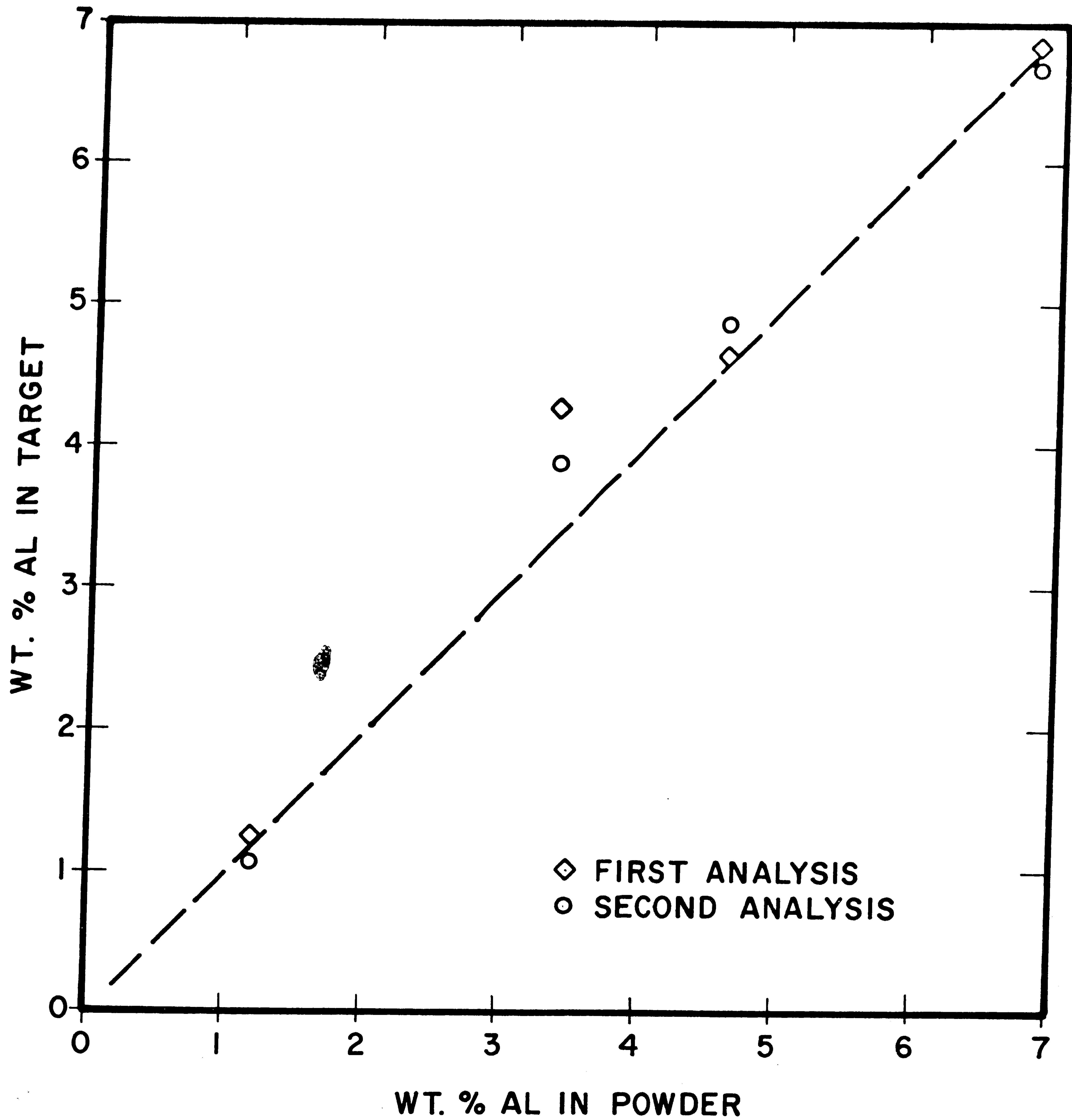

FIGURE 17

PLOT OF TANTALUM CONTENT IN PLASMA SPRAYED TARGET VERSUS TANTALUM CONTENT IN POWDER

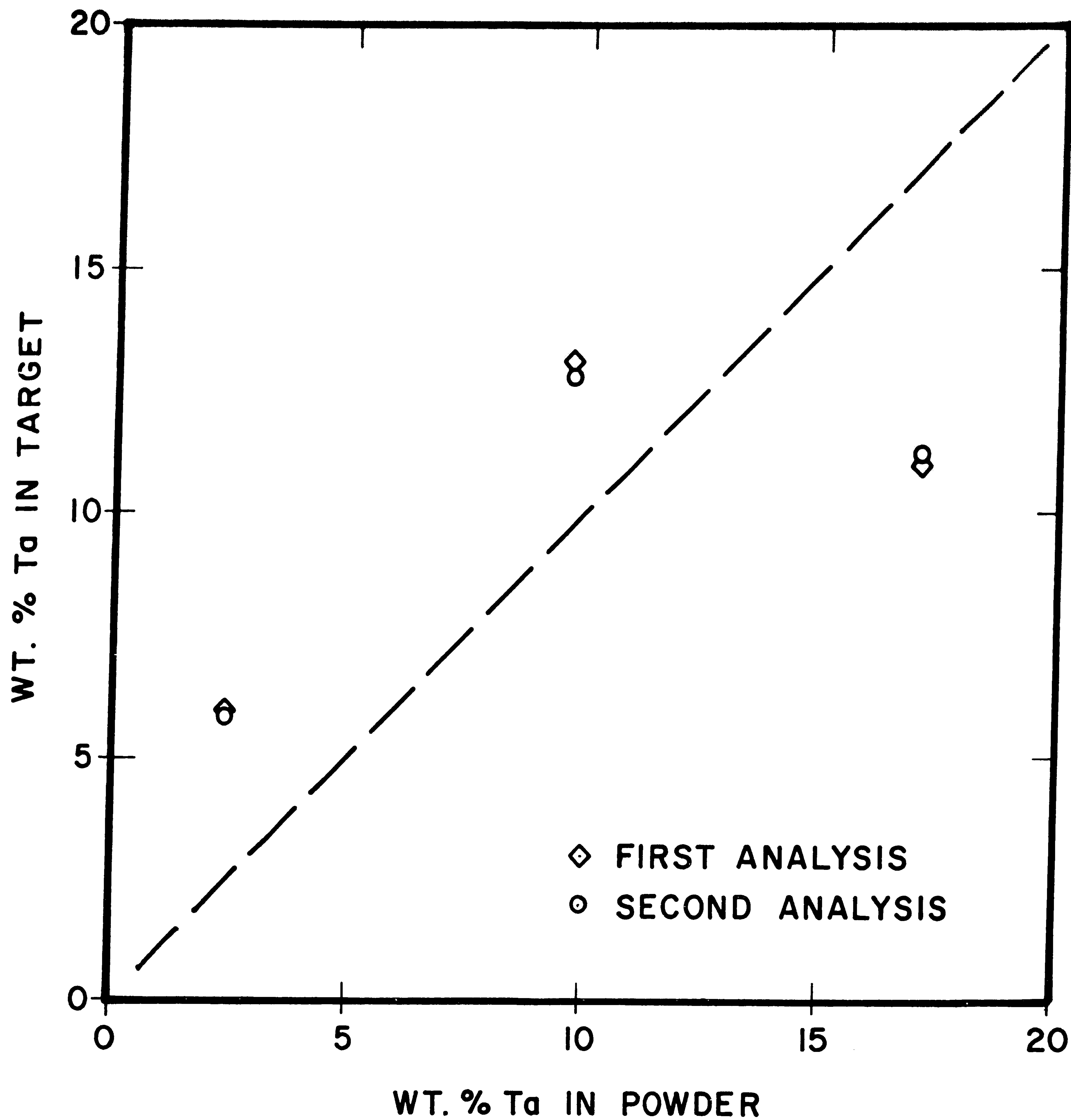

FIGURE 18

SILICON K ALPHA INTENSITY VERSUS MICROPROBE KILOVOLTAGE FOR THIN FILMS AND BULK SAMPLE

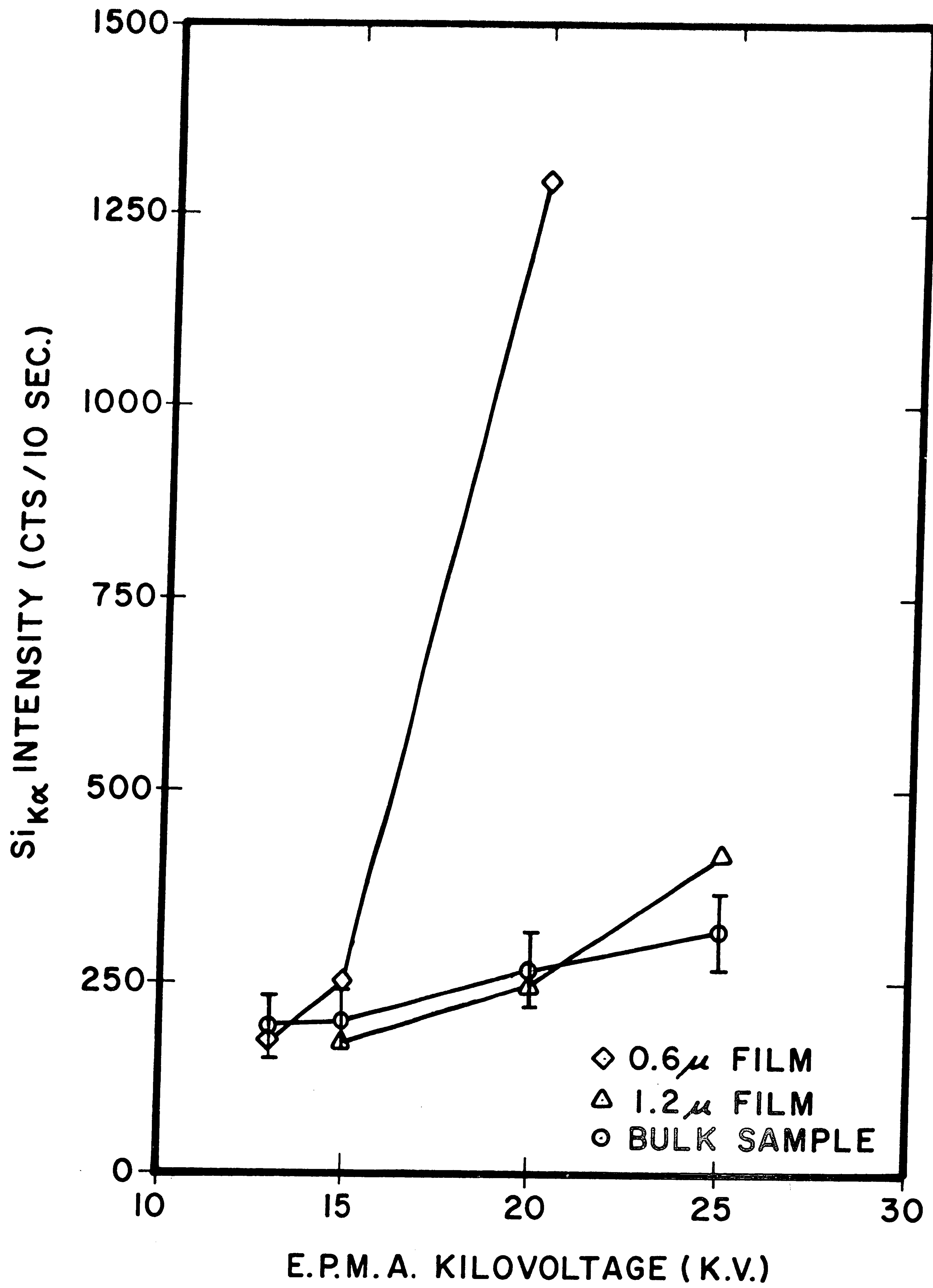

FIGURE 19

COMPARISON OF MICROPROBE RESULTS FOR
1.2 μ NI-AL FILMS AT 8 KV AND 20 KV

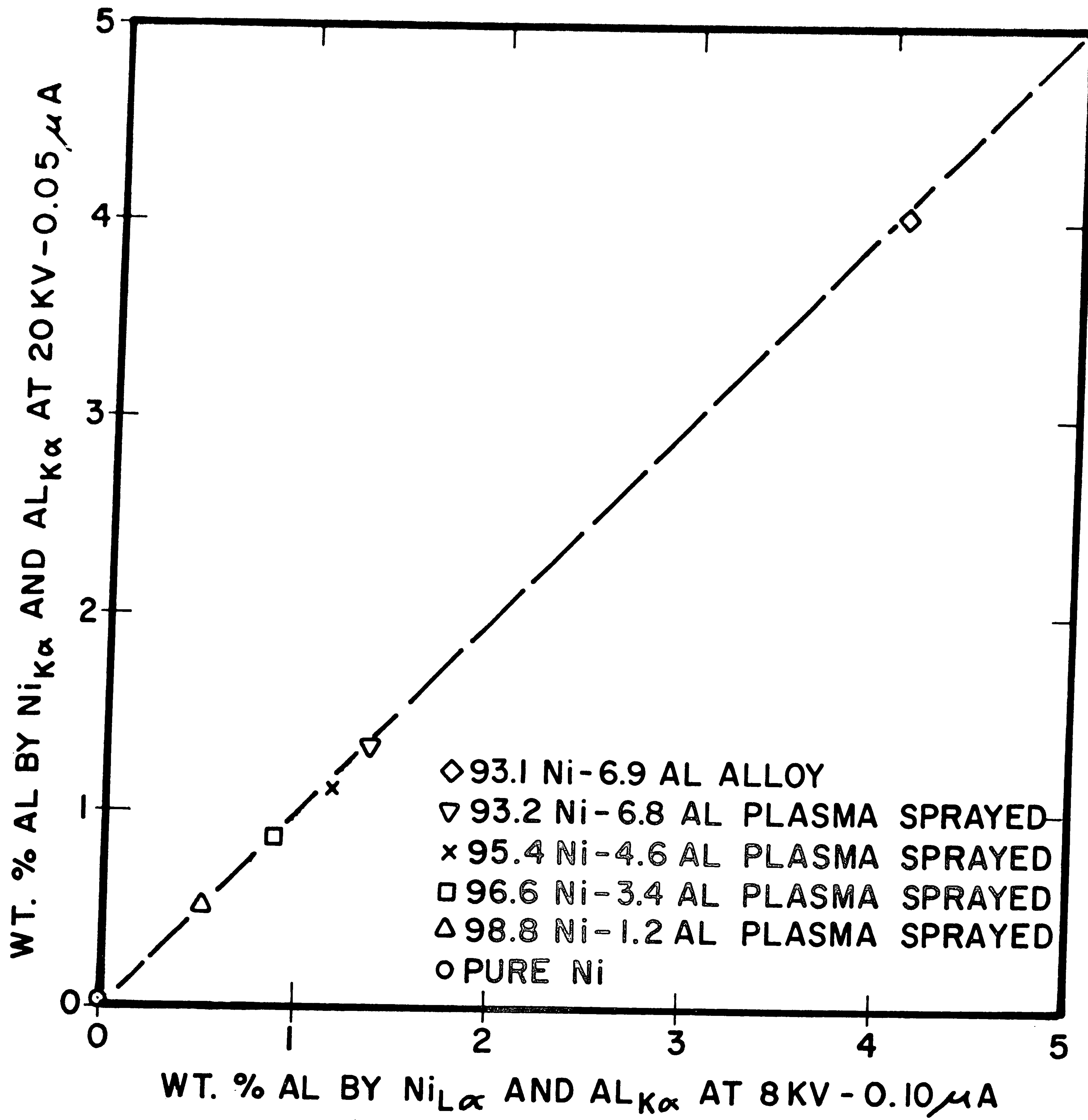

FIGURE 20

PLOT OF ALUMINUM CONTENT IN SPUTTERED FILM VERSUS ALUMINUM CONTENT IN TARGET

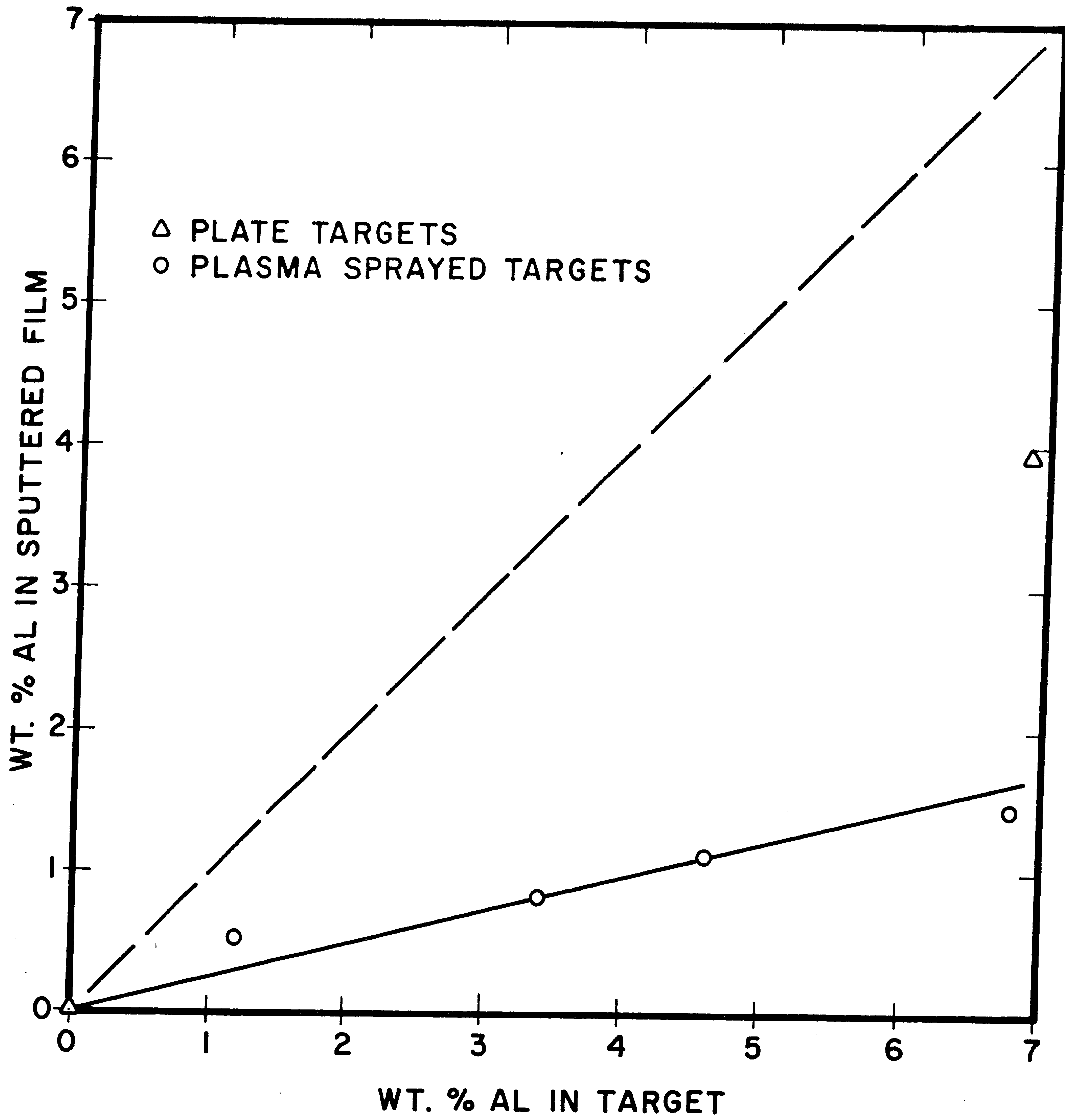

FIGURE 21

PLOT OF TANTALUM CONTENT IN SPUTTERED FILM VERSUS TANTALUM CONTENT IN TARGET

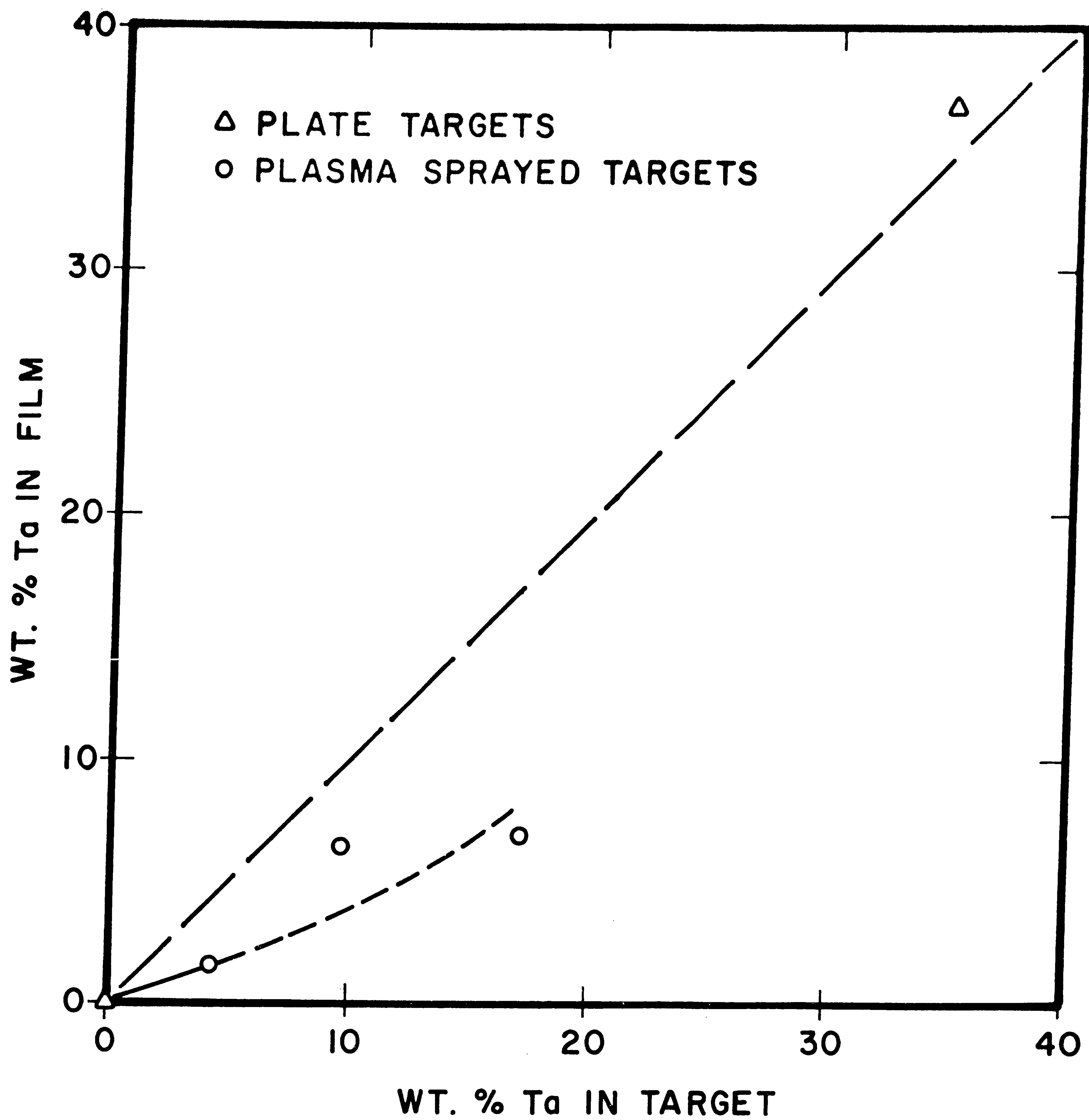

FIGURE 22

SOLID STATE DETECTOR SCANS FOR
PURE NICKEL TARGET AND 1.2 μ THIN FILM

Target: pure Ni

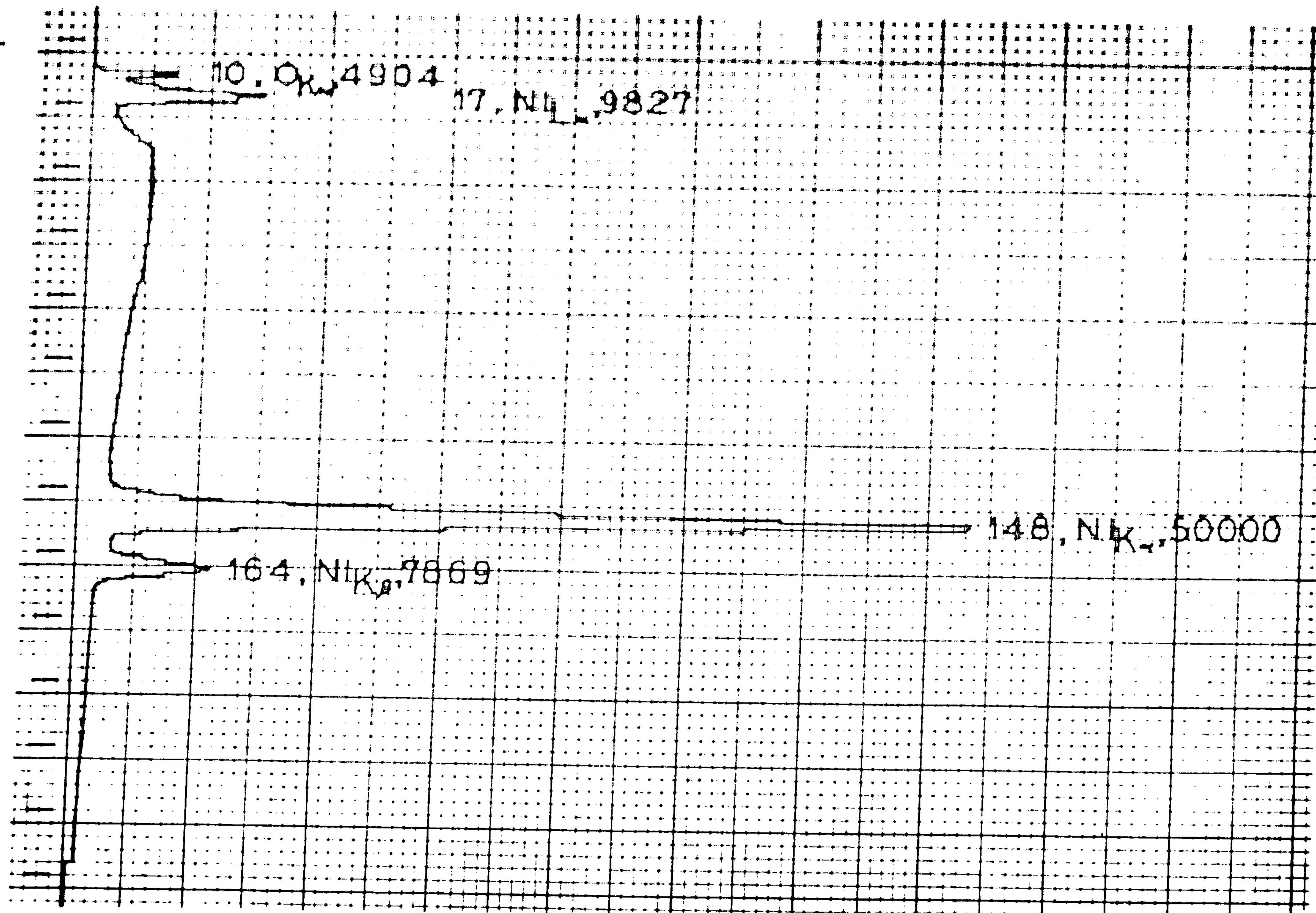

Thin film: pure Ni

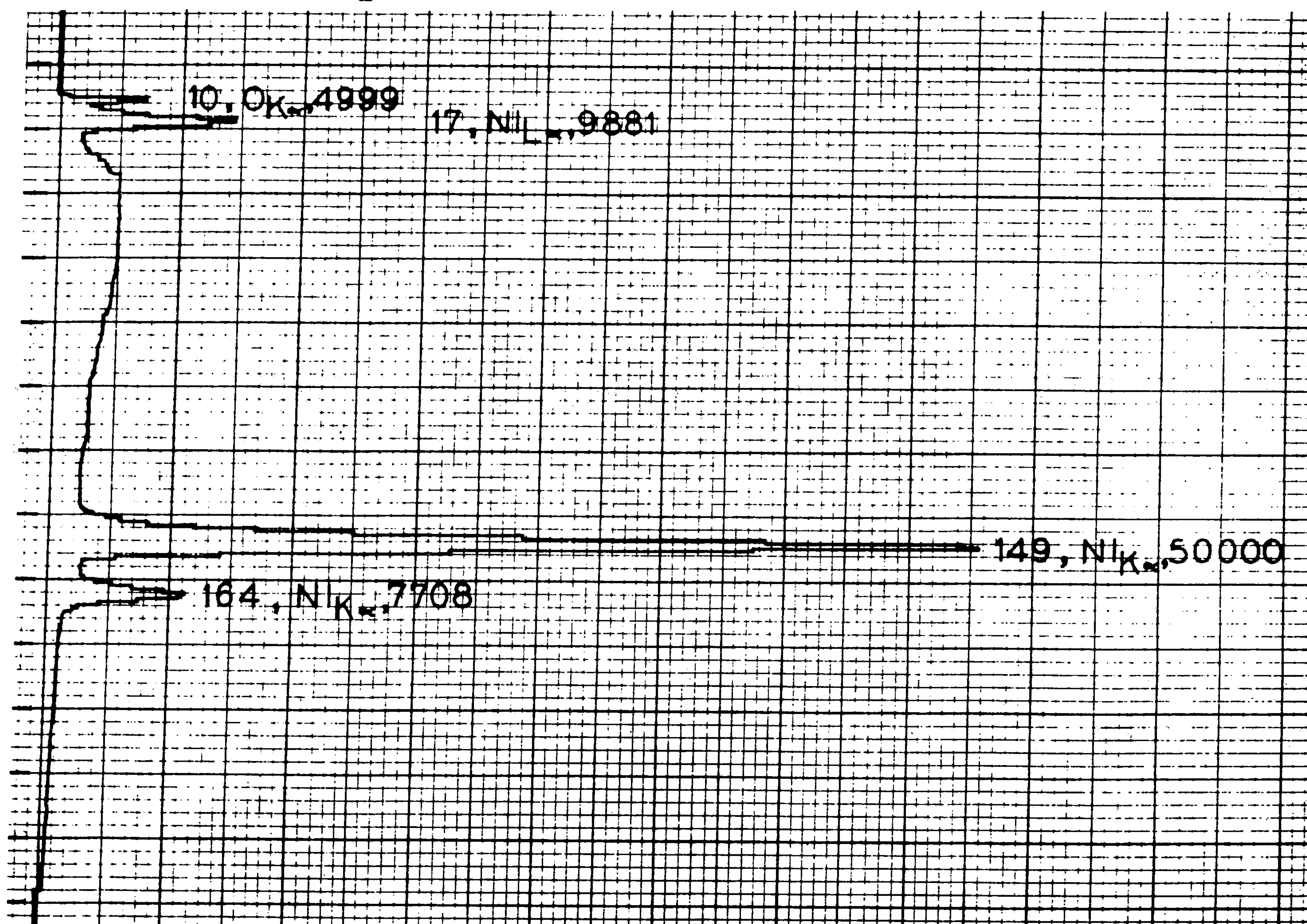

FIGURE 23

SOLID STATE DETECTOR SCANS FOR NI-AL ALLOY TARGET AND 1.2 μ THIN FILM

Target: 93.1Ni - 6.9Al

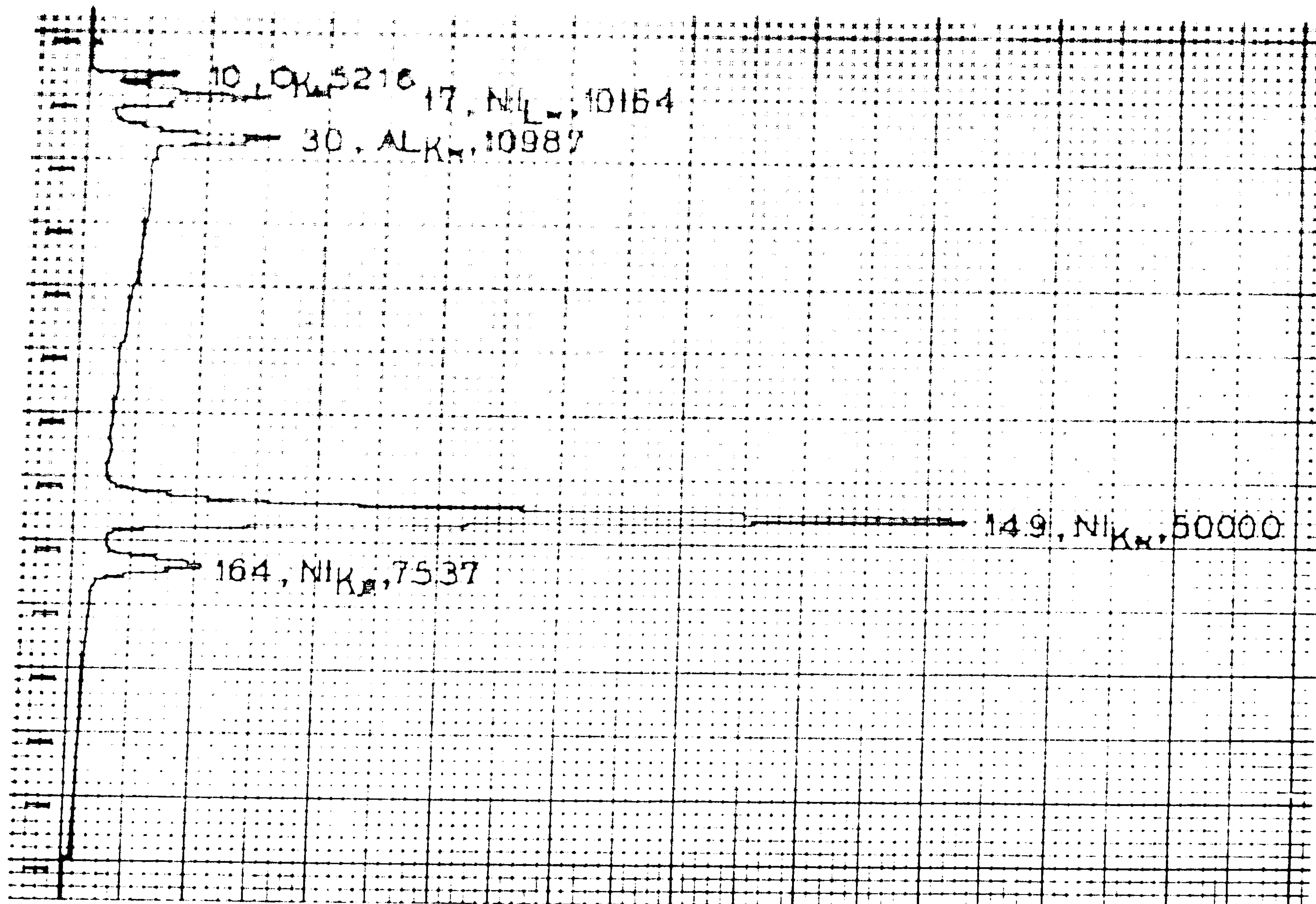

Thin film: 96.05Ni - 3.95Al

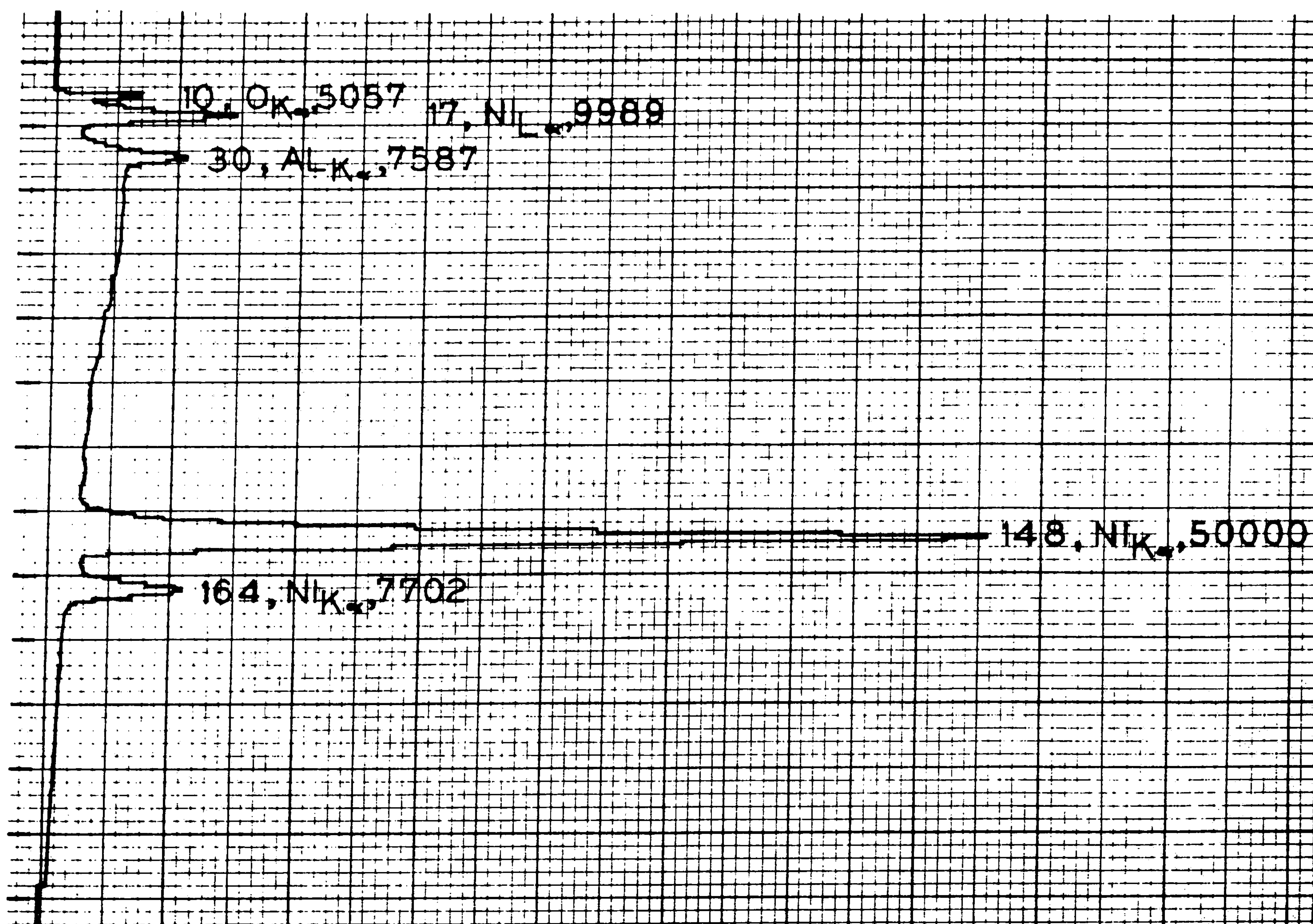

FIGURE 24

SOLID STATE DETECTOR SCANS FOR NI-TA
ALLOY TARGET AND 1.2 μ THIN FILM

Target: 65.2Ni - 34.8Ta

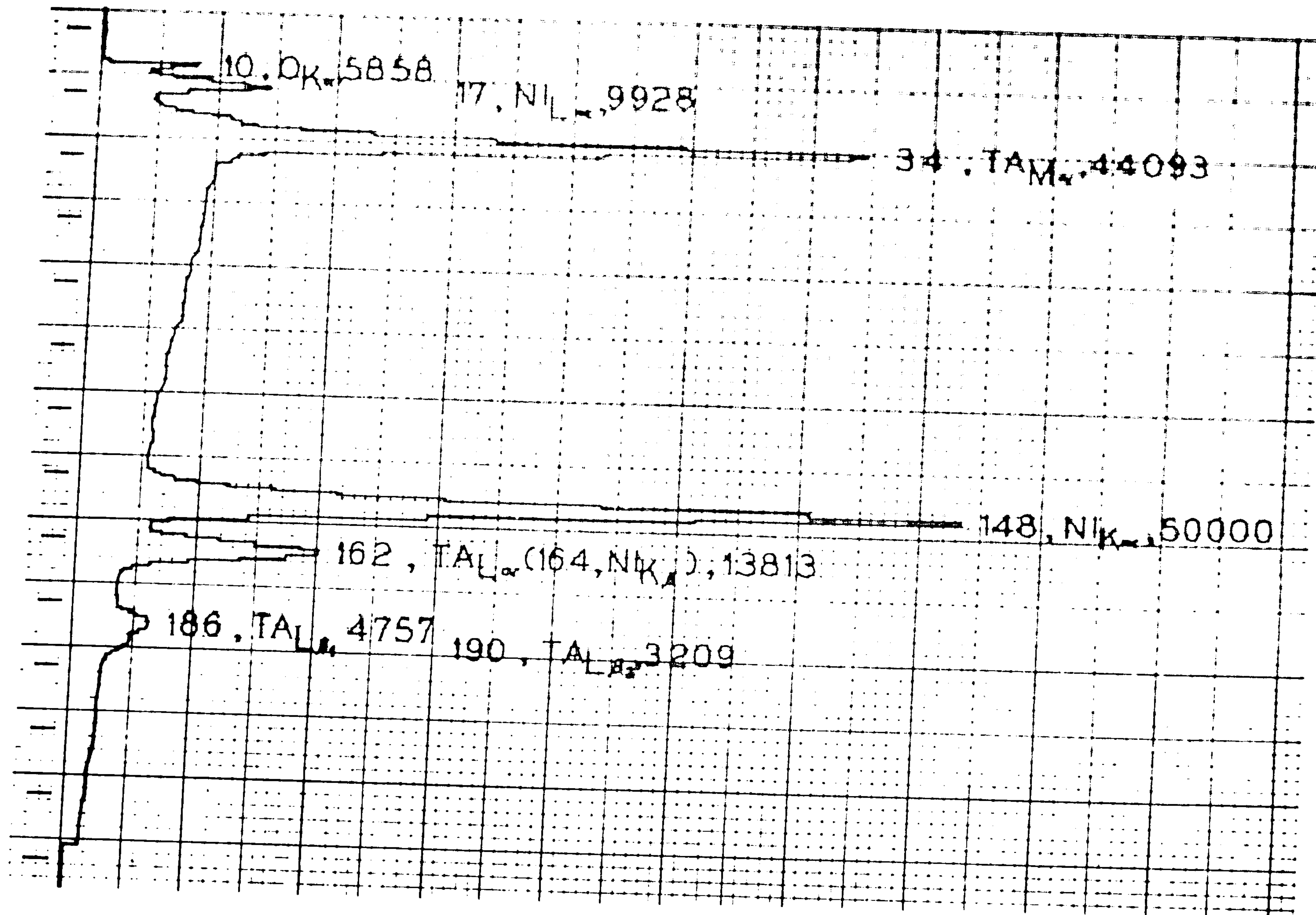

Thin film: 54.4Ni - 36.7Ta - Ar

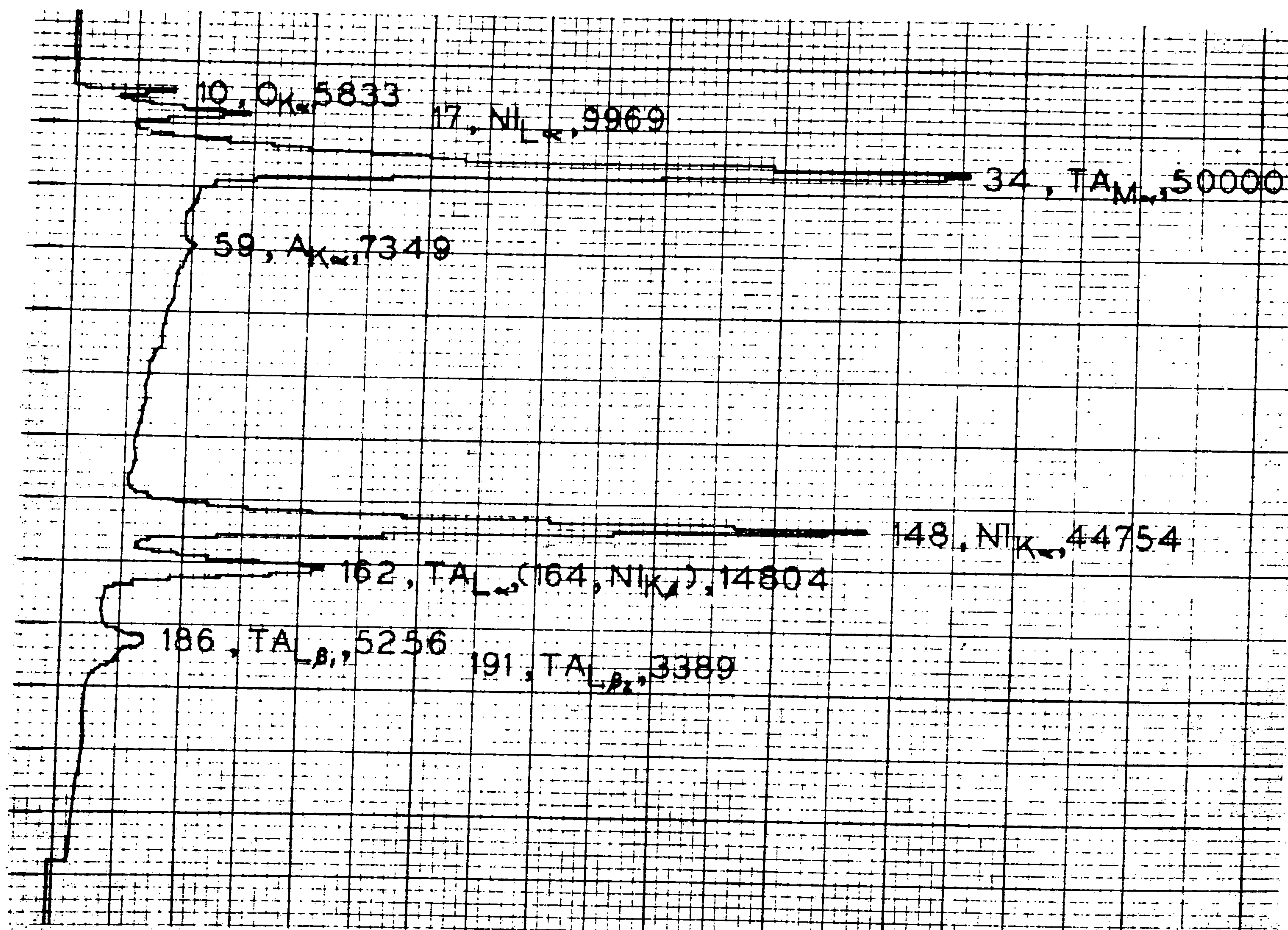

FIGURE 25

SURFACE TOPOGRAPHY OF NI - 9.7TA
PLASMA SPRAYED TARGET

(a) unsputtered, 500x, 40° tilt

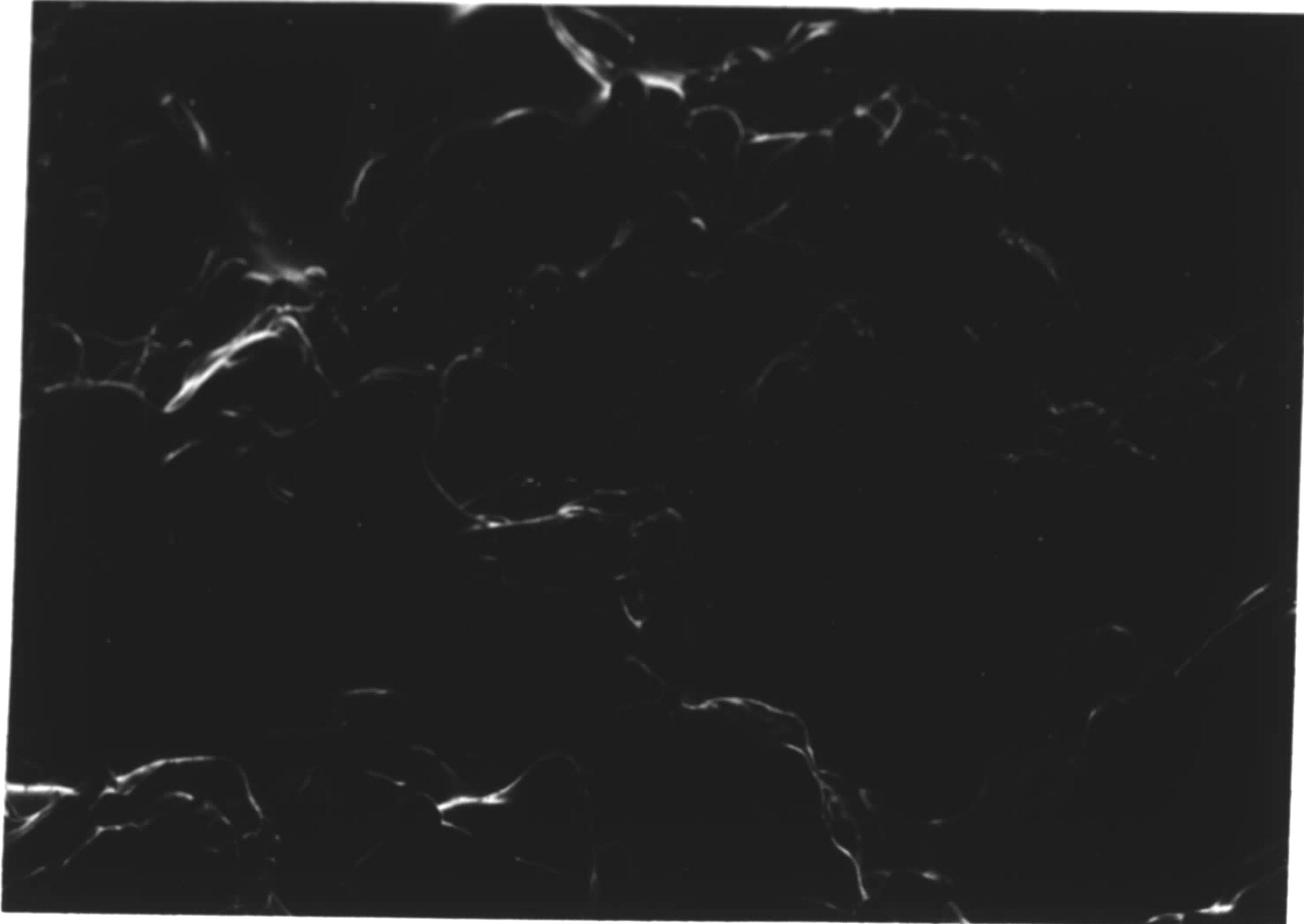

(b) sputtered, 500x, 40°tilt

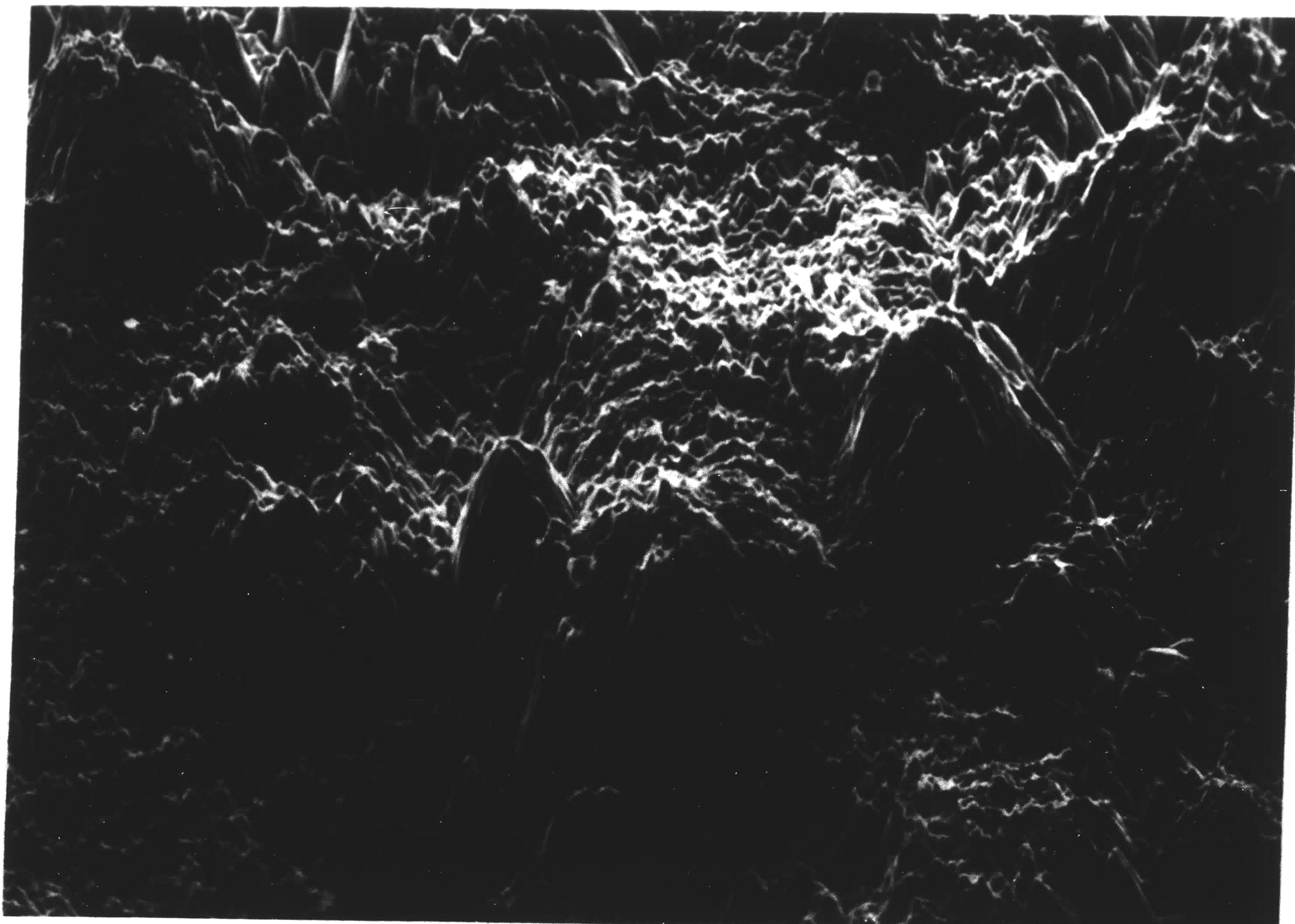

FIGURE 26

SURFACE TOPOGRAPHY OF NI - 6.8AL
PLASMA SPRAYED TARGET

(a) unsputtered, 500x, 40° tilt

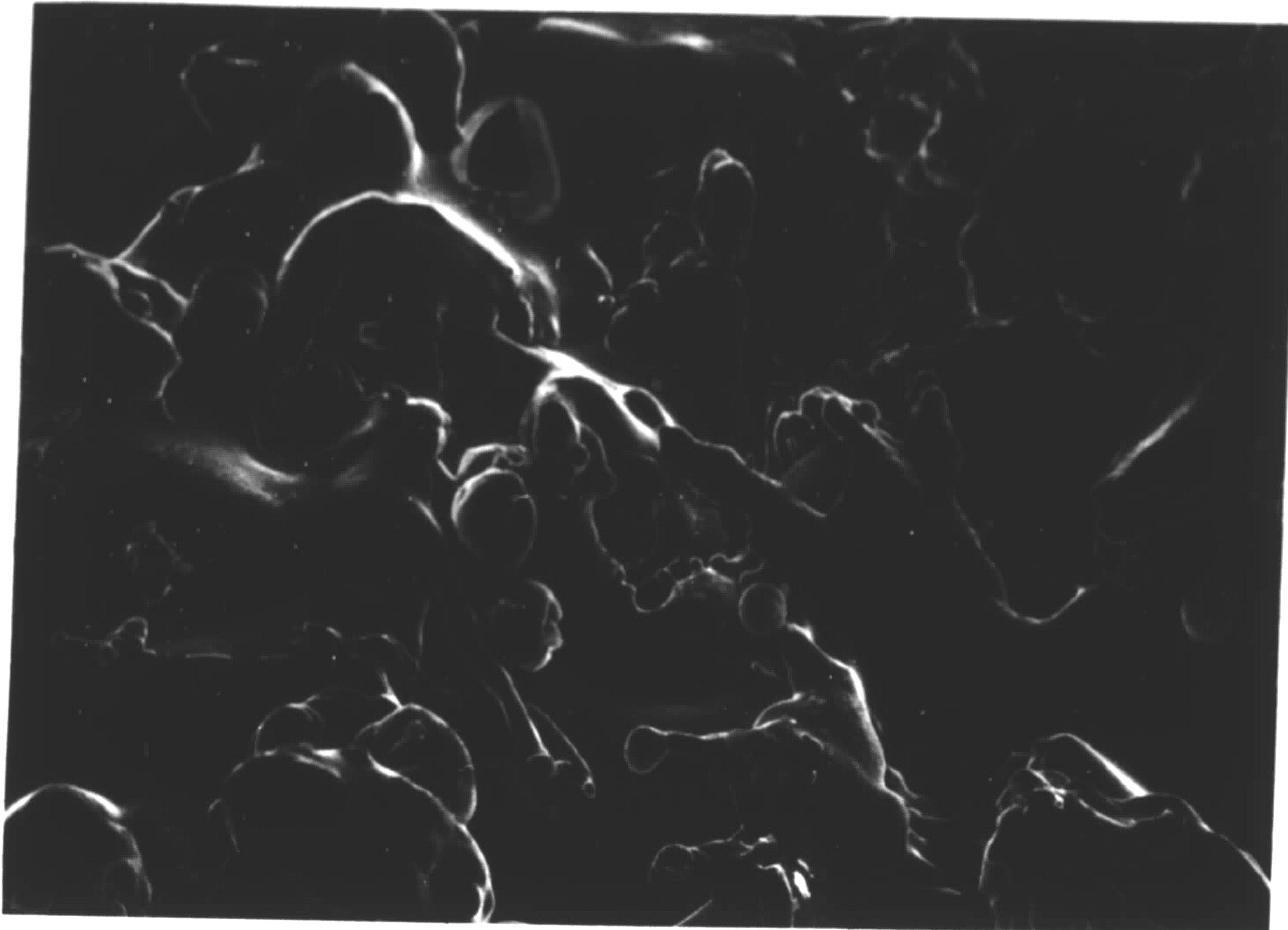

(b) sputtered, 500x, 40° tilt

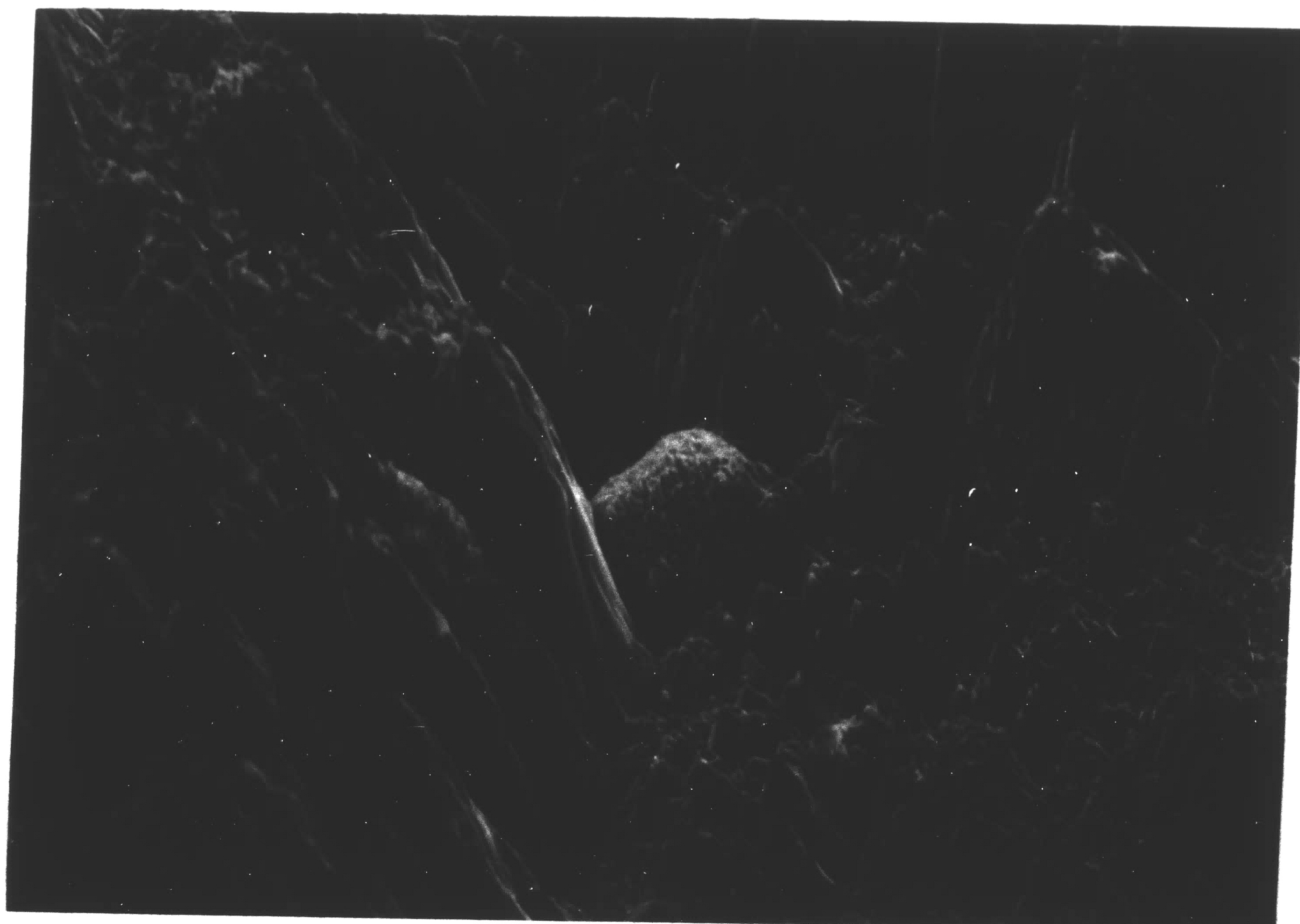

FIGURE 27

MICROSTRUCTURE OF NI-TA ALLOY TARGET
AS POLISHED AND CHEMICALLY ETCHED

(a) 400x

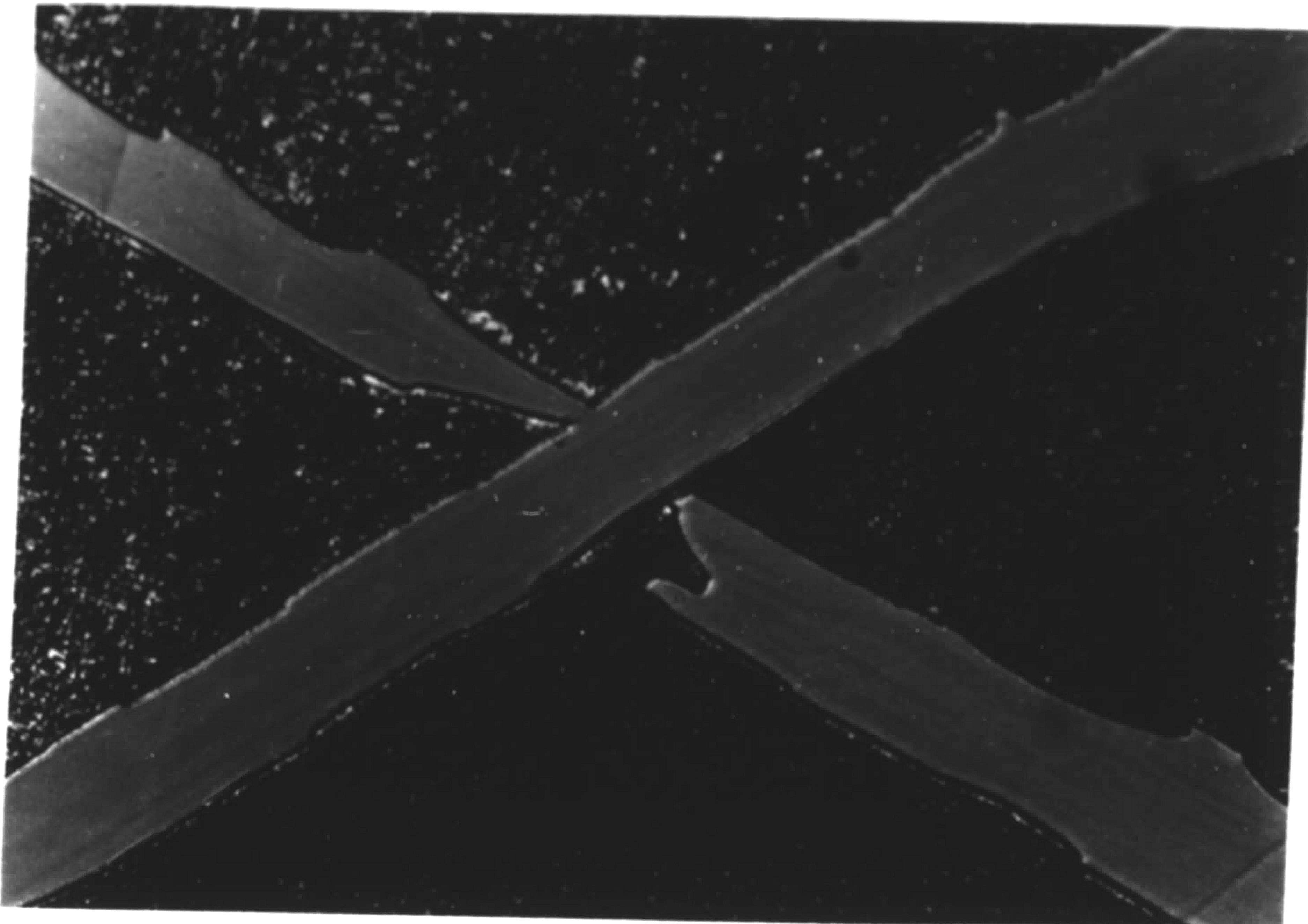

(b) 400x

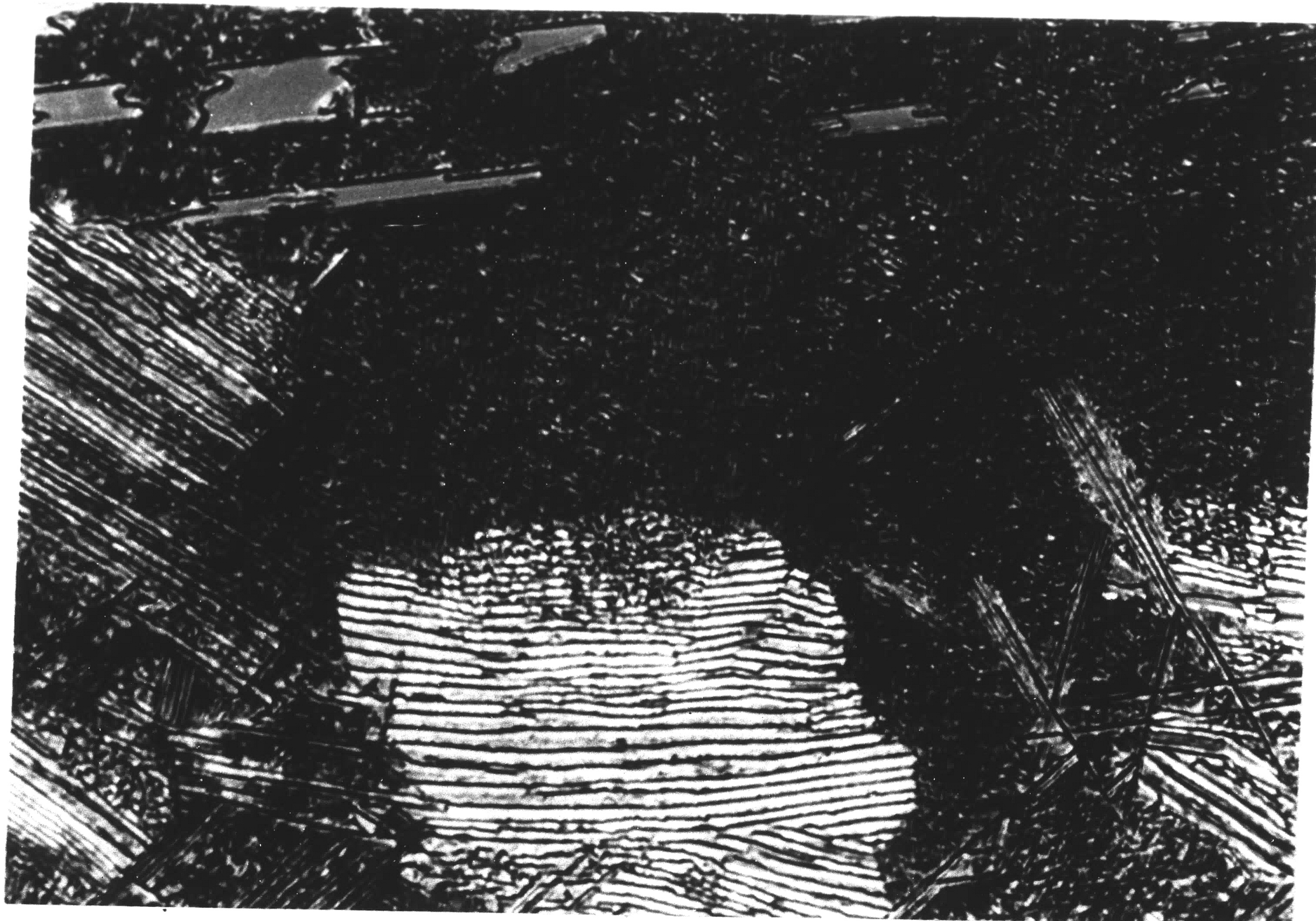

FIGURE 28

MICROSTRUCTURE OF FINE PRECIPITATE
MATRIX OF NI-TA ALLOY TARGET
AS POLISHED AND CHEMICALLY ETCHED

4000x

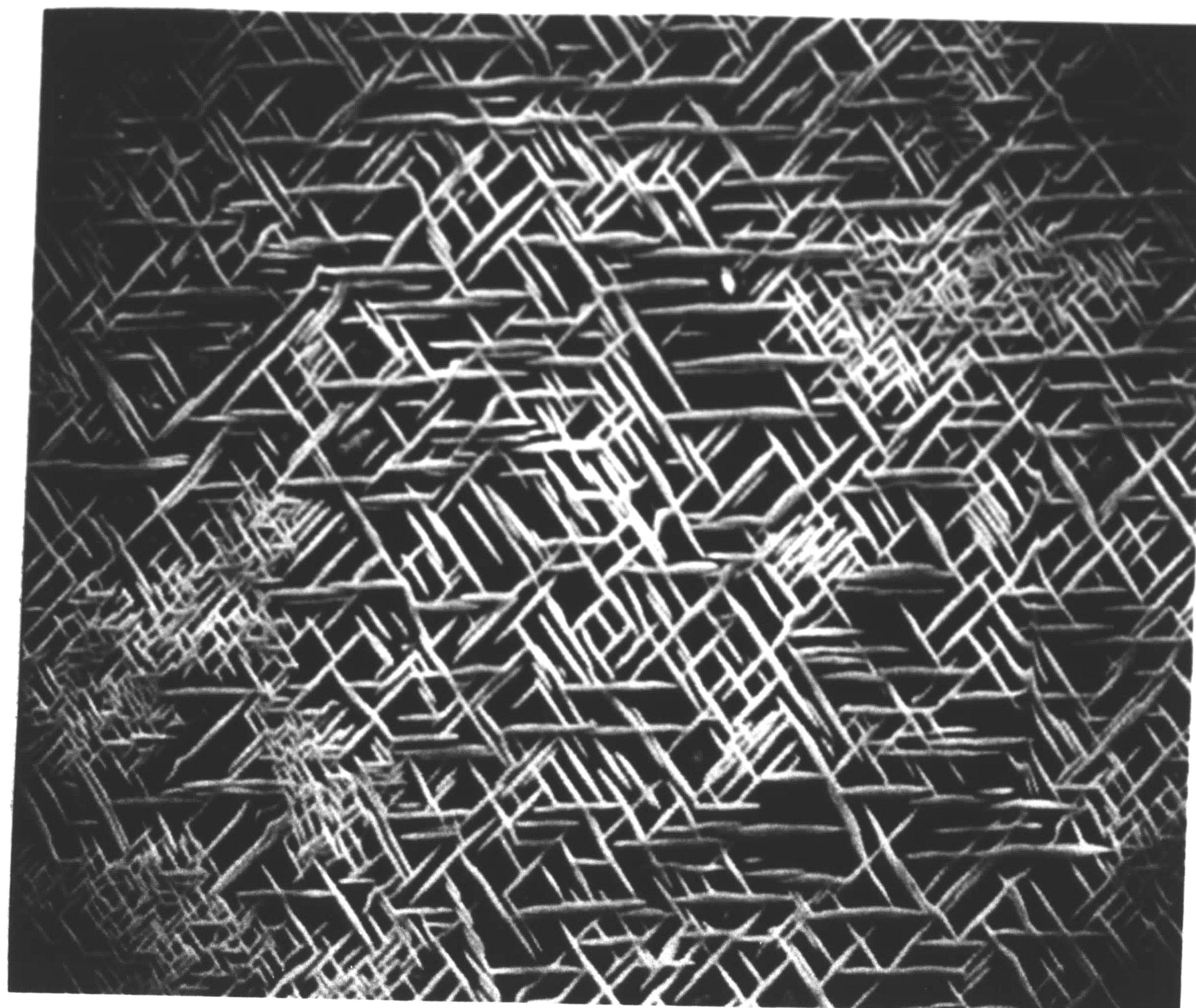

FIGURE 29

LOW MAGNIFICATION MICROGRAPH OF
SURFACE TOPOGRAPHY OF NI-TA
ALLOY TARGET AFTER SPUTTERING

400x

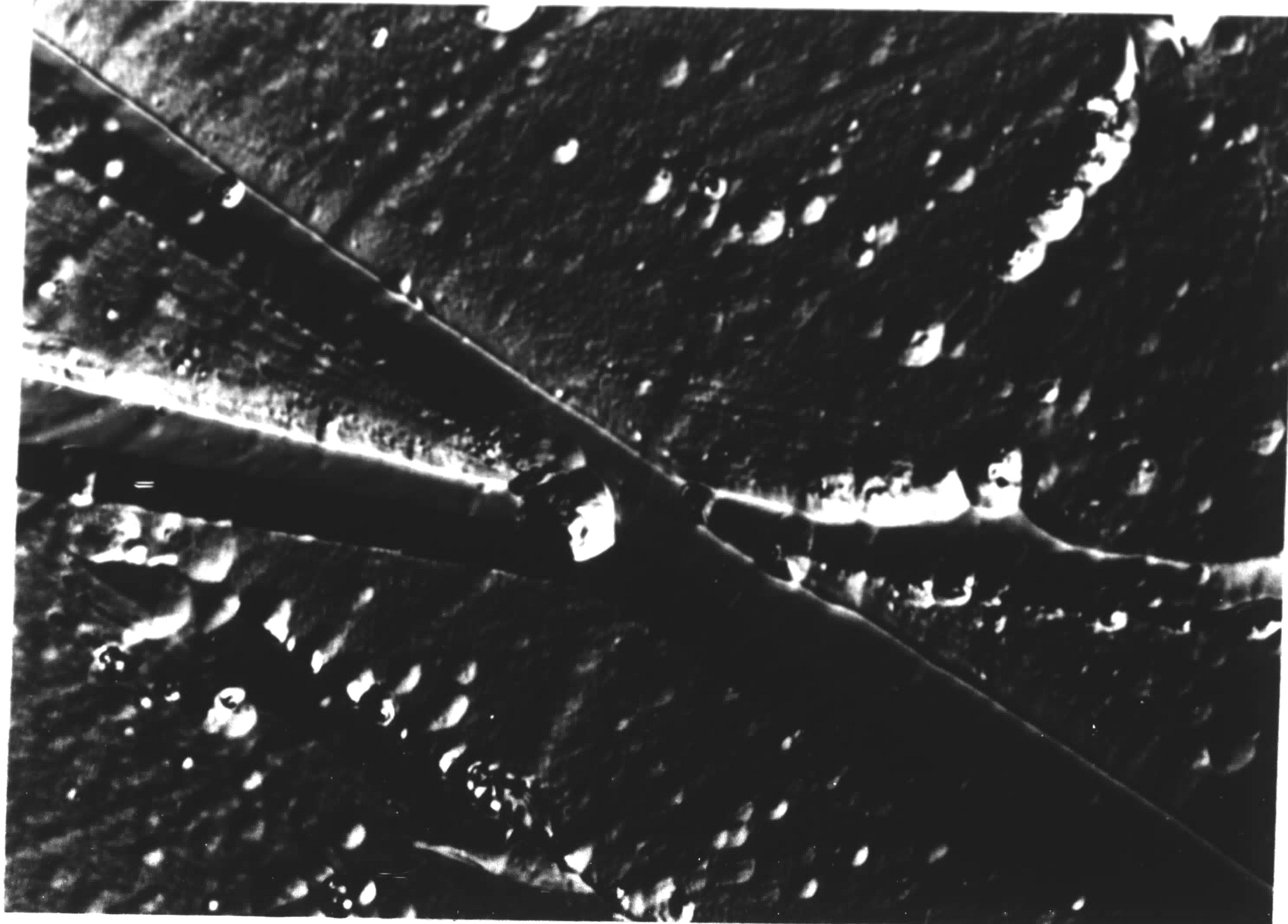

FIGURE 30

HIGH MAGNIFICATION MICROGRAPHS OF SURFACE TOPOGRAPHY OF NI-TA ALLOY TARGET AFTER SPUTTERING

(a) 800x

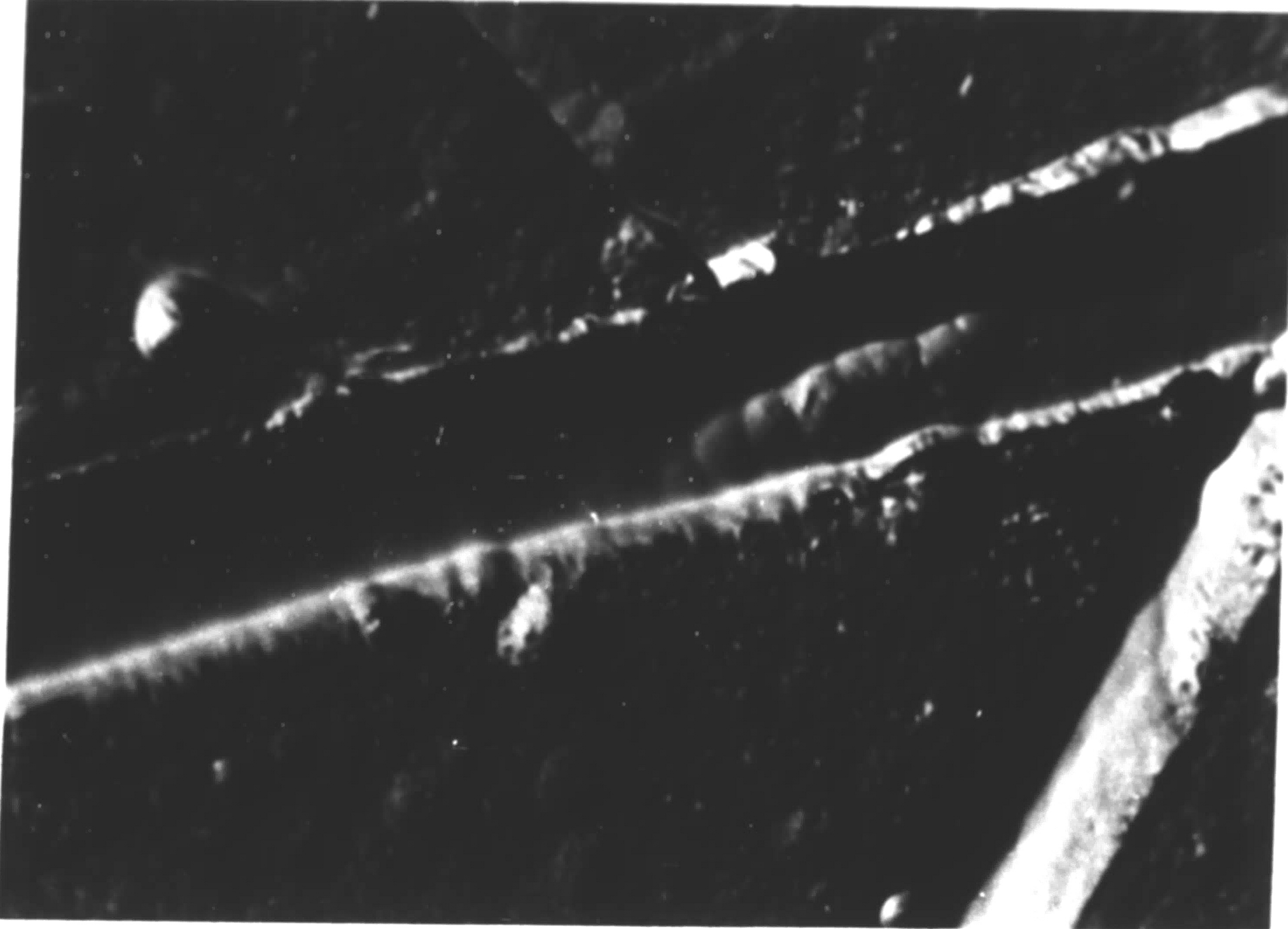

(b) 800x

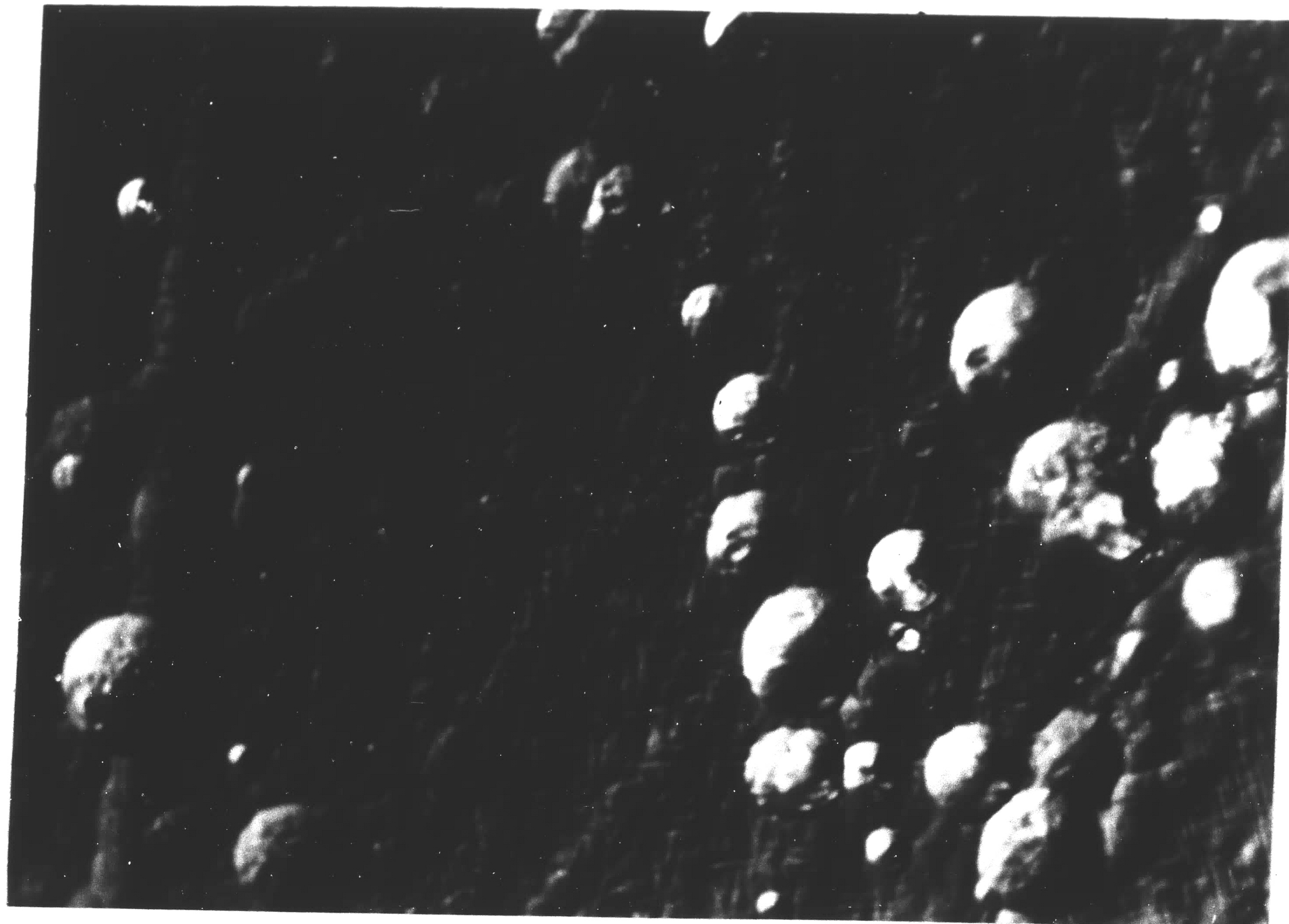

FIGURE 31

MICROGRAPH OF AS-SPUTTERED STRUCTURE
OF PURE ALUMINUM THIN FILM

Run # 17
Target: pure Al
Film: pure Al
750 Å thick, 46,400x

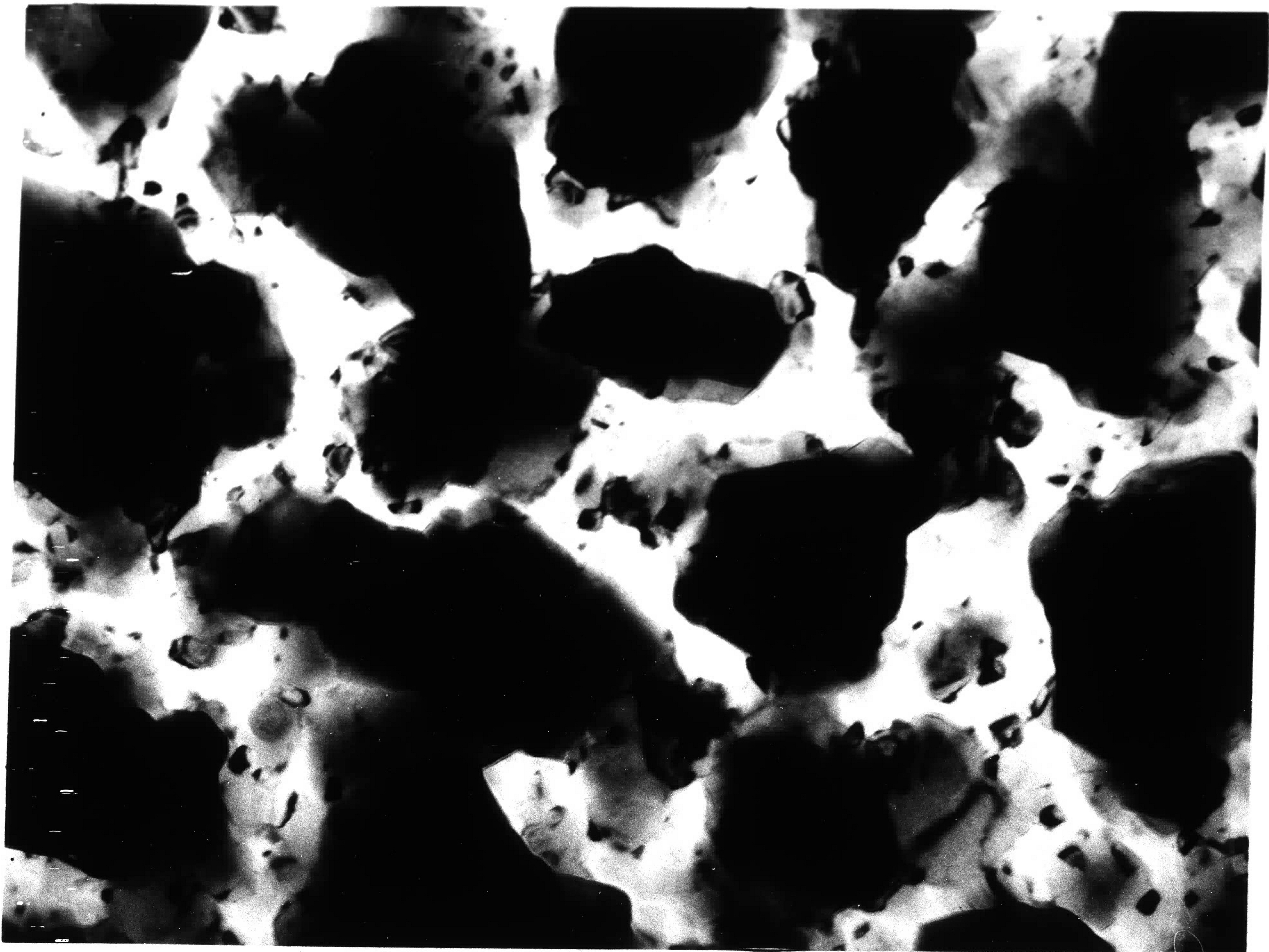

FIGURE 32

MICROGRAPH OF AS-SPUTTERED STRUCTURE
OF PURE NICKEL THIN FILM

Run #18
Target: pure Ni
Film: pure Ni
300 Å thick, 71,500x

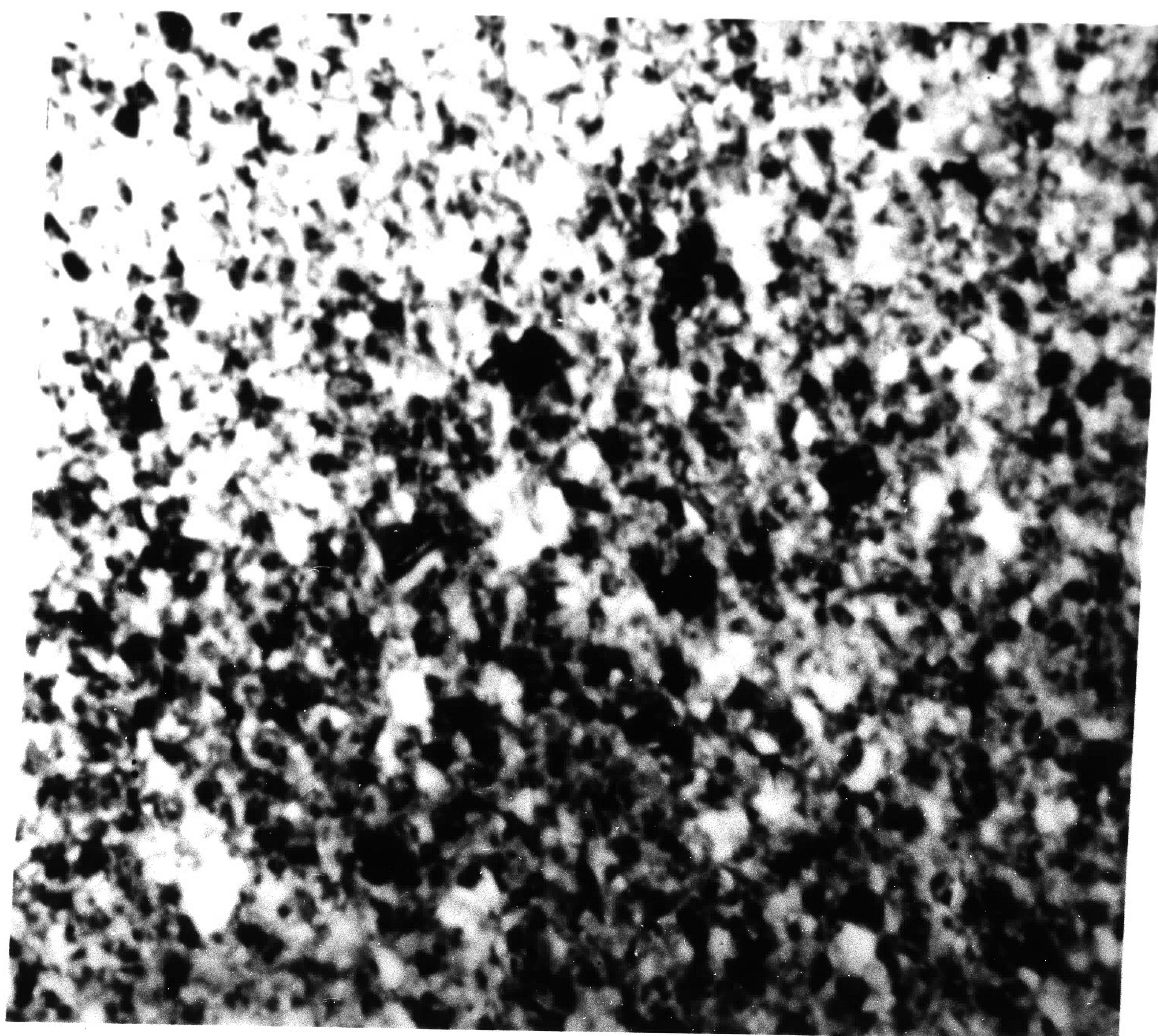

FIGURE 33

MICROGRAPHS OF AS-SPUTTERED STRUCTURE
OF TWO NI - 1.46AL THIN FILMS

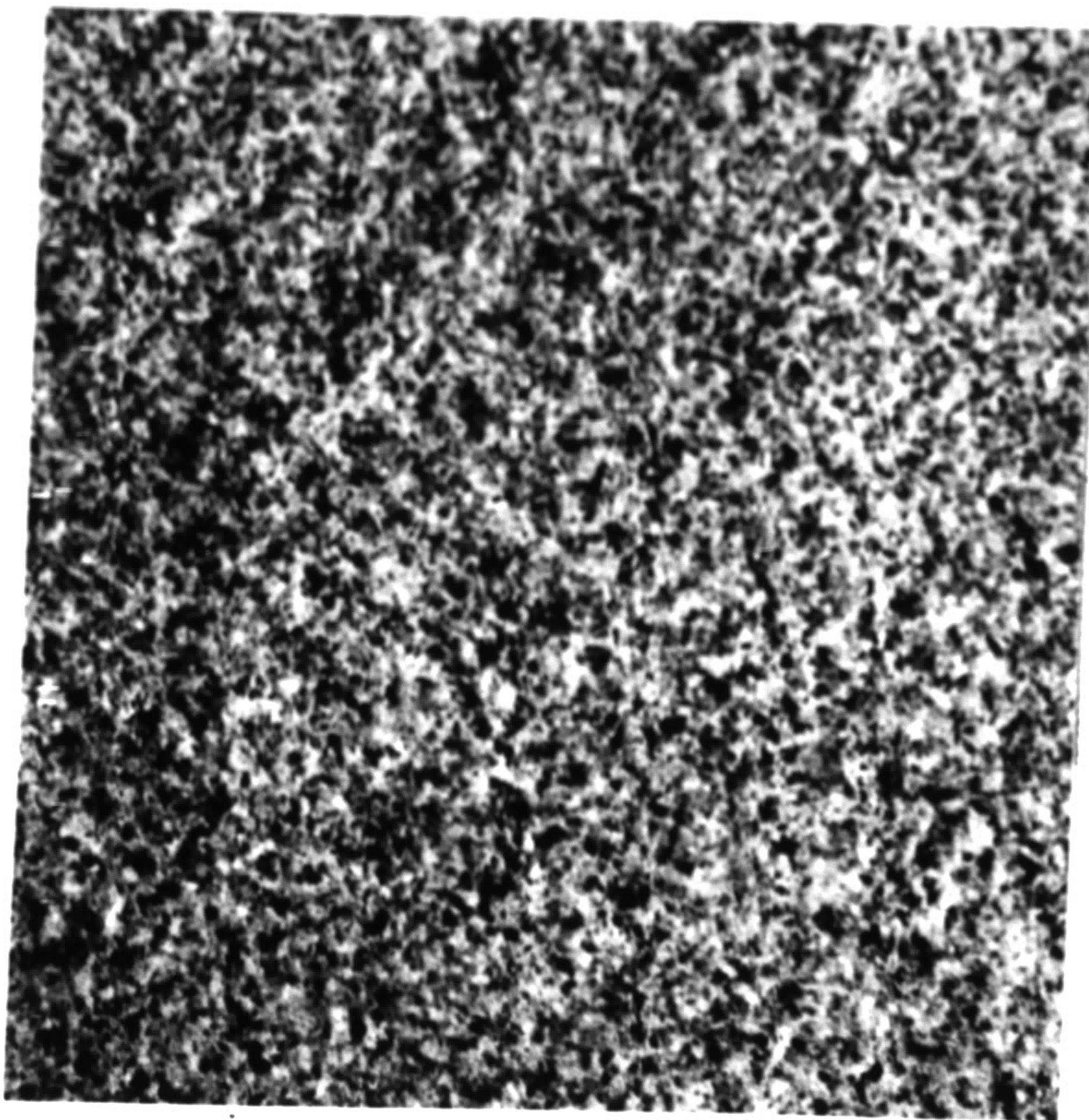

(a)
Run #22
Target: Ni - 6.8Al plasma sprayed
Film: 98.54Ni - 1.46Al
300 Å thick, 71,500x

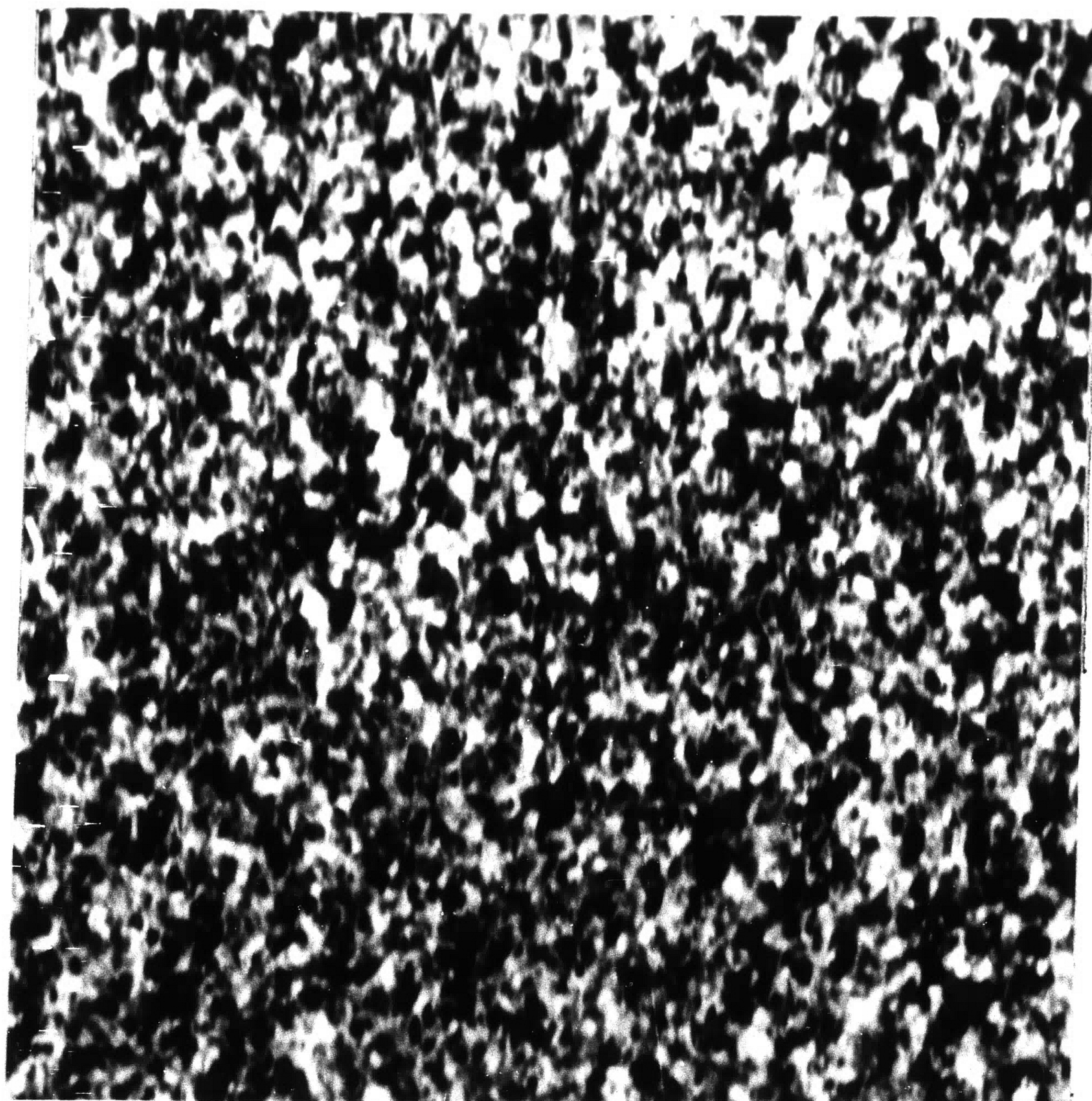

(b)
Run #24
Target: Ni - 6.8Al plasma sprayed
Film: 98.54Ni - 1.46Al
600 Å thick, 71,500x

FIGURE 34

STRUCTURE AND SELECTED AREA DIFFRACTION PATTERN OF AS-SPUTTERED NI - 3.95AL THIN FILM

Run #91
Target: 93.1Ni - 6.9Al alloy
Film: 96.05Ni - 3.95Al
600 Å thick, 176,000x

(a)

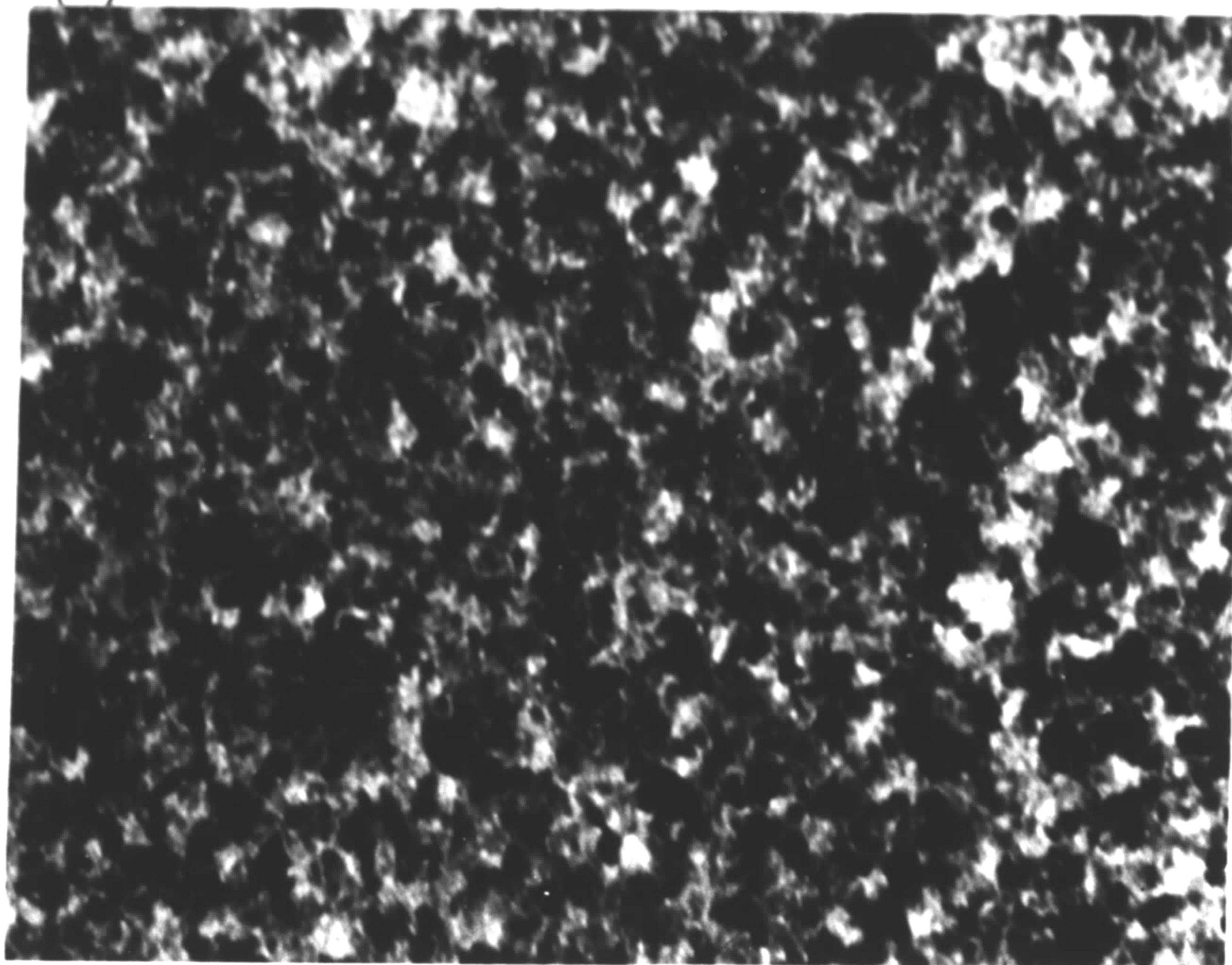

(b)

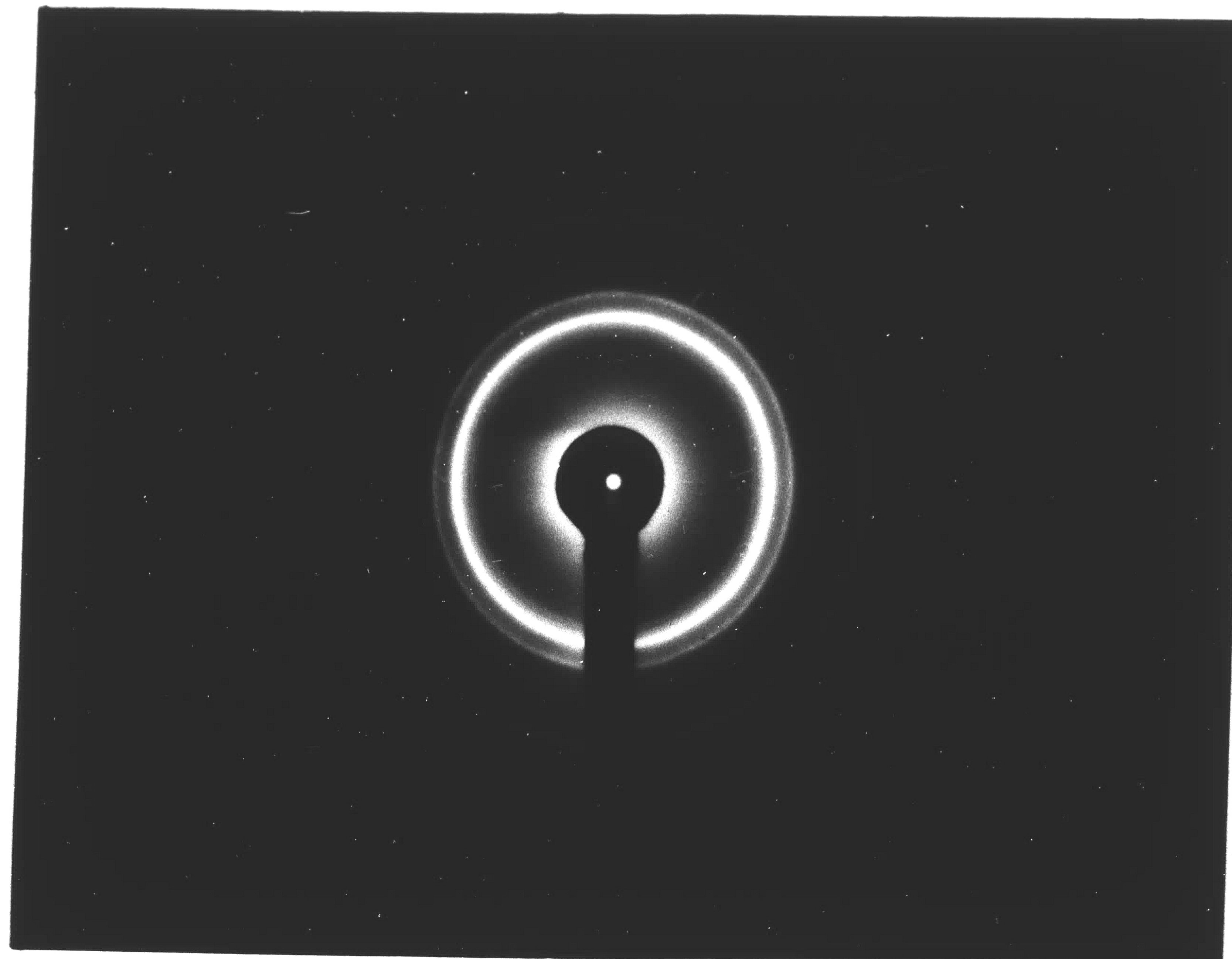

FIGURE 35

STRUCTURE AND SELECTED AREA DIFFRACTION
PATTERN OF AS-SPUTTERED NI - 36.7TA THIN FILM

Run #92
Target: 65.2Ni - 34.8Ta alloy
Film: 54.4Ni - 36.7Ta - Ar
500 Å thick, 108,800x

(a)

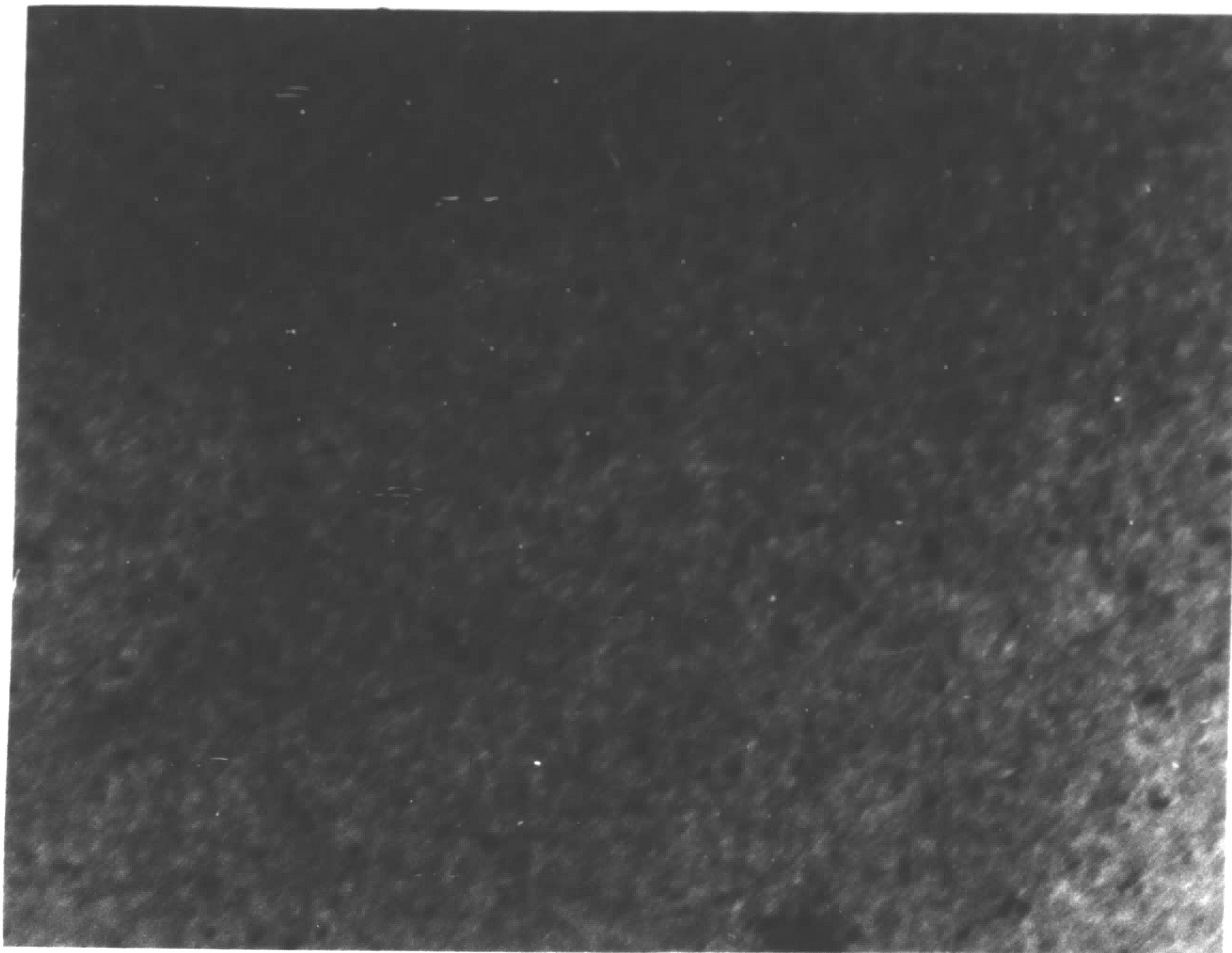

(b)

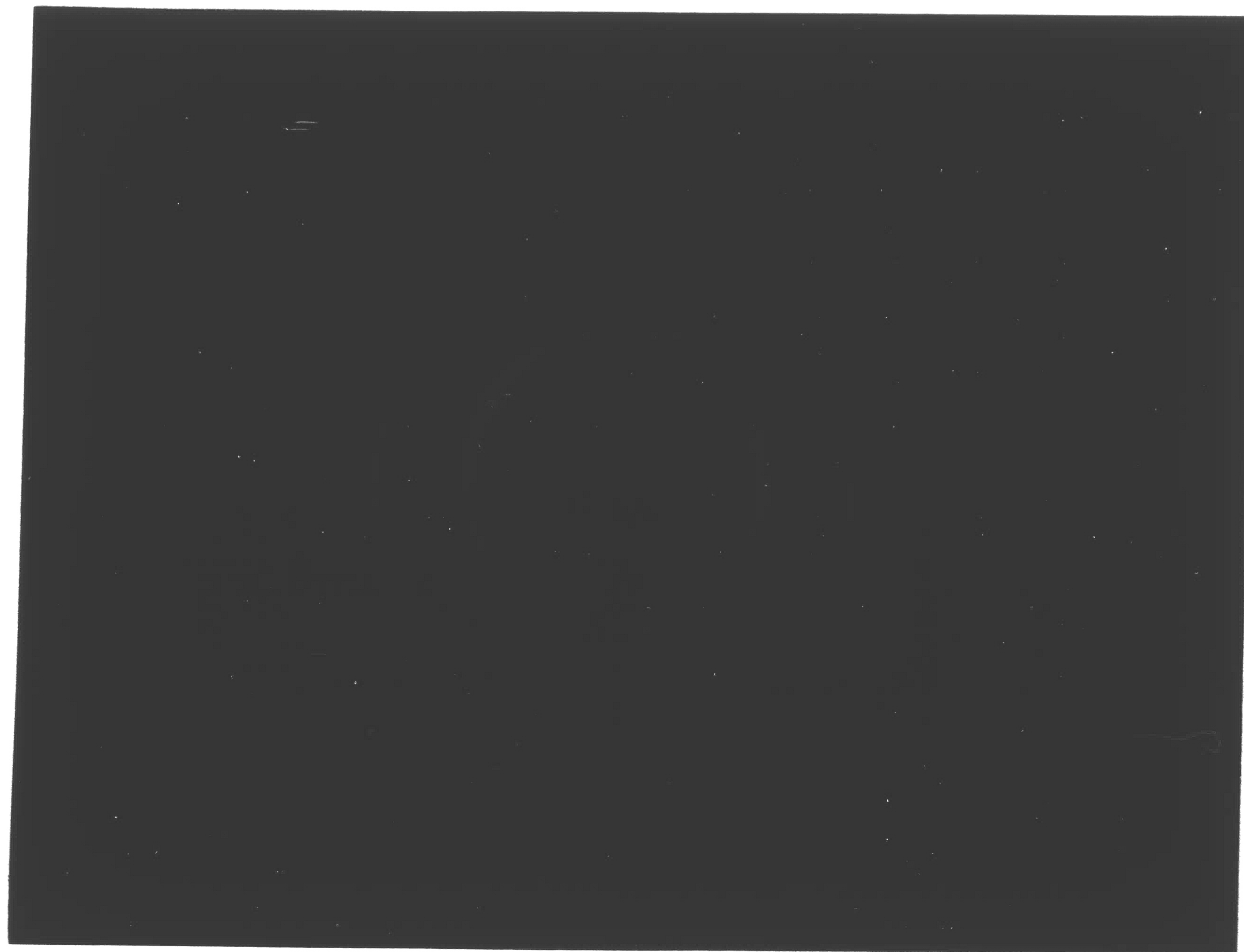

FIGURE 36

SELECTED AREA DIFFRACTION PATTERN SHOWING TEXTURE OF NI - 36.7TA THIN FILM ON TILTING

Run #92
Target: 65.2Ni - 34.8Ta alloy
Film: 54.4Ni - 36.7Ta - Ar
500 Å thick

(a) +19 specimen tilt

(b) -6.5 specimen tilt

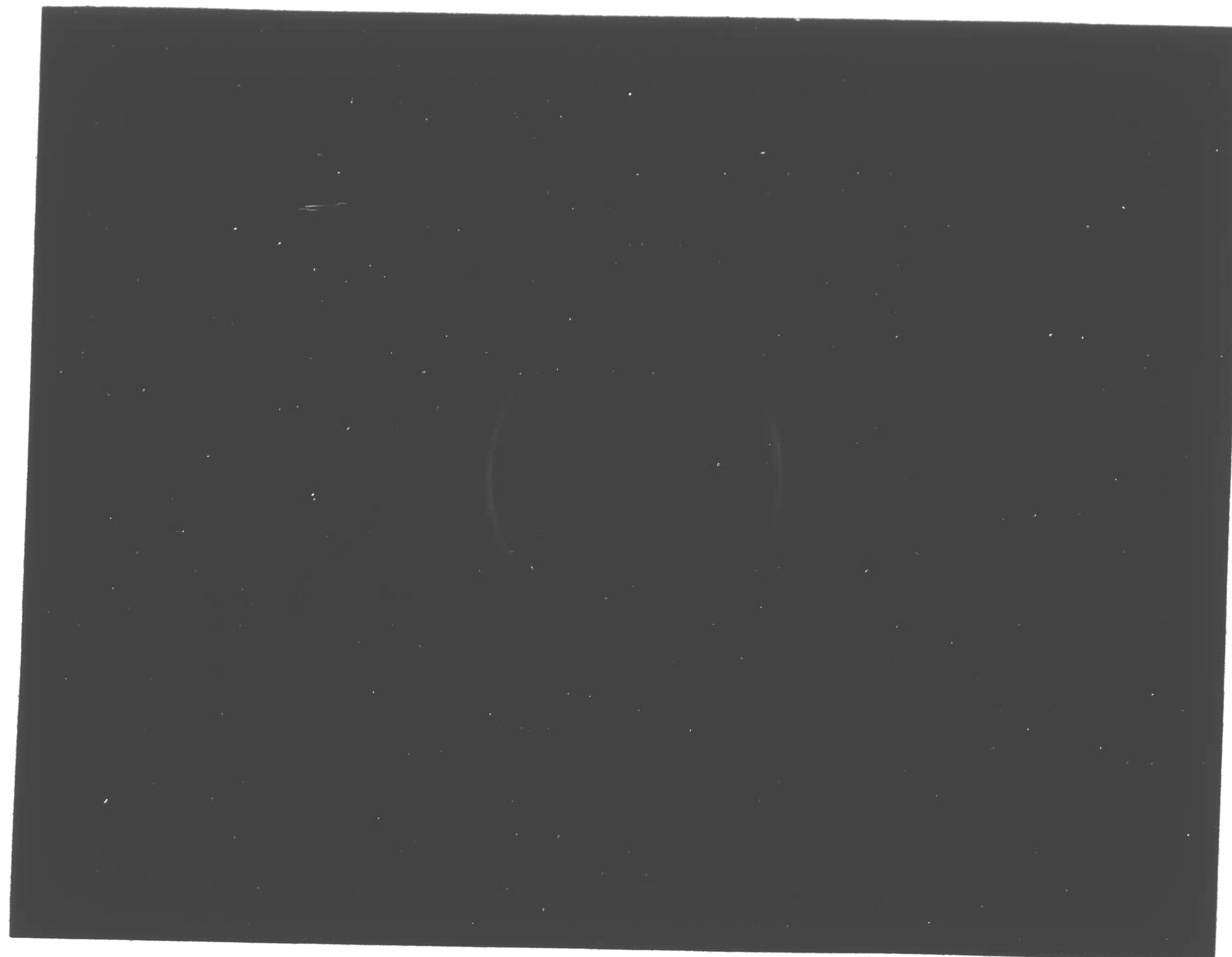

FIGURE 37

LOW MAGNIFICATION MICROGRAPH
OF FILM BREAK UP ON HEATING

Run #24
Target: 93.2Ni - 6.8Al plasma sprayed
Film: 98.54Ni - 1.46Al
600 Å thick, 5100x, 575°C

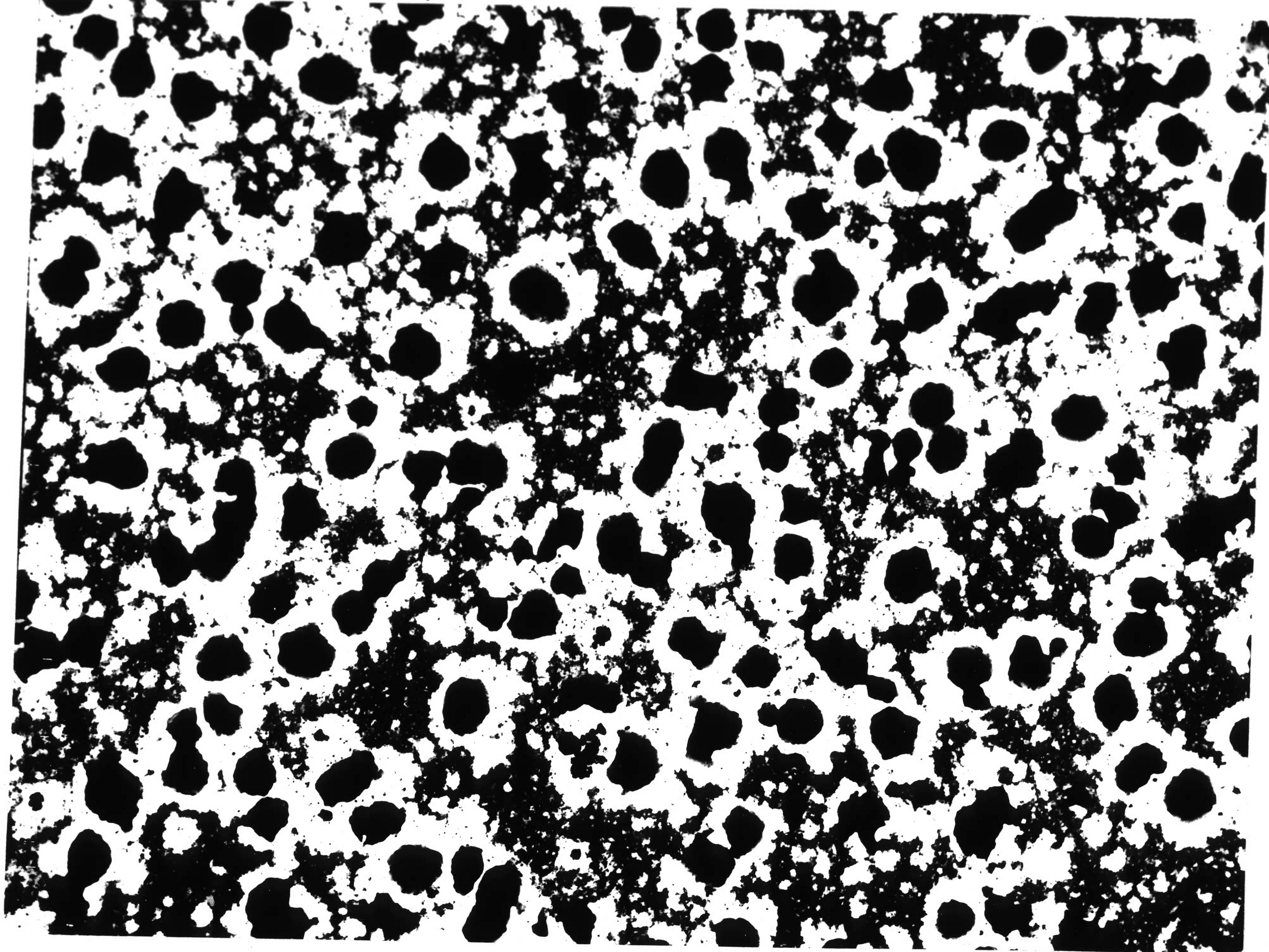

FIGURE 38

HIGH MAGNIFICATION MICROGRAPH
OF AGGLOMERATED STRUCTURE

Run #24
Target: 93.2Ni - 6.8Al plasma sprayed
Film: 98.54Ni - 1.46Al
600 Å thick, 44,800x, 575°C

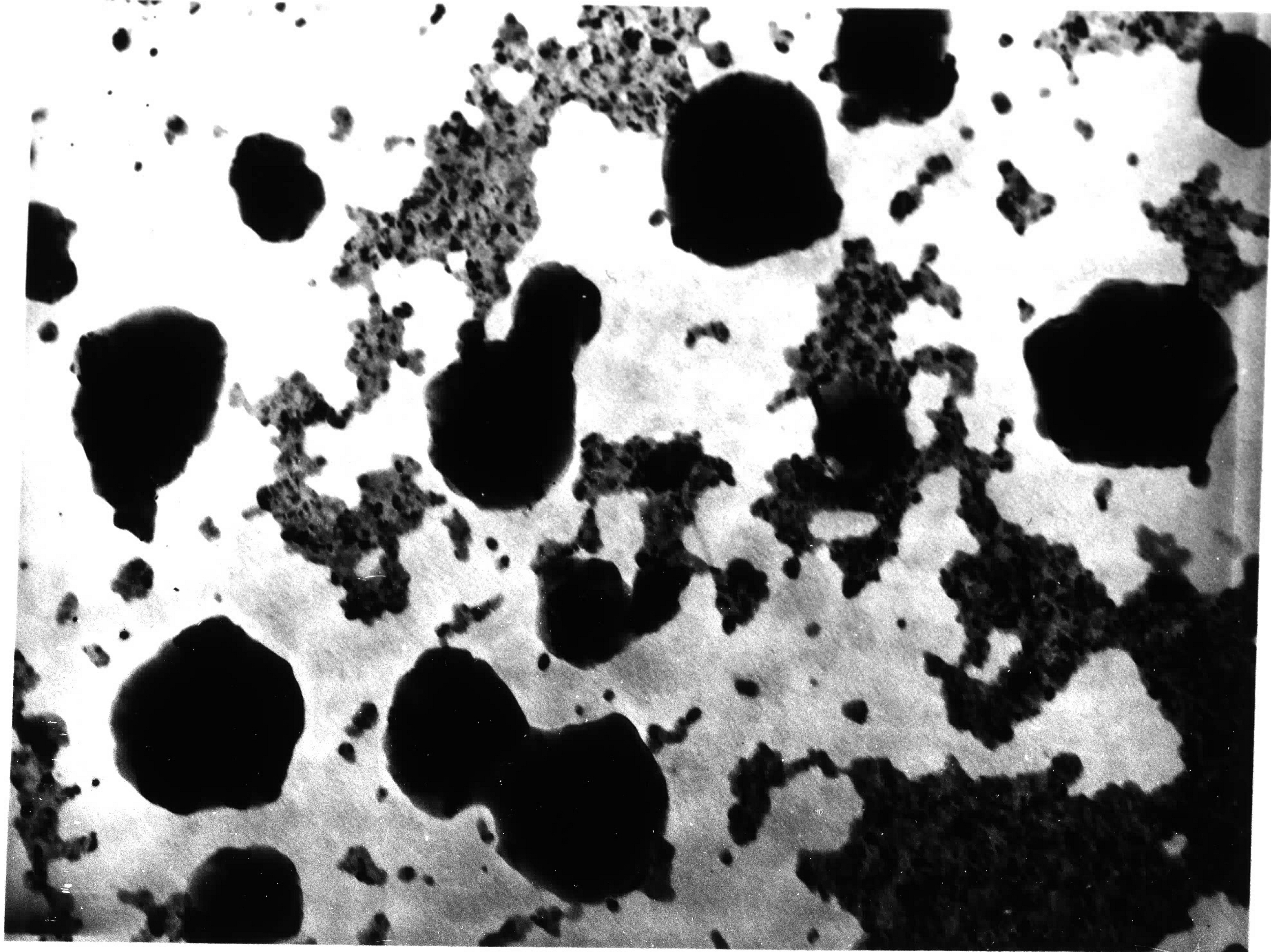

FIGURE 39

MICROGRAPH OF IRREGULAR
FILM BREAK UP PATTERN

Run #24
Target: 93.2Ni - 6.8Al plasma sprayed
Film: 98.54Ni - 1.46Al
600 Å thick, 3140x, 460°C

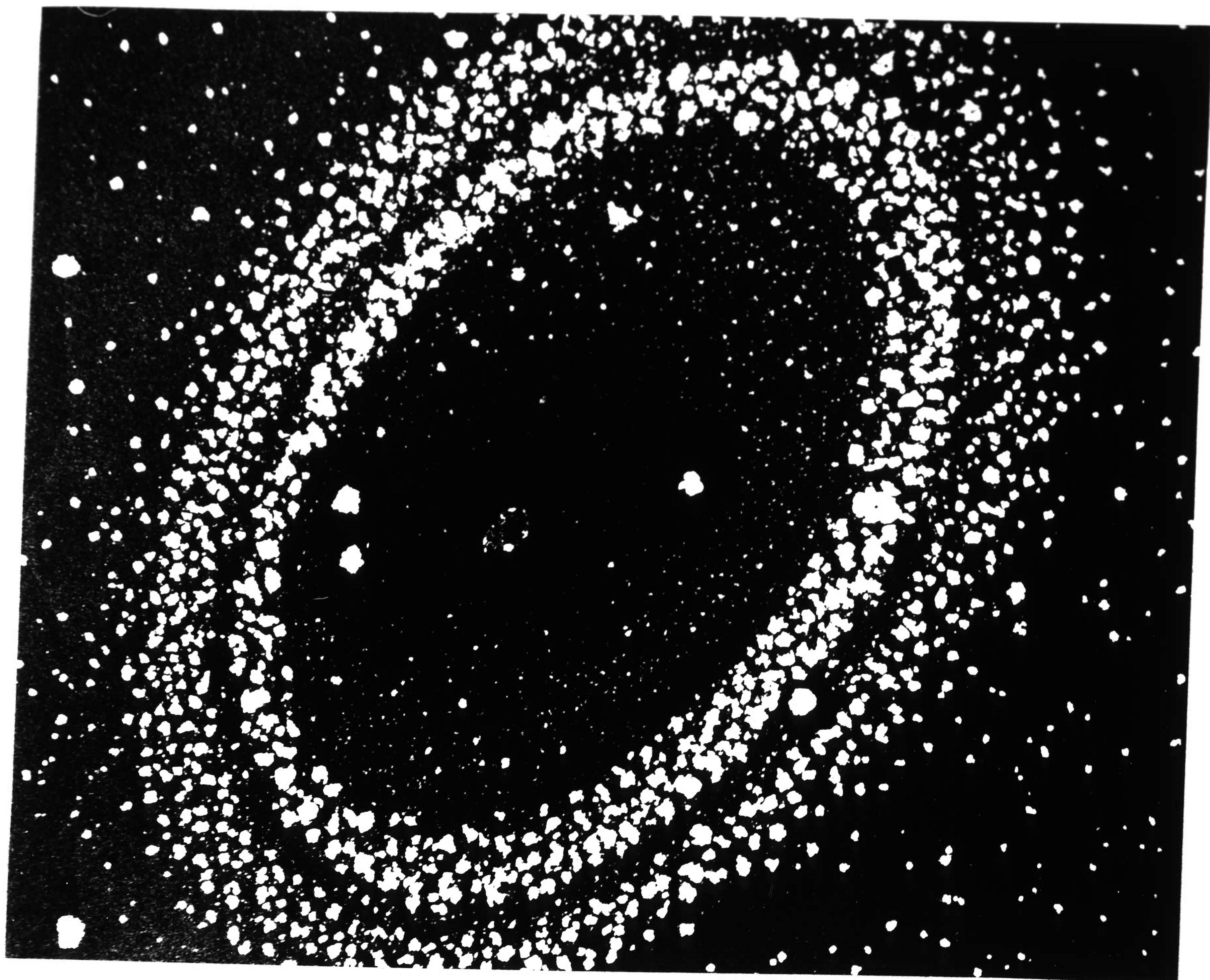

FIGURE 40

SELECTED AREA DIFFRACTION PATTERN
OF NI - 3.95AL THIN FILM AT 265°C

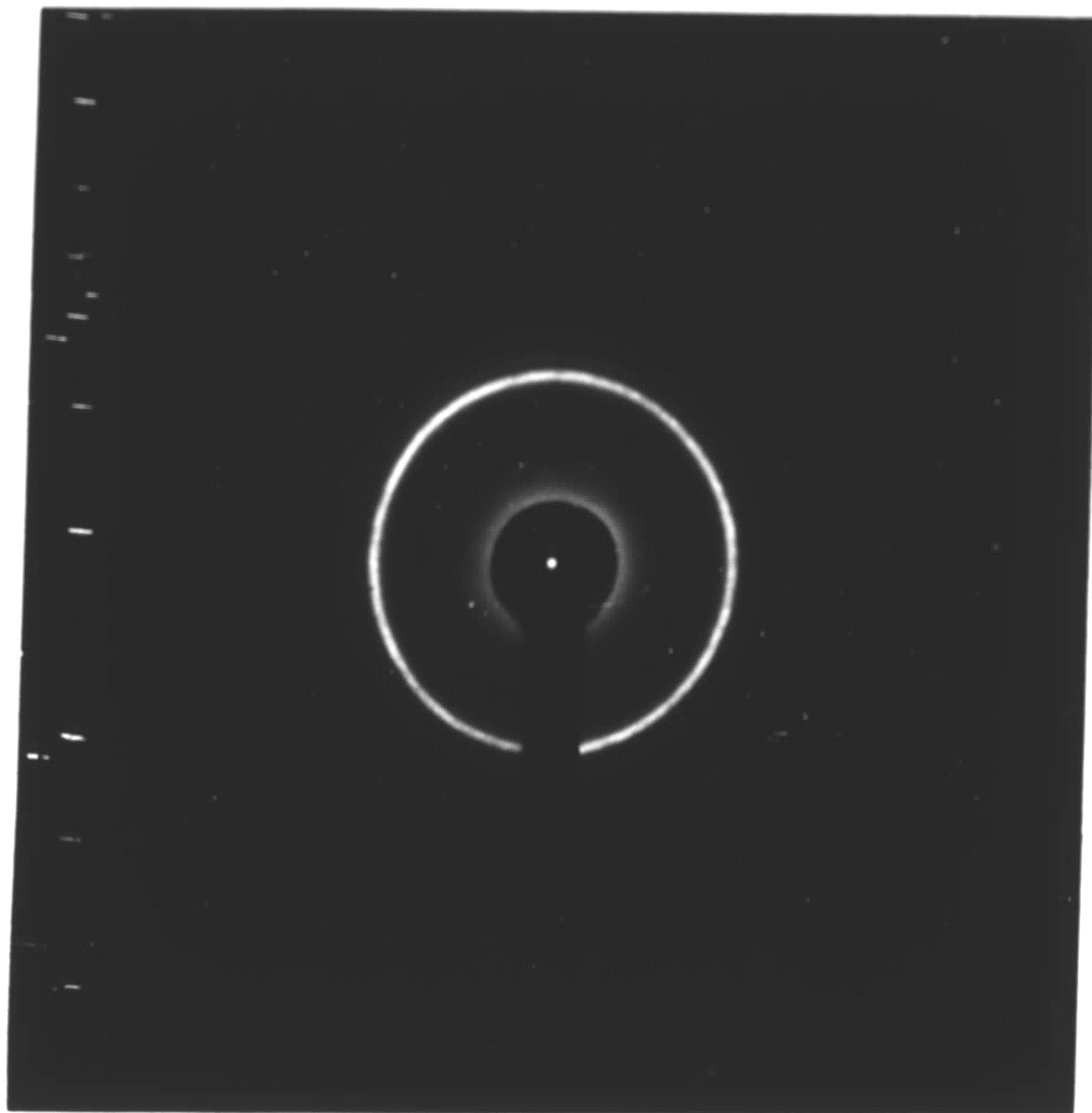

Run #91
Target: 93.1Ni - 6.9Al alloy
Film: 96.05Ni - 3.95Al
600 Å thick, 265°C

FIGURE 41

SELECTED AREA DIFFRACTION PATTERN
OF NI - 3.95AL THIN FILM AT 415°C

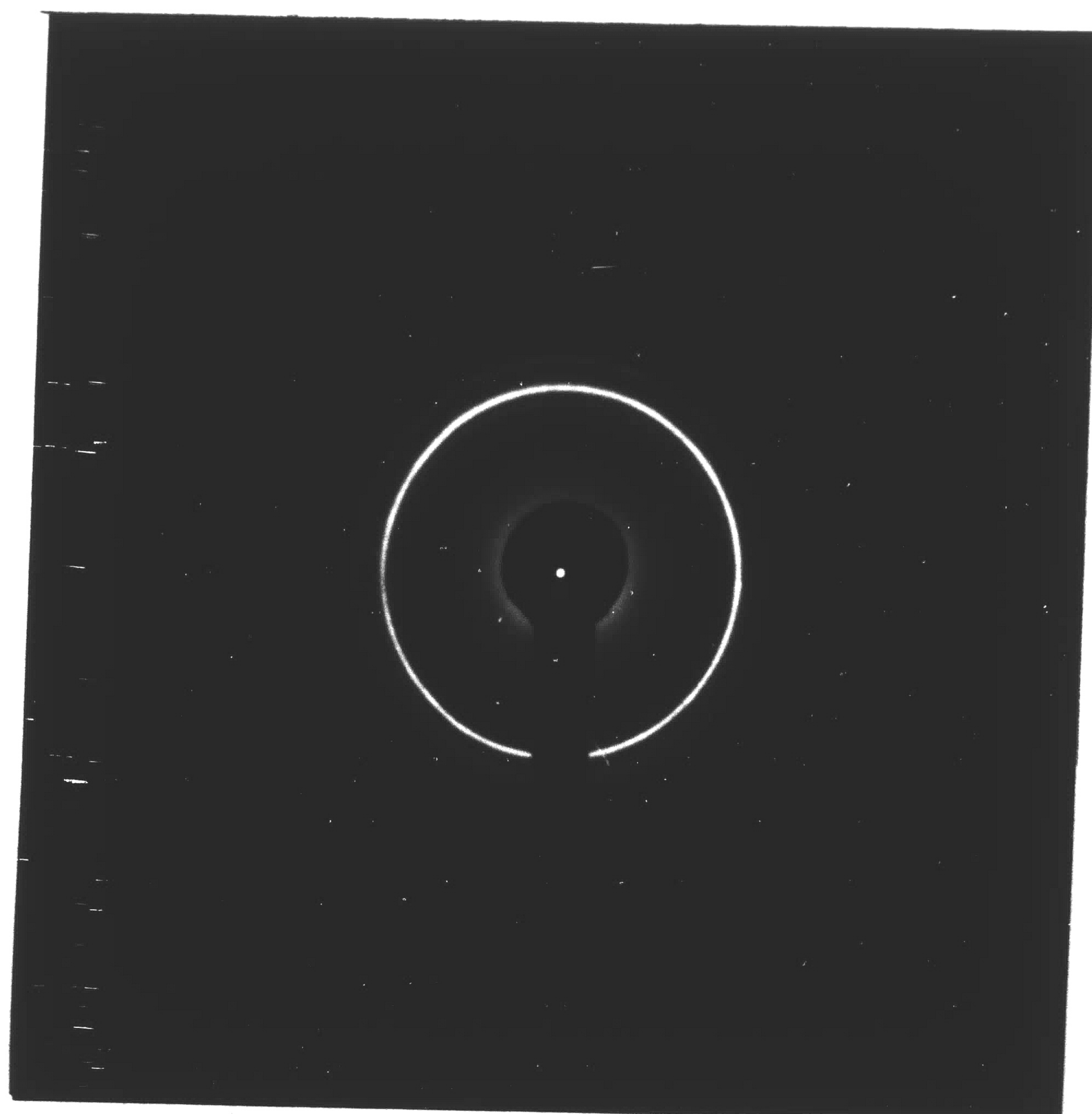

Run #91
Target: 93.1Ni - 6.9Al alloy
Film: 96.05Ni - 3.95Al
600 Å thick, 415°C

FIGURE 42

BRIGHT FIELD AND DARK FIELD MICROGRAPHS
OF NI - 3.95AL STRUCTURE AT 700°C

Run #91
Target: 93.1Ni - 6.9Al alloy
Film: 96.05Ni - 3.95Al
600 Å thick, 73,600x, 700°C

(a) Bright field

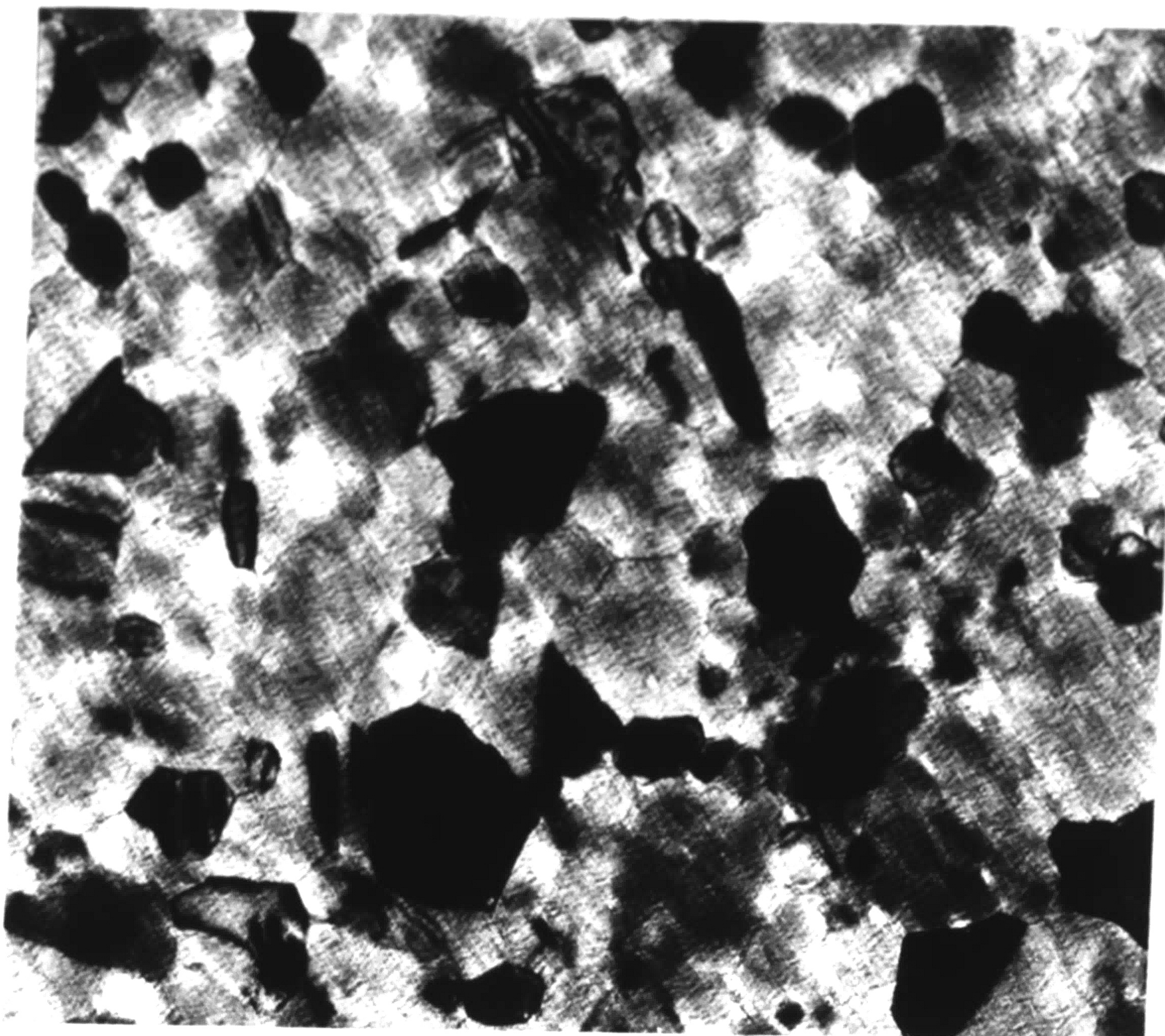

(b) Dark field

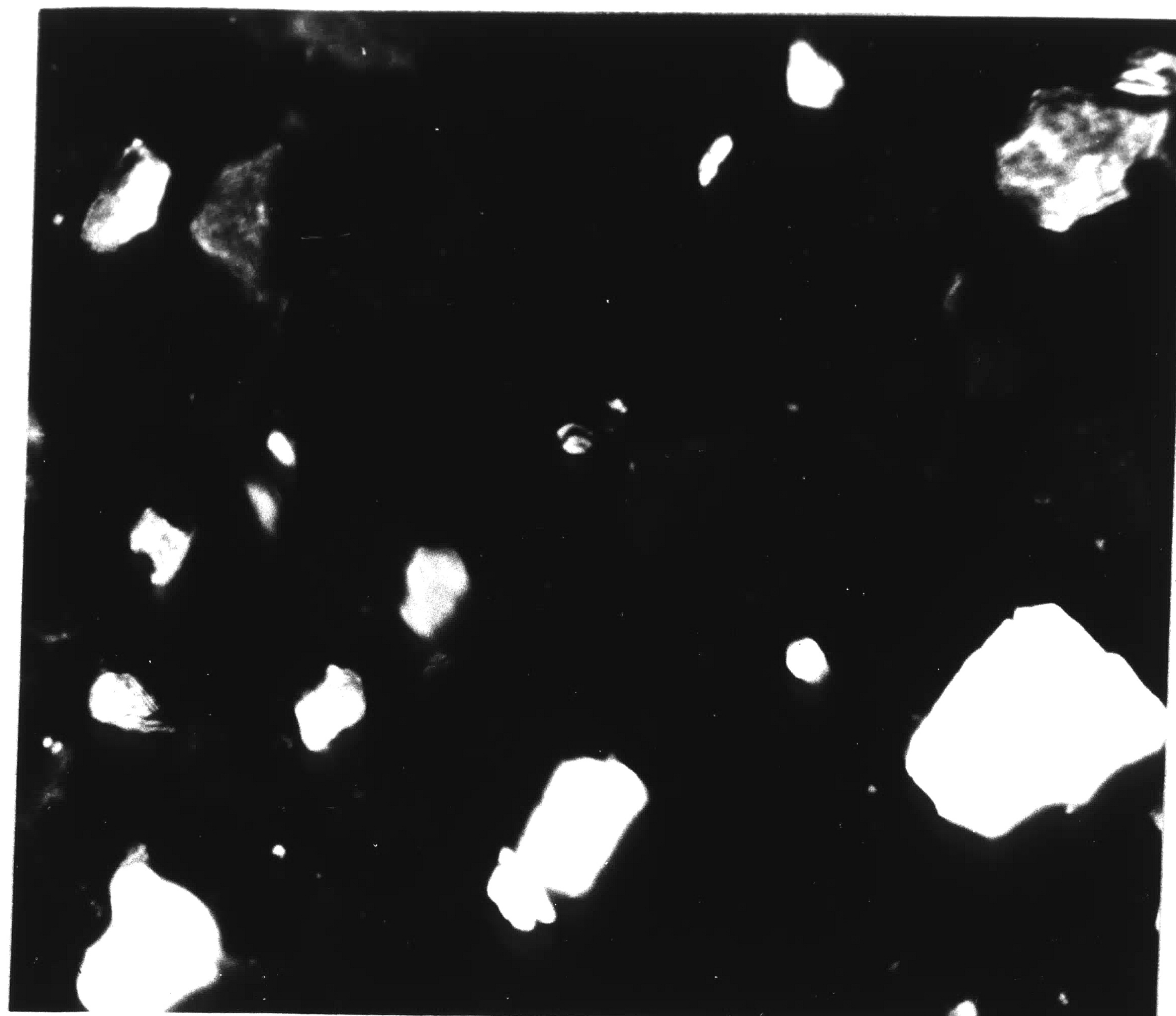

FIGURE 43

SELECTED AREA DIFFRACTION PATTERN
OF NI - 36.7TA THIN FILM AT 410°C

Run #92
Target: 65.2Ni - 34.8Ta alloy
Film: 54.4Ni - 36.7Ta - Ar
500 Å thick, 410°C

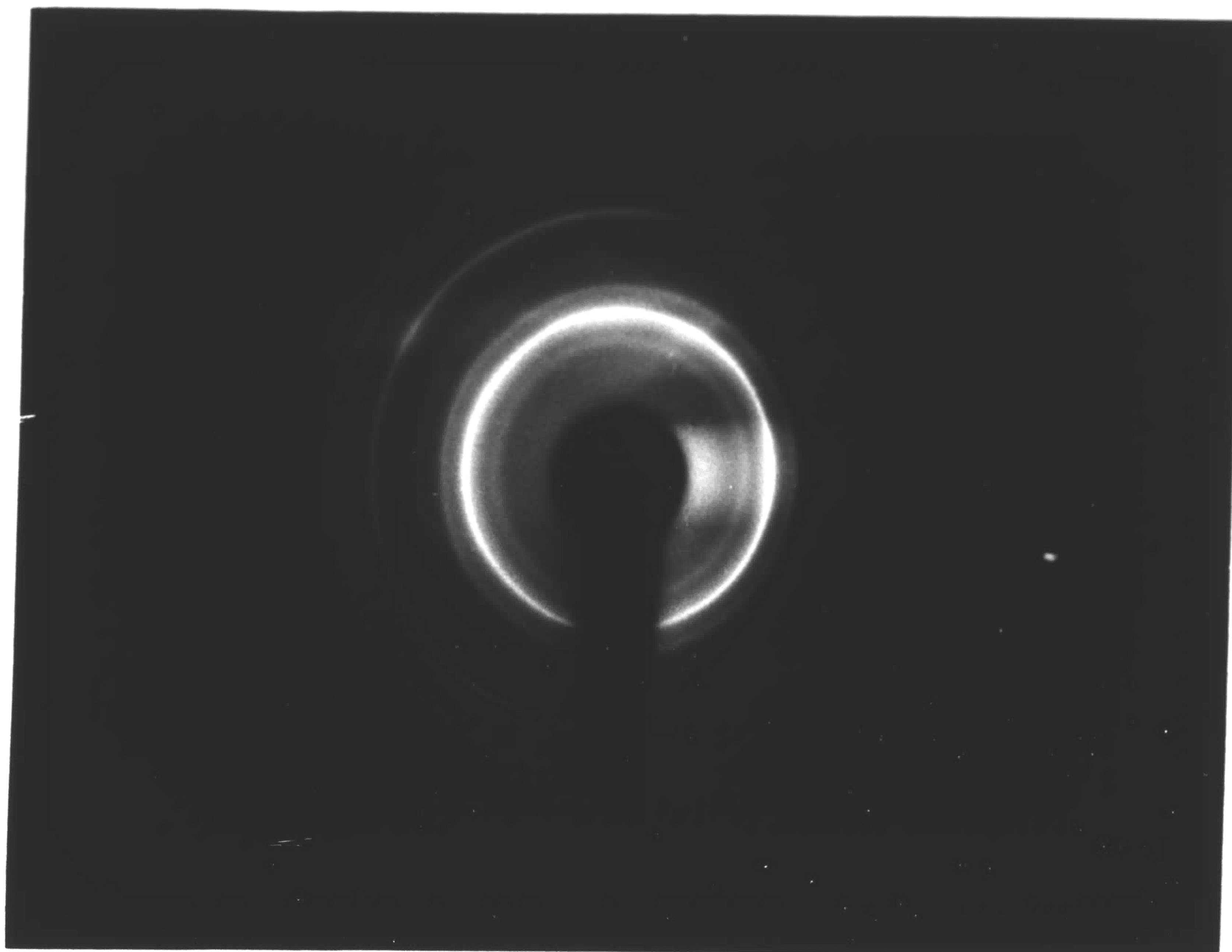

FIGURE 44

STRUCTURE AND SELECTED AREA DIFFRACTION PATTERN OF NI - 36.7TA THIN FILM AT 900°C

Run #92
Target: 65.2Ni - 34.8Ta alloy
Film: 54.4Ni - 36.7Ta - Ar
500 Å thick, 73,600x, 900°C

(a)

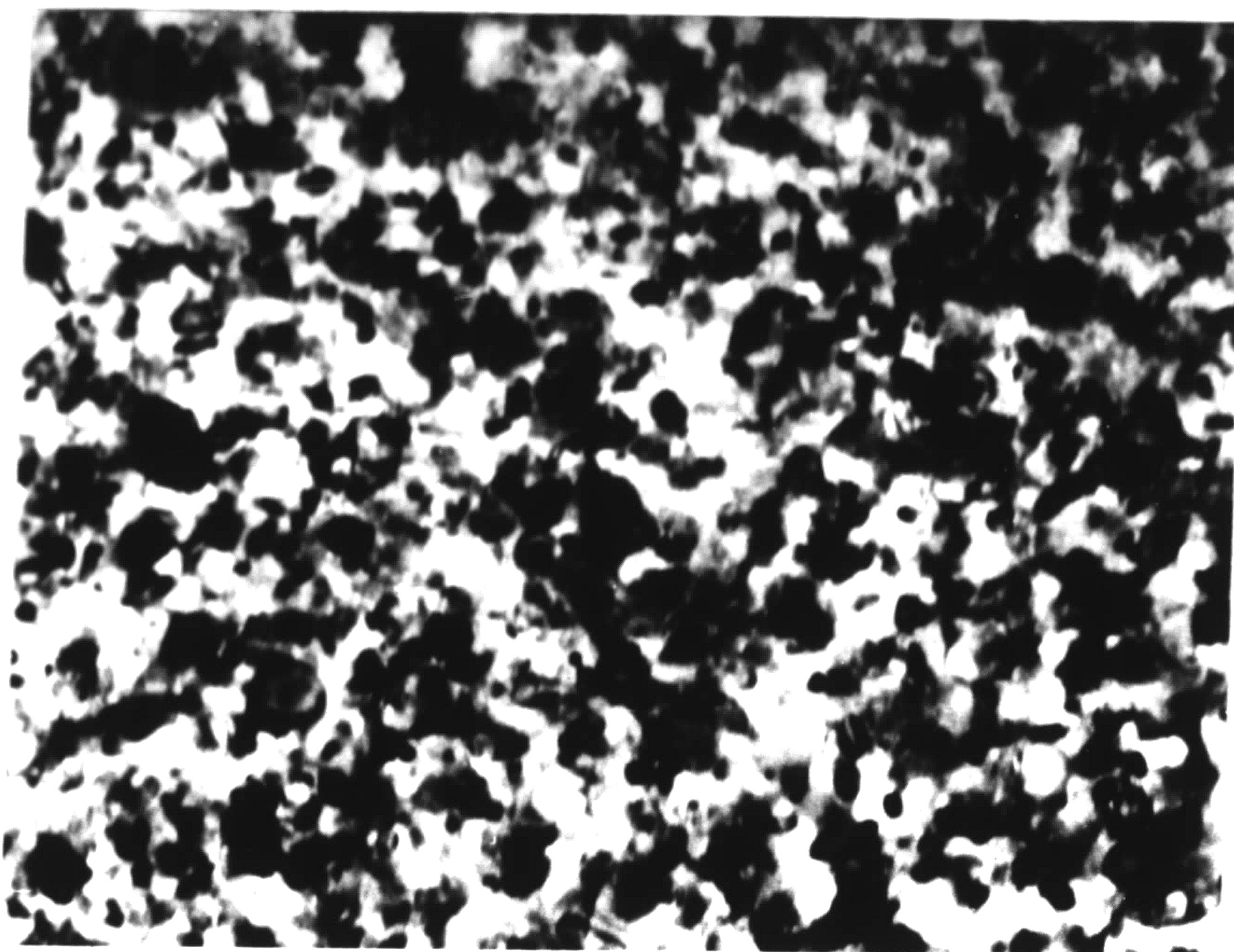

(b)

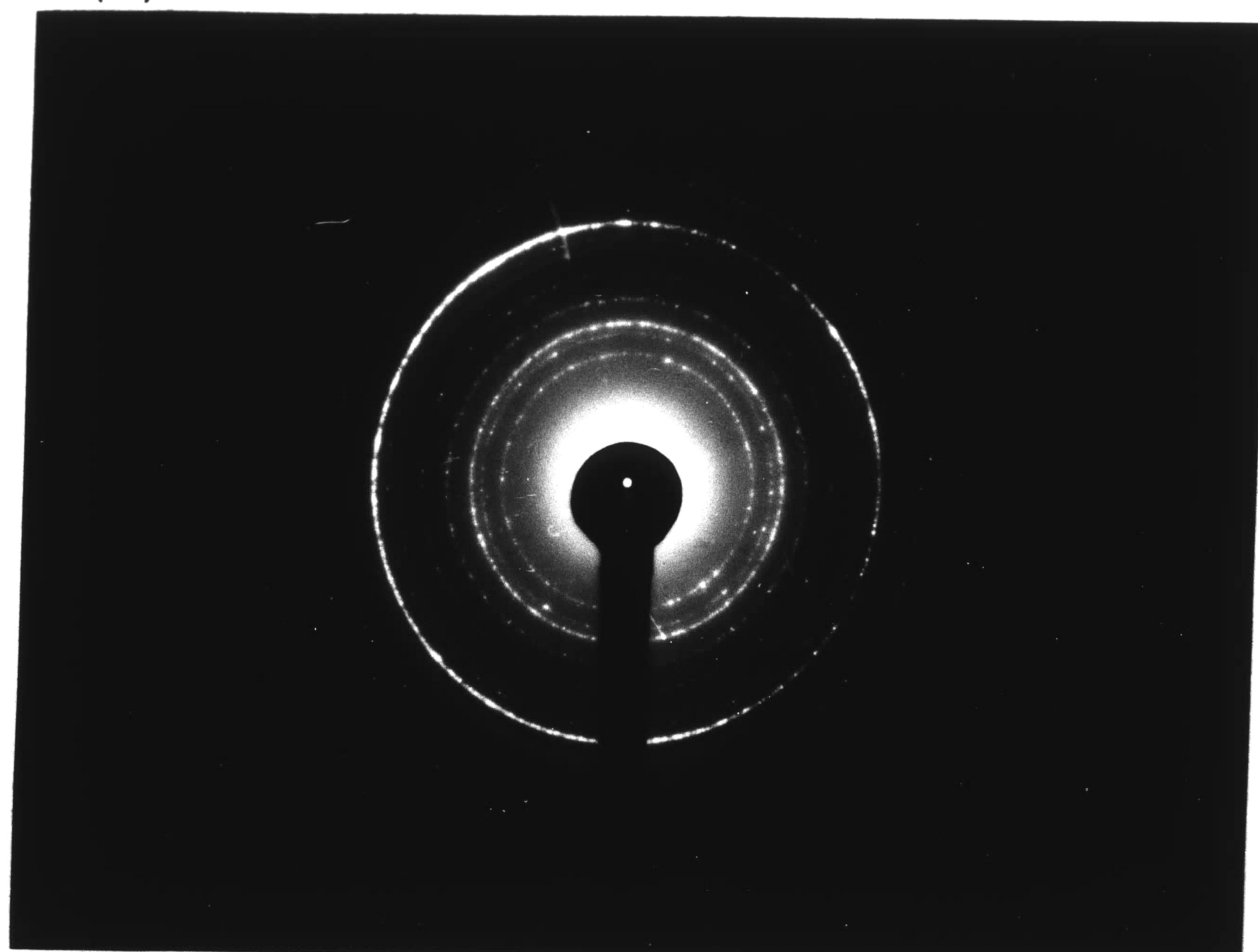

APPENDIX I

Description of the Three Stages for Sputtering

Pre-sputtering Stage (≈12 hours)

(1) Break vacuum with nitrogen.

(2) Screw selected target(s) to upper electrode(s) and place either aluminum foil or a sheet of annealed copper between target and electrode to assure thermal contact.

(3) Place substrate(s) on substrate holder table.

(4) Pump chamber and gas lines to $\approx 5 * 10^{-7}$ torr.

Sputtering Stage (1/2 hour + deposition time)

(5) Water cool target and substrate, backfill gas lines with argon, heat Ti gas purifier to 900°C.

(6) Bleed argon to a chamber pressure of $\approx 3 * 10^{-3}$ torr by the needle valve and allow the system to stabilize.

(7) Select target, place the shield over the corresponding substrate, raise chamber pressure to $\approx 10 * 10^{-3}$ torr by the sputter-shutter valve.

(8) Start the R.F. generator and apply low power to the target to warm up the generator.

(9) Start plasma by:

a) Applying high power (≈500 watts)
b) Using teslacoil

(10) Set argon pressure to desired level and match system at high power input.

(11) Monitor the forward and reflected power and the D.C. bias and the R.F. kilovoltages until they indicate the target is clean and they have stabilized.

(12) Set power level to approximate range to give desired D.C. bias kilovoltage and R.F. kilovoltage with the system matched.

(13) Remove shield over substrate and immediately set the parameters and match the system to give the desired conditions.

(14) Adjust the driver control, the shunt and series controls of the matching network and the needle valve to maintain the sputtering conditions while depositing on the substrate.

(15) Quench plasma by turning R.F. generator off.

Post-sputtering Stage (1/2 hour)

(16) Pump chamber and gas lines to $\approx 5 * 10^{-7}$ torr.

(17) Backfill chamber to atmospheric with nitrogen and remove substrate(s).

(18) Pump chamber to 10^{-1} torr and hold.

APPENDIX II

Data Sheet

RUN # ____
DATE ______
ELECTRODE # ___
TARGET ____________________
SUBSTRATE ____________________

INITIAL VACUUM __________
NEEDLE VALVE SETTING ________
LINE PRESSURE ________
GAS PURIFIER ______
SPUTTER SHUTTER VALVE ______, SLIDE ___

TIME (min)	FORWARD POWER (watts)	REFLECTED POWER (watts)	R.F. VOLTAGE (kilovolts)	D.C. BIAS (kilovolts)	PRESSURE (microns)	FINE TUNING SETTING	
						SERIES (----)	SHUNT (---)

Comments:

APPENDIX III

Calculation of the Sticking Coefficient of Nickel on Glass

From Figure 7 of the Results and Discussion section, two deposition rates are known:

$$t = 0^+, \quad \dot{D}\Big|_{t=0^+} = 66 \text{ Å/min.}$$

$$t \gg 0, \quad \dot{D}\Big|_{t=\infty} = 131 \text{ Å/min.}$$

Assuming the resputtering and evaporation rates are negligible, then:

$$\dot{D} = s_{Ni}\dot{N}_{Ni} + s_{A\ell}\dot{N}_{A\ell} \qquad \text{(III-1)}$$

The sputtering rates are independent of time so:

$$\dot{D}\Big|_{t=0^+} = s_{Ni}\Big|_{t=0^+} \dot{N}_{Ni} + s_{A\ell}\Big|_{t=0^+} \dot{N}_{A\ell} \qquad \text{(III-2)}$$

$$\dot{D}\Big|_{t=\infty} = s_{Ni}\Big|_{t=\infty} \dot{N}_{Ni} + s_{A\ell}\Big|_{t=\infty} \dot{N}_{A\ell} \qquad \text{(III-3)}$$

Under steady state conditions with respect to the target surface, the sputtering rate of each specie is directly proportional to the bulk target composition:

$$\frac{\dot{N}_{Ni}}{\dot{N}_{A\ell}} = \frac{x_{Ni}}{x_{A\ell}} = \frac{0.8611}{0.1389} \qquad \text{(III-4)}$$

$$\dot{N}_{A\ell} = 0.1613 \, \dot{N}_{Ni} \qquad \text{(III-5)}$$

With the known deposition rates and equations (III-2), (III-3), (III-5), a relation with only the sticking coefficients can be derived as follows:

$$\dot{D}\big|_{t=0^+} = 66 = (s_{Ni}\big|_{t=0^+})(\dot{N}_{Ni}) + (s_{A\ell}\big|_{t=0^+})(0.1613\ \dot{N}_{Ni}) \qquad \text{(III-6)}$$

$$\dot{D}\big|_{t=\infty} = 131 = (s_{Ni}\big|_{t=\infty})(\dot{N}_{Ni}) + (s_{A\ell}\big|_{t=\infty})(0.1613\ \dot{N}_{Ni}) \qquad \text{(III-7)}$$

$$\frac{D\big|_{t=\infty}}{D\big|_{t=0^+}} = \frac{131}{66} = \frac{(s_{Ni}\big|_{t=\infty})(N_{Ni}) + (s_{A\ell}\big|_{t=\infty})(0.1613\ N_{Ni})}{(s_{Ni}\big|_{t=0^+})(N_{Ni}) + (s_{A\ell}\big|_{t=0^+})(0.1613\ N_{Ni})} \qquad \text{(III-8)}$$

$$1.985 = \frac{(s_{Ni}\big|_{t=\infty}) + (s_{A\ell}\big|_{t=\infty})(0.1613)}{(s_{Ni}\big|_{t=0^+}) + (s_{A\ell}\big|_{t=0^+})(0.1613)} \qquad \text{(III-9)}$$

From the electron microprobe analysis, the sticking coefficient of aluminum is (see Appendix VI):

$$s_{A\ell}\big|_{t=\infty} \approx 0.55$$

For simplicity of this analysis, it can be assumed that:

$$s_{A\ell}\big|_{t=0^+} = s_{A\ell}\big|_{t=\infty} = 0.55$$

It is also known that at $t \gg 0$, $s_{Ni}\big|_{t=\infty} = 1.00$ so by substituting these values into equation (III-9), the initial sticking coefficient of nickel on glass is:

$$1.985 = \frac{1.00 + (0.55)(0.1613)}{(s_{Ni}|_{t=0^+}) + (0.55)(0.1613)}$$

$$s_{Ni}|_{t=0^+} = 0.4594$$

$$s_{Ni}|_{t=0^+} \approx 0.5$$

APPENDIX IV

Analysis of Sputtering Yield Versus Ion Energy

An approximate expression for the sputtering yield as a function of ion energy is desired for ion energies above 1 kev. For the low ion energies below 10 kev, there are three regions of the sputtering yield versus ion energy curve. At the ion energies of approximately 0.5 kev, the yield, S, is approximately a linear function of ion energy, E:

$$E \approx 0.5, \qquad S = C * E \qquad \text{(IV-1)}$$

Conversely at the high energies above 5 kev, the sputtering yield is approximately constant (increasing at a very slow rate):

$$E > 5, \qquad S \approx C' \qquad \text{(IV-2)}$$

For the present work, the transition region between these two limits of ion energies, between approximately 1 kev and 5 kev, is of concern. The simplest expression for the sputtering yield as a function of the ion energy over this transition region is [43]:

$$S \propto \ln (E/E_t) \qquad \text{(IV-3)}$$

where E is the ion energy and E_t is the threshold energy

for the ion-target atom combination. This gives the relation:

$$1 < E < 5, \qquad S = k \ln (E/E_t) \qquad \text{(IV-4)}$$

The natural logarithm of x for x > ½ can be expressed by the following series*:

$$\ln x = \frac{x-1}{x} + \frac{1}{2}\left(\frac{x-1}{x}\right)^2 + \frac{1}{3}\left(\frac{x-1}{x}\right)^3 + \ldots \qquad \text{(IV-5)}$$

The threshold energy of equation (IV-4) is on the order of 0.02 kev (Table XIV) and with $(E/E_t) >> ½$, the series expansion may be used to give:

$$S = k \left[\frac{(E/E_t)-1}{(E/E_t)} + \frac{1}{2}\left(\frac{(E/E_t)-1}{(E/E_t)}\right)^2 + \frac{1}{3}\left(\frac{(E/E_t)-1}{(E/E_t)}\right)^3 + \ldots.\right] \qquad \text{(IV-6)}$$

$$S = k \left[\frac{E-E_t}{E} + \frac{1}{2}\left(\frac{E-E_t}{E}\right)^2 + \frac{1}{3}\left(\frac{E-E_t}{E}\right)^3 + \ldots.\right] \qquad \text{(IV-7)}$$

Considering the first three terms of the series to observe the basic form of the expression, equation (IV-7) reduces to:

$$S = k\left[\frac{11}{6} - \frac{3(E_t)}{E} + \frac{3(E_t)^2}{2E^2} - \frac{(E_t)^3}{2E^3}\right] \qquad \text{(IV-8)}$$

The general form of equation (IV-4) with the series expansion of the natural logarithm is thus:

---

*Standard Mathematical Tables, Chemical Rubber Co., 13th ed., p. 381.

$$S = a + \frac{b}{E} + \frac{c}{E^2} + \frac{d}{E^3} + \ldots. \qquad \text{(IV-9)}$$

For E >> 0, equation (IV-9) gives the proper limit of S = a in agreement with equation (IV-2). As the energy decreases, the higher power terms contribute more to the value of the sputtering yield.

To approximate equation (IV-9) by two terms, three terms, or more, high ion energy sputtering yield data is required. As shown in Table XIII, there is low ion energy data for both nickel and aluminum; however, there is no high ion energy data for nickel as there is for aluminum. The sputtering yield of nickel by Ar^+ at high energies can be approximated from the high ion energy sputtering yield data of Bader et al. [44] for nitrogen bombarding nickel. For constant ion energy and target material, the sputtering yield can be taken proportional to the ion-target atom energy transfer term ε [43]:

$$\varepsilon = \frac{4M_1M_2}{(M_1+M_2)^2} \qquad \text{(IV-10)}$$

where M_1 and M_2 are the masses of the bombarding ion and sputtered atom respectively. Thus the relation between the sputtering yield of Ni by N_2^+ of energy E, $S_{N_2}^{Ni}|_E$, and the sputtering yield of Ni by Ar^+ of energy E, $S_{Ar}^{Ni}|_E$, is:

$$\frac{S_{Ar}^{Ni}|_E}{S_{N_2}^{Ni}|_E} = \frac{4\, M_{Ar}\; M_{Ni}/(M_{Ar} + M_{Ni})^2}{4\, M_{N_2}\; M_{Ni}/(M_{N_2} + M_{Ni})^2} \qquad \text{(IV-11)}$$

Substituting in the appropriate values:

$$S_{Ar}^{Ni}|_E \approx 1.1 * S_{N_2}^{Ni}|_E \qquad \text{(IV-12)}$$

The sputtering yield of nickel by N_2^+ of 5 kev ion energy is ≈ 2.3 by Bader et al. and this gives the sputtering yield of nickel by Ar^+ of 5 kev ion energy as:

$$S_{Ar}^{Ni}|_5 \approx 2.53$$

Equation (IV-9) can be solved for the n constants (i.e. for n terms) with n sputtering yield-ion energy values. Table IV-1 gives the calculated values of the sputtering yield for a four term expression, $S = a + \frac{b}{E} + \frac{c}{E^2} + \frac{d}{E^3}$, and for a two term expression, $S = a + \frac{b}{E}$, along with the published values and the values of the constants. With the available data, the four term series represents the data the best. Comparing the two term series to the four term series, the agreement is very good for ion energies above 1 kev and is poor at the lower energies where the higher power terms are significant. With the desired result being a simple, fairly accurate expression for the sputtering yield above 1 kev, the two term expressions are sufficient. Thus for Figure 10 of the text, the sputtering yield variations with ion energy are:

$$S_{Ar}^{Ni}\Big|_E = 2.6375 - \frac{0.5375}{E}$$

$$S_{Ar}^{A\ell}\Big|_E = 2.1036 - \frac{0.5182}{E}$$

Table IV-1

Data Points for Solution

Four term, Ni	2.53/5*	2.10/1	1.52/0.6	0.70/0.2
Two term, Ni	2.53/5	2.10/1		
Four term, Aℓ	2.00/5	1.24/0.6	1.05/0.5	0.35/0.2
Two term, Aℓ	2.00/5	1.24/0.6		

* sputtering yield at energy E/ argon ion energy

Values of Constants

	a	b	c	d
Four term, Ni	+2.56558	-0.09005	-0.45226	+0.07973
Two term, Ni	+2.63750	-0.53750	0	0
Four term, Aℓ	+2.07600	-0.35449	-0.13334	+0.02704
Two term, Aℓ	+2.10360	-0.51820	0	0

Calculated Sputtering yields

Ion Energy	Ni (published)	Ni (four term)	Ni (two term)	Aℓ (published)	Aℓ (four term)	Aℓ (two term)
5.0 kev	(2.53)	2.53	2.53	2.00	2.00	2.00
4.5 kev	---	2.52	2.52	----	1.99	1.99
4.0 kev	----	2.52	2.50	----	1.98	1.97
3.5 kev	----	2.50	2.48	----	1.96	1.96
3.0 kev	----	2.49	2.46	----	1.94	1.93
2.5 kev	----	2.46	2.42	----	1.91	1.90
2.0 kev	----	2.42	2.37	----	1.87	1.84
1.5 kev	----	2.33	2.28	----	1.79	1.76
1.0 kev	2.10	2.10	2.10	----	1.62	1.59
0.6 kev	1.52	1.52	1.74	1.24	1.24	1.24
0.5 kev	1.39	1.20	1.56	1.05	1.05	1.07
0.2 kev	0.70	0.70	-0.05	0.35	0.35	-4.87

APPENDIX V

Analysis of Deposition Rate for Ni-Al Alloy Target

The net deposition rate $\dot{D}$ for the Ni-Al alloy target is expressed as:

$$\dot{D} = \dot{D}_{Ni} + \dot{D}_{Al} \qquad \text{(V-1)}$$

By assuming the resputtering and evaporation rates are neglible, the net deposition rate is:

$$\dot{D} = s_{Ni}\dot{N}_{Ni} + s_{Al}\dot{N}_{Al} \qquad \text{(V-2)}$$

By also assuming that initially, i.e. $t=0^+$, $s_{Ni} = s_{Al}$ which is effectively assuming a sticking coefficient for the alloy, i.e. $s_{Ni} = s_{Al} = s_{alloy}$, the net deposition rate is:

$$\dot{D} = s_{alloy} (\dot{N}_{Ni} + \dot{N}_{Al}) \qquad \text{(V-3)}$$

The sputtering rate is expressed as:

$$\dot{N}_{Ni} = x_{Ni} * J * y_{Ni}$$

$$\dot{N}_{Al} = x_{Al} * J * y_{Al}$$

$$\dot{N} = \dot{N}_{Ni} + \dot{N}_{Al} = J * (x_{Ni}y_{Ni} + x_{Al}y_{Al}) \qquad \text{(V-4)}$$

The ion flux J is defined as:

$$J = I/A$$

$$J = \text{ion flux} = \frac{\text{ions}}{\text{cm}^2\ \text{sec}}$$

$$I = \text{ion current} = \text{ions/sec}$$

$$A = \text{target area} = cm^2$$

The ion current is directly proporational to the net D.C. bias kilovoltage, which is equal to the R.F. kilovoltage, so:

$$\frac{dV}{dt} = I/C \rightarrow\rightarrow \quad I \propto V_{RF}$$

This gives the ion flux as:

$$J \propto V_{RF} \tag{V-6}$$

By considering two conditions, 1 and 2, the ratio of the sputtering can be expressed as:

$$\frac{(\dot{N}_{Ni} + \dot{N}_{Al})|_1}{(\dot{N}_{Ni} + \dot{N}_{Al})|_2} = \frac{J_1}{J_2} * \frac{x_{Ni}|_1\, y_{Ni}|_1 + x_{Al}|_1\, y_{Al}|_1}{x_{Ni}|_2\, y_{Ni}|_2 + x_{Al}|_2\, y_{Al}|_2}$$

$$\frac{(\dot{N}_{Ni} + \dot{N}_{Al})|_1}{(\dot{N}_{Ni} + \dot{N}_{Al})|_2} = \frac{V_{RF}|_1}{V_{RF}|_2} * \frac{x_{Ni}|_1\, y_{Ni}|_1 + x_{Al}|_1\, y_{Al}|_1}{x_{Ni}|_2\, y_{Ni}|_2 + x_{Al}|_1\, y_{Al}|_1} \tag{V-7}$$

By combining the net deposition rate relation, equation (V-3), with the sputtering rate relation, equation (V-7), the ratio of the deposition rates for two conditions is:

$$\frac{\dot{D}_1}{\dot{D}_2} = \frac{s_{alloy}|_1}{s_{alloy}|_2} * \frac{(\dot{N}_{Ni} + \dot{N}_{Al})|_1}{(\dot{N}_{Ni} + \dot{N}_{Al})|_2} \tag{V-8}$$

$$\frac{\dot{D}_1}{\dot{D}_2} = \frac{s_{alloy}|_1}{s_{alloy}|_2} * \frac{V_{RF}|_1}{V_{RF}|_2} * \frac{x_{Ni}|_1\, y_{Ni}|_1 + x_{Al}|_1\, y_{Al}|_1}{x_{Ni}|_2\, y_{Ni}|_2 + x_{Al}|_2\, y_{Al}|_2} \tag{V-9}$$

The target is an alloy so under steady state conditions, the sputtering rate of each specie is proportional to the atomic fraction of each specie in the

target:

$$\frac{\dot{N}_{Ni}}{\dot{N}_{Al}} = \frac{x_{Ni}|_{target}}{x_{Al}|_{target}} \qquad \text{(V-10)}$$

The composition of the target is (Table IV):

93.1 wt.% Ni → → 0.8611 at. fract. Ni

6.9 wt.% Al → → 0.1389 at. fract. Al

and thus equation (V-10) becomes:

$$\frac{\dot{N}_{Ni}}{\dot{N}_{Al}} = \frac{0.8611}{0.1389} \qquad \text{(V-11)}$$

Expanding the sputtering rate of each specie:

$$i=1,2 \qquad \frac{(x_{Ni}|_i)\,(J_i)\,(y_{Ni}|_i)}{(x_{Al}|_i)\,(J_i)\,(y_{Al}|_i)} = \frac{0.8611}{0.1389} \qquad \text{(V-12)}$$

$$i=1,2 \qquad \frac{(x_{Ni}|_i)\,(y_{Ni}|_i)}{(x_{Al}|_i)\,(y_{Al}|_i)} = \frac{0.8611}{0.1389} \qquad \text{(V-13)}$$

The total composition must be 100 atomic %:

$$i=1,2 \qquad x_{Ni}|_i + x_{Al}|_i = 1.00 \qquad \text{(V-14)}$$

$$i=1,2 \qquad x_{Al}|_i = 1 - x_{Ni}|_i \qquad \text{(V-15)}$$

Substituting equation (V-15) in equation (V-13):

$$i=1,2 \qquad \frac{x_{Ni}|_i}{1 - x_{Ni}|_i} * \frac{y_{Ni}|_i}{y_{Al}|_i} = \frac{0.8611}{0.1389} \qquad \text{(V-16)}$$

Equations (V-16), (V-15) and (V-9) are the governing relations because the values needed are known as follows:

V_{RF} is measured,

y_{Ni} and y_{Al} are found from published data,

$\dot{D}$ is known from D vs. t relation,

$s_{alloy\ 1}$ may be assumed equal to $s_{alloy\ 2}$ at $t=0^+$.

APPENDIX VI

Aluminum Sticking Coefficient Calculation for 93.1Ni - 6.9Aℓ Alloy Target

The average composition of the sputtered thin film is Ni-3.947 wt.% Aℓ from the Ni-6.9 wt.% Aℓ alloy target. With steady state conditions at the target surface, the sputtering rate for each specie is:

$$\frac{\dot{N}_{A\ell}}{\dot{N}_{Ni}} = \frac{0.1389}{0.8611} \qquad \text{(VI-1)}$$

By assuming the resputtering and evaporation rates are negligible, the deposition rate for each specie may be expressed as:

$$\frac{\dot{D}_{A\ell}}{\dot{D}_{Ni}} = \frac{s_{A\ell}\dot{N}_{A\ell}}{s_{Ni}\dot{N}_{Ni}} \qquad \text{(VI-2)}$$

From the microprobe analysis, the ratio of the deposition rates is:

$$\frac{\dot{D}_{A\ell}}{\dot{D}_{Ni}} = \frac{0.0821}{0.9179} \qquad \text{(VI-3)}$$

Taking the sticking coefficient of Ni equal to unity and substituting equation (VI-1) and (VI-3) into equation (VII-2), the sticking coefficient of aluminum is calculated as:

$$s_{A\ell} = s_{Ni} * \frac{\dot{N}_{Ni}}{\dot{N}_{A\ell}} * \frac{\dot{D}_{A\ell}}{\dot{D}_{Ni}}$$

$$s_{A\ell} = 0.5543$$

$$s_{A\ell} \approx 0.55$$

APPENDIX VII

Target Composition Calculation For Ni-Ta Plasma-Sprayed Targets

By rearranging equation (31) of the text for the ratio of the target compositions, the equation is:

$$\frac{x_{Ni}}{x_{Ta}} = \frac{s_{Ta}}{s_{Ni}} * \frac{y_{Ta}}{y_{Ni}} * \frac{\dot{D}_{Ni}}{\dot{D}_{Ta}} \qquad \text{(VII-1)}$$

The sticking coefficients of nickel and tantalum are assumed to be unity. The sputtering yield of nickel is taken from Figure 10. Using the analysis of Appendix IV based on the 5 kv and 0.6 kv data of Table XIII, the sputtering yield of tantalum is given by:

$$y_{Ta} = 1.1114 - \frac{0.30682}{V_{RF}}$$

This relation gives the sputtering yield of tantalum as 0.98 for 2.3 kv $< V_{RF} <$ 2.4 kv. The composition values used in equation (VII-1) are the atom fractions. Also the total composition is expressed as:

$$x_{Ta} = 1 - x_{Ni} \qquad \text{(VII-2)}$$

The following table gives the values used and the solution to equations (VII-1) and (VII-2) for the "expected" target composition.

s_{Ni}	s_{Ta}	V_{RF}	y_{Ni}	y_{Ta}	(D_{Ni} /	D_{Ta})	x_{Ni}	x_{Ta}
(---)	(---)	(kv)	($\frac{atoms}{ion}$)	($\frac{atoms}{ion}$)	(--)	(--)	(wt.%)	(wt.%)
1.00	1.00	2.37	2.41	0.98	(98.84 /	1.16)	97.2	2.8
1.00	1.00	2.41	2.41	0.98	(93.57 /	6.43)	85.5	14.5
1.00	1.00	2.30	2.40	0.98	(93.13 /	6.87)	84.7	15.3

LIST OF REFERENCES

[1] ______, Handbook of Chemistry and Physics, 45th edition, R.C. Weast, ed., Chemical Rubber Company, Cleveland, Ohio, 1964.

[2] Decker, R.F., "Strengthening Mechanisms in Nickel-Based Superalloys," Symposium: Steel-Strengthening Mechanisms, Climax Molybdenum Company, 1969.

[3] Hansen, M., Constitution of Binary Alloys, McGraw-Hill Book Co., Inc., New York, 1958, p.119.
Shunk, F.A., Constitution of Binary Alloys, Second Supplement, McGraw-Hill Book Co., Inc., New York, 1969, p.557.

[4] Maissel, L.I. and P.M. Schaible, "Thin Films Deposited by Bias Sputtering," Journal of Applied Physics, 36, 237-242(1965).

[5] Frerichs, R., "Superconductive Films Made by Protected Sputtering of Tantalum or Niobium," Journal of Applied Physics, 33, 1898-1899(1962).

[6] Edgecumbe, J., L.G. Rosner, and D.E. Anderson, "Preparation and Properties of Thin Film Hard Superconductors," Journal of Applied Physics, 35, 2198-2202(1964).

[7] Cash, J.H., J.A. Cunningham, and J.P. Keene, "R.F. Sputtering of Metals," Second Symposium on the Deposition of Thin Films by Sputtering, University of Rochester, June 6-7, 1967, Proceedings, 1-9.

[8] Vratny, F., "Deposition of Tantalum and Tantalum Oxide by Superimposed R.F. and D.C. Sputtering," Journal of the Electrochemical Society, 114, 505(1967).

[9] Theuerer, H.C. and J.J. Hauser, "Getter Sputtering for the Preparation of Thin Films of Superconducting Elements and Compounds," Journal of Applied Physics, 35, 554-555(1964).

[10] Logan, J.S., "Control of R.F. Sputtering Film Properties Through Substrate Tuning," I.B.M. Journal of Research Development, March, 1970.

[11] Heil, R., S. Hurwith and W. Huss, "Sputter Etching of Microcircuits and Compounds," Solid State Technology, Dec. 1968, 42-47.

[12] Gerstenberg, D. and E.H. Moyer, "Properties of Tantalum Sputtered Films," Proceedings of 1962 Electronics Components Conference, 57-61(1962).

[13] Berry, R.W., P.M. Hall and M.T. Harris, Thin Film Technology, Van Nostrand Reinhold Co., New York, 1968, p.220.

[14] Gill, W.D. and E. Kay, "Efficient Low Pressure Sputtering in a Large Inverted Magnetron Suitable for Film Synthesis," Review of Scientific Instruments, 36, 277-282(1965).

[15] Steidel, C.A., D. Jaffe and H.Y. Kumagai, "Compositional Control of Tantalum-Aluminum Alloy Films by a D.C. Biased, A.C. Sputtering Technique," Journal of Vacuum Science and Technology, 9, 346(1972).

[16] Henrickson, J.F., G. Krauss, R.N.Tauber and D.J. Sharp, "Structure and Properties of Sputtered Ta-Al_2O_3 Cermet Thin Films," Journal of Applied Physics, 40, 5006-5014(1969).

[17] Shoemaker, R.T., C.E. Anderson and G.L. Liedl, "Sputtering of Bismuth-Titanium Two-Phase Cathodes," Journal of Electrochemical Society, 117, 1438-1439 (1970).

[18] Cowan, R.L. and M.R. Notis, "The Effect of Substrate Temperature and Cathode Composition on the Composition of Sputtered Ta-Al Thin Films," unpublished paper, Lehigh University, 1970.

[19] Winters, H.F., D.L. Raimondi and D.E. Horne, "Proposed Model for the Composition of Sputtered Multicomponent Thin Films," Journal of Applied Physics, 40, 2996-3006(1969).

[20] Neugebauer, C.A., "Condensation, Nucleation, and Growth of Thin Films," Handbook of Thin Film Technology, ed. L.I. Maissel and R. Glang, McGraw-Hill, Inc., New York, 1970, Chapter 8.

[21] Chopra, K.L., Thin Film Phenomena, McGraw-Hill, Inc., New York, 1969, 149-151.

[22] Mader, S., "Metastable Alloy Films," Journal of Vacuum Science and Technology, 2, 35-41(1965).

[23] Spitzer, H.J., "Relationship Between Substrate Temperature, Structure, and Superconducting Properties of Reactive Sputtered Niobium Nitride Thin Films," Journal of Vacuum Science and Technology, 9, 333-336(1972).

[24] Tolansky, S., Multiple-Beam Interferometry of Surfaces and Films, Dover Publications, Inc., New York, 1970.

[25] Anderson, C.A. "Electron Probe Microanalysis of Thin Layers and Small Particles with Emphasis on Light Element Determinations," Electron Microprobe, ed. T.D. McKinley, K.F.J. Heinrich and D.B. Witty, John Wiley & Sons, Inc., New York, 1966, p.58.

[26] Goldstein, J.I. and P.A. Comella, A Computer Program for Electron Probe Microanalysis in the Fields of Metallurgy and Geology, Goddard Space Flight Center, Greenbelt, Md., X-642-69-115, April, 1969.

[27] Colby, J., Bell Telephone Laboratory, Allentown, Pa., personal communication,

[28] Alder, I. and J.I. Goldstein, Absorption Tables for Electron Probe Microanalysis, Goddard Space Flight Center, Greenbelt, Md., NASA Technical Note D-2984, October, 1965.

[29] Anderson, G.S., W.N. Mayer and G.K. Wehner, "Sputtering of Dielectrics by High Frequency Fields," Journal of Applied Physics, 33, 2991-2992(1962).

[30] Yang, L., C.E. Birchenall, G.M. Pound and M.J. Simnad, "Some Observations on Hetergeneous Nucleation

of Sodium Crystals From Atomic Beams," Acta Metallurgica, 2, 462-469(1954).
Yang, L., M.J. Simnad and G.M. Pound, "A Radioactive Tracer Study of Silver Condensation on Substrates," Acta Metallurgica, 2, 470-475(1954).

[31] Johnson, J.E., "Kinetics of Cadmium Sulfide Evaporated Film Formation," Vacuum Microbalance Techniques, ed. P.M. Waters, 4, 81-98(1965).

[32] Tsui, R.T.C., "Calculation of Ion Bombarding Energy and Its Distribution in R.F. Sputtering," Physical Review, 168, 107-113(1968).

[33] Butler, H.S. and G.S. Kino, "Plasma Sheath Formation by Radio-Frequency Fields," The Physics of Fluids, 6, 1346-1355(1963).

[34] Brodie, I., L.T. Lamont, Jr. and D.O. Myers, "Substrate Bombardment During R.F. Sputtering," The Journal of Vacuum Science and Technology, 6, 124-127(1969).

[35] Anderson, G.S., W. N. Mayer and G.K. Wehner, "Sputtering of Dielectrics by High Frequency Fields," Journal of Applied Physics, 33, 2991-2992(1962).

[36] Wehner, G.K., General Mills Report #2309, July, 1962.

[37] Weijsenfeld, C.H. and A. Hoogendoorn, "Proceedings of the Fifth Conference on Ionization Phenomena in Gases," Munich (1961), 1, North Holland Publishing Co., Amsterdam, p.124.

[38] McKeown, D. and A.Y. Cabezas, Annual Report of Space Science Laboratory General Dynamics/Astronautics, July, 1962.

[39] Laegreid, N. and G.K. Wehner, "Sputtering Yields of Metals for Ar^+ and Ne^+ Ions with Energies from 50 to 600w," Journal of Applied Physics, 32, 365-369(1961).

[40] Carlston, C.E., G.D. Magnuson, A. Comeaux and P. Mahodevan, "Effect of Elevated Temperatures on Sputtering Yield," Physical Review, 138, A759-A763(1965).

[41] Weijsenfeld, C.H., A. Hoogendoorn and M. Koedam, "Sputtering of Polycrystalline Metals by Inert Gas Ions of Low Energy(100-1000w)," Letter to the Editor, Physica, 27, 763-764(1961).

[42] Wehner, G.K., and G.S. Anderson, "The Nature of Physical Sputtering," Handbook of Thin Film Technology, ed. L.I. Maissel and R. Glang, McGraw-Hill, Inc., New York, 1970, p.3-19.

[43] Carter, G., and J.S. Colligon, Ion Bombardment of Solids, Hunemann Educational Books, Ltd., London, 1968, p.310.

[44] Bader, M., F.C. Witteborn and T.W. Snouse, NASA Report #TR-R-105, Washington(1961).

[45] Glang, R., "Vacuum Evaporation," Handbook of Thin Film Technology, ed. L.I. Maissel and R. Glang, McGraw-Hill, Inc., New York, 1970, p.1-22.

[46] Dushman, S., Scientific Foundations of Vacuum Technique, John Wiley and Sons, Inc., New York, 1962, p.39.

[47] Levitskii, S.M., "Space Potential and Electrode Sputtering in a High Frequency Discharge," Soviet Physics Technical Physics, Transl., 2, 913-920(1957).

[48] Cannara, A.B. and F.W. Crawford, "Beam Probing of R.F. Beam/Plasma Interface," Journal of Applied Physics, 36, 3132-3135(1965).

[49] Autier, B., and R. Lewis, "Application Laboratory Report," Cameca Instruments, Inc., Feasibility Report Using Cameca Ion Analyzer-IMS 300, June 23, 1972.

[50] Fagen, E.A., "Thermally Stimulated Argon Release From Amorphous Alloy Films," Material Research Bulletin, 7, 279-284(1972).

[51] Stewart, A.D.G., and M.W. Thompson, "Microtopography of Surfaces Eroded by Ion-Bombardment," Journal of Material Science, 4, 56-60(1969).

[52] Bayly, A.R., "Secondary Processes in the Evolution of Sputter-Topographies," Journal of Material Science, 7, 404-412(1972).

[53] ______, "The Powder Diffraction File," Joint Committee on Powder Diffraction Standards, Philadelphia, 1971.

[54] Pashley, D.W. and M.J. Stowell, "Electron Microscopy and Diffraction of Twinned Structures in Evaporated Films of Gold," Philosophy Magazine, 8, 1605-1632(1963).

[55] Presland, A.E.B., G.F. Price and D.L. Trimm, "Hillock Formation by Surface Diffusion on Thin Silver Films," Journal of Surface Science, 29, 424-434(1972).

[56] Presland, A.E.B., G.L. Price and D.L. Trimm, "The Role of Microstructure and Surface Energy in Hole Growth and Island Formation in Thin Silver Films," Journal of Surface Science, 29, 435-446(1972).

[57] Corey, C.L. and B. Lisowsky, "The Ni_3Al Ordering Systems," Technical Report, Wayne State University, June, 1966.

VITA

David Gregory Hill was born on April 10, 1948 in Baltimore, Maryland to Mr. and Mrs. William P. Hill. He graduated from Shady Side Academy in Pittsburgh, Pennsylvania in June, 1966 with Cum Laude honors. He enrolled at the College of Engineering of Cornell University in September, 1966 and graduated with a Bachelor of Science degree in June, 1970. While attending Cornell University, he specialized in mechanical engineering. Also, Mr. Hill was commissioned an Ensign in the U.S. Naval Reserves on June 8, 1970.

Mr. Hill recieved a two year delay in active duty from the U.S. Navy to pursue graduate studies. In September, 1970, he enrolled at Lehigh University as a candidate for a Master of Science degree in metallurgy and material science.

Mr. Hill is a member of ASME, AISE, ASM and AIME professional societies.